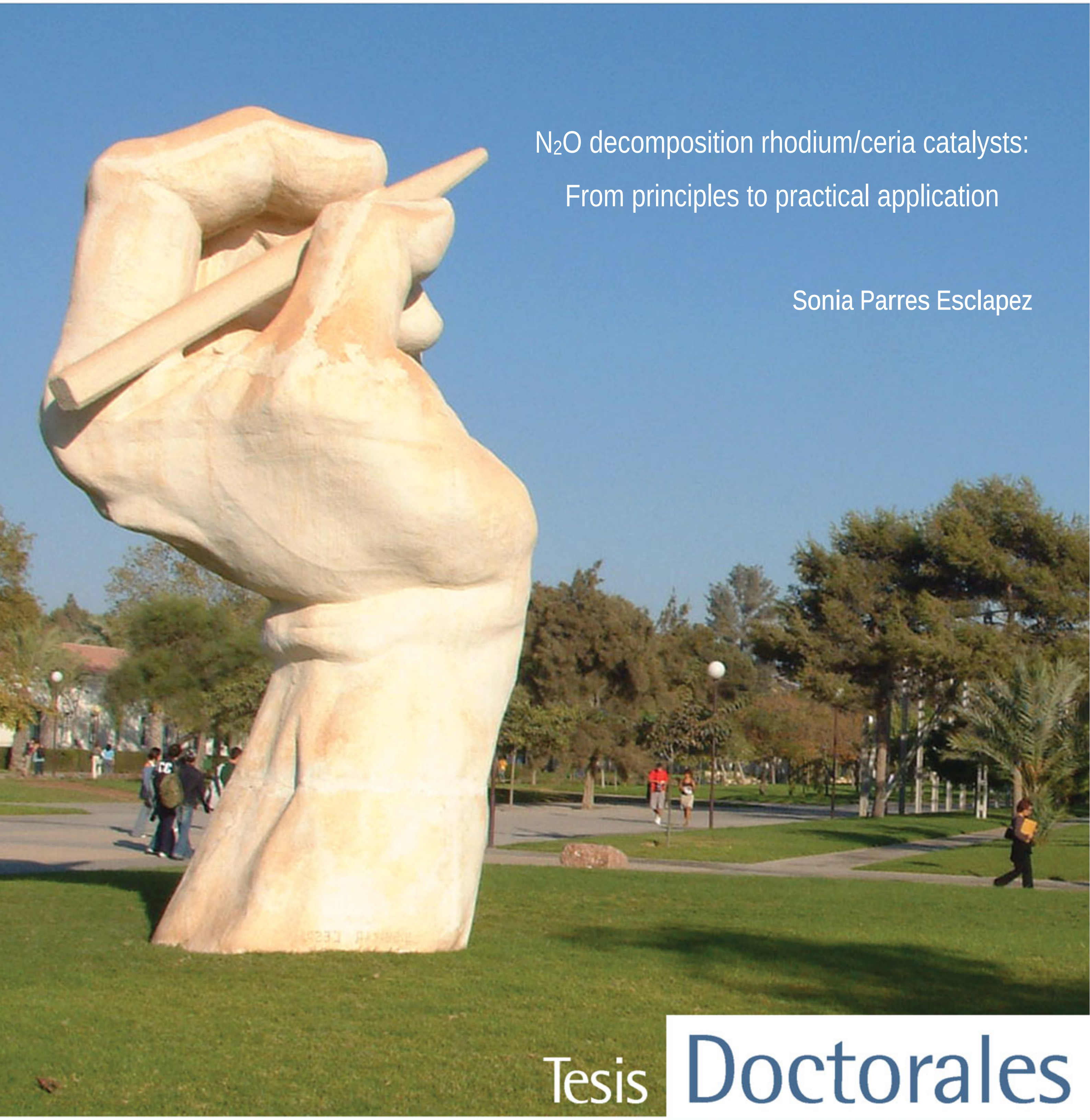

N_2O decomposition rhodium/ceria catalysts: From principles to practical application

Sonia Parres Esclapez

PhD THESIS | October 2011

Sonia Parres Esclapez

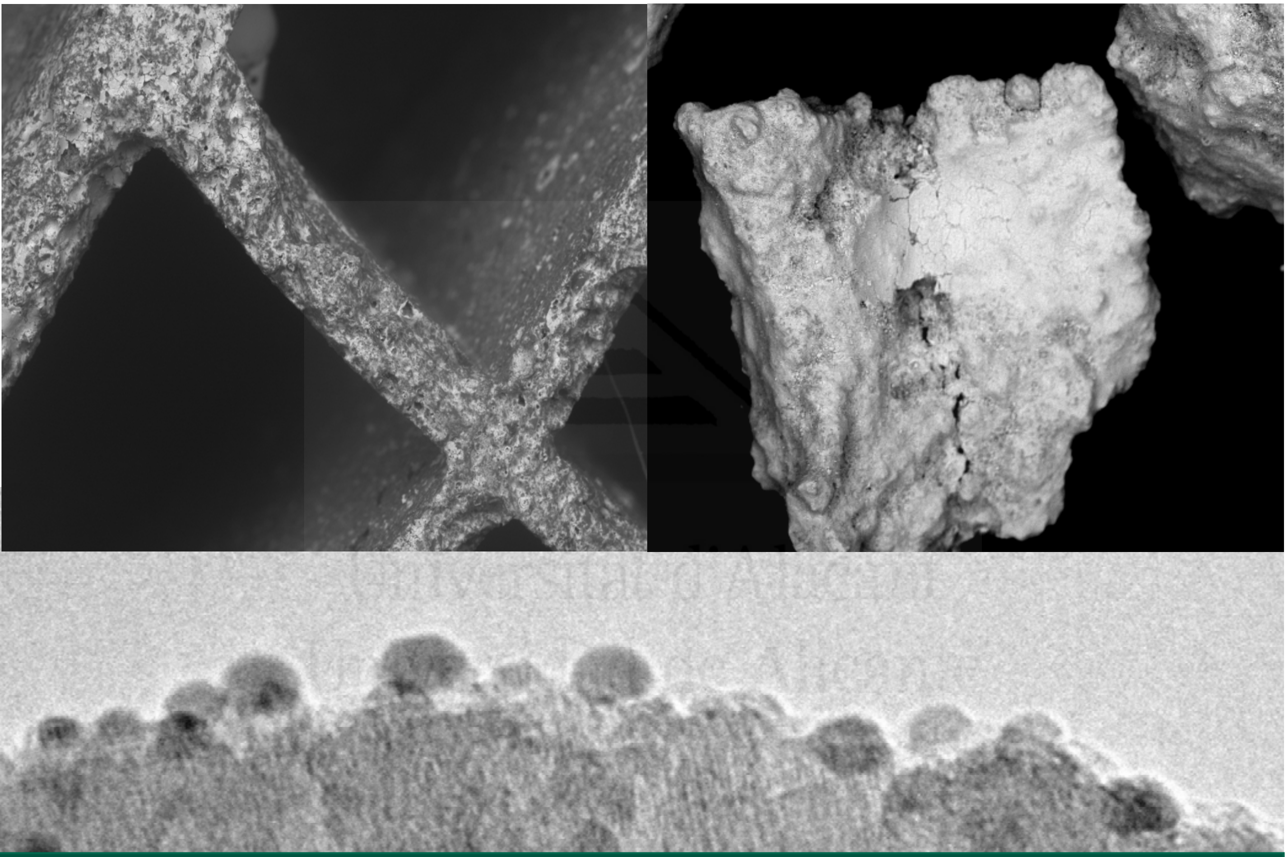

N_2O decomposition rhodium/ceria catalysts:

From principles to practical application

University of Alicante

UNIVERSIDAD DE ALICANTE

Departamento de Química Inorgánica
Grupo de Materiales Carbonosos y Medio Ambiente (MCMA)

N_2O decomposition rhodium/ceria catalysts: From principles to practical application.

Memoria presentada para aspirar al grado de Doctor

Sonia Parres Esclapez

Directores del trabajo:

Agustín Bueno López
Profesor Titular de
Química Inorgánica

María José Illán Gómez
Catedrática de
Química Inorgánica

Alicante, Octubre 2011

María José Illán Gómez, Catedrática de Química Inorgánica y Agustín Bueno López, Profesor Titular de Química Inorgánica de la Universidad de Alicante,

CERTIFICAN QUE:

Dña. Sonia Parres Esclapez, Licenciada en Química, ha realizado en el Departamento de Química Inorgánica de la Facultad de Ciencias de la Universidad de Alicante, bajo nuestra dirección, el trabajo titulado “N_2O decomposition rhodium/ceria catalysts: From principles to practical application” que constituye su Memoria para aspirar al grado de Doctor por la Universidad de Alicante reuniendo, a nuestro juicio, las condiciones necesarias para ser presentada y defendida ante el tribunal correspondiente.

Y para que conste a los efectos oportunos, en cumplimiento de la legislación vigente, firmamos el presente certificado en Alicante, a 14 de Septiembre de 2011.

Fdo. Agustín Bueno López.   Fdo. María José Illán Gómez.

Agradecimientos/Acknowledgments

Después de cinco años, por fin llegó el momento que tanto esperaba, escribir y finalizar mi Tesis doctoral, sabía que no sería fácil, pero lo que no sabía es que escribir estas líneas también resultaría complicado. Me resulta muy complejo plasmar en pocas palabras todo lo que me han aportado estos años y el agradecimiento a toda la gente que de un modo u otro ha hecho posible este camino, o al menos, me lo ha facilitado.

Me gustaría empezar por las personas que hicieron posible mi incorporación al grupo de Materiales Carbonosos y Medio Ambiente. La Dra. Concepción Salinas Martínez de Lecea, la Dra. María José Illán Gómez y el Dr. Agustín Bueno López, a los tres gracias de todo corazón por darme esta oportunidad y creer en mí desde el primer momento. Yo tengo claro que no me equivoqué con las decisiones tomadas y espero que este sentimiento sea mutuo. Concha gracias por enseñarme tu visión de la ciencia, por esas discusiones sobre los resultados en las que he podido aprender que uno deber ser el primero en criticar y dudar de su trabajo y sobre todo gracias por tu gran apoyo y cariño en momentos difíciles. Mª José contigo me he sentido siempre como en casa, has sabido darme siempre el consejo y el apoyo que he necesitado en cada momento y la libertad para expresar y decidir que camino seguir, gracias por tu cariño y comprensión. Agus, para mi eres todo un ejemplo a seguir, trabajar contigo ha sido un placer, eres una persona optimista y amante de la ciencia y consigues contagiar ese sentimiento a todos los que te rodean. Gracias por tus miles de consejos, sobretodo me he quedado con dos "no me des los peces, enséñame a pescar" y "esto es una carrera de fondo así que tienes que llegar al equilibrio entre el experimento y la cerveza para llegar a la meta", creo que encontré el equilibrio o por lo menos la carrera la he acabado, muchas gracias, jefe, compañero, empresario y amigo.

Me gustaría también agradecer muy especialmente a los secretarios y técnicos del departamento por su inestimable ayuda, no siempre se reconoce la gran labor que realizan pero sin duda son parte del motor interno que hace que funcione está gran maquinaría y sin ellos, estaríamos perdidos en muchas ocasiones, por ello Esther, Juan Cuadrado, Ana (mi Anita), Elisa, Concha, Paco, Jaime, Quique, David Carpena, Olga, Isidro, Eduardo y Germán, un millón de gracias. Especialmente quiero agradecer a Quique, Germán y Ana, ya que no solo han hecho más fácil mi vida en innumerables ocasiones, sino que además me han dado su cariño, su amistad y hemos compartido momentos inolvidables, ya sabéis que tenéis todo mi amor.

Por supuesto también quiero agradecer a todos mis compañero, no solo del grupo, sino del departamento por todos los momentos vividos, aquí se pasan muchas horas cada día, y al final terminamos siendo todos una gran familia. Quería mencionar especialmente a Jerónimo Juan "mi sensei" y a Angel Berenguer por todos sus consejos y ayuda, a JuanPi por ser como eres y afrontar todo con buen humor, a David San José mi asesor personal en el diseño de pósters y presentaciones, a mi Paquito por tu amistad dentro y fuera del trabajo, a Mayer mi ilicitana favorita y "gemela", a Eduardo Santillán "mi yanqui" no puedo expresar con palabras lo mucho que me gusto conocerte y el cariño que te tengo, gracias por ser como eres, a Erika por darme tu amistad y entenderme como soy y a Izaskún y Vero "mis becarias" ha sido un placer trabajar codo con codo con vosotras. Mención especial se merece el bando Colombiano (Franz, Robi, Aroldo, Johana, Ernesto...), sois muchos los que habéis pasado por aquí y gracias a conoceros y ver el amor que le tenéis a vuestra tierra, me habéis despertado curiosidad por ese país, así que espero verles a todos en un futuro allí. También me gustaría mencionar a "mis chicos" de Química Orgánica, a pesar de ser de diferentes departamentos hemos compartido y vivido mucho juntos y os llevo en el corazón, especialmente a Santi, Henoc y Dani, por mimarme, por quererme como soy y porque sin vosotros estos años no habrían sido lo mismo. A Néstorcillo por tu amistad y cariño.

Franzito, mi pechu, que te puedo decir a ti que ya no sepas, definitivamente no me imagino todos estos años sin ti a mi lado, ayudándome, dándome tu amistad y haciéndome reír, te quiero! Tu, Javi y Quique sois lo mejor que me llevo con diferencia del paso por el departamento. Javi, sigo sin entender porque tienes que recoger a todos los "animalitos" del mundo, jeje, aunque bueno es parte de ti y de tu naturaleza.

No puedo pasar sin escribir unas palabras a todas las personas que me han acompañado en congresos, han sido muchos y buenos momentos y me llevo un gran recuerdo de todos ellos. Lived, Maria, Avelina, Cristina y Vero, mis compañeras de habitación en todos ellos, cuantas historias se podrían contar y cuantos momentos para recordar y para olvidar… Antonio y Avelina, yo creo que ninguno olvidará jamás ese congreso en Belfast, y tantos otros que hemos pasado, ha sido maravilloso poder compartir con vosotros y me llevo una gran amistad. Agus, aún no me queda claro si era magnesio o manganeso… pero bueno nos reímos. A todas y cada una de las personas que vivieron "momentos congreso" conmigo gracias por hacerlos especiales.

I would like to thank Professor Bert Weckhuysen for letting me work in his research group of the Debye Institute for Nanomaterials Science of Utrecht University. Also, Andy Beale, Satu Korhonen and Upakul Deka, one million thanks for all your help and your huge patience with me, particularly with "my English". Thanks to all the master students, Ph.D. students, postdocs and technicians, all of you made me feel as home from the first second and this is something really important when you are 2000 km far away from home. Last but not least, thank to Upa, Luis, Javi and Sandra for being my family in Utrecht and take care of me, your friendship was more important than ever in these times.

En estos años, he tenido la oportunidad de compaginar mis tareas científicas con tareas educativas gracias a Nuria Grané Teruel, gracias por la confianza depositada en mi y sobre todo gracias por brindarme tu amistad. Eres una persona que se preocupa por la gente y que intenta mejorar las cosas cada día, sigue así con ese espíritu que te caracteriza y con esa gran calidad humana. Darles las gracias a todo el equipo decanal (actual y anterior) y a la secretaría de la facultad y de decanato, especialmente a Almudena que no solo te soluciona la vida, literalmente, sino que además lo hace con una sonrisa siempre en la boca.

A los servicios técnicos de investigación de la Universidad de Alicante, por su profesionalidad y su rapidez en todo momento.

A mis niñas de siempre, Wink, Ague, Vicky, Gema, Irenufa, Natalia, Cristina, Victoria y Bea, que hubiera sido de mí sin esos jueves "golfos". Gracias por estar ahí ahora y siempre, os quiero! A Pedro y Rosa por estar ahí en cada momento importante y a Raúl por su gran apoyo en toda mi andadura científica, gracias de corazón.

A mi familia, tíos, primos, por supuesto a mis hermanas Fanny y Alba, y como no a la razón de que hoy este aquí, mis padres, Manolo y Marga. Es tanto el apoyo y el amor que he recibido y recibo de vosotros, es tal el orgullo que veo en vuestras miradas, que solo puedo agradeceros que estéis ahí conmigo, soy lo que soy gracias a vosotros.

To my Emiel, thanks for change my whole life, for show me others ways, for your help in every moment and for your love. Ik hou van je nu en voor altijd.

Por último me gustaría agradecer a unas de las personas más especiales que ha pasado por mi vida, un ejemplo a seguir, una persona buena, respetuosa, divertida y un apoyo incondicional para mi, mi abuelo Manolo. Era la única persona que siempre en cualquier situación ha conseguido robarme una sonrisa y me hacía ver y tomarme la vida de otra manera. Esta tesis te la dedico a ti abuelo, sé que estarías conmigo al igual que has estado en todos los momentos importantes de mi vida, para mostrarme tu amor y tu apoyo. Te quiero y te echo de menos todos los días.

A todas las personas que aunque no haya nombrado saben que tienen un trocito de mi corazón, GRACIAS!

A mi abuelo

Contents

SUMMARY

This thesis presents the results of the study about CeO_2-supported Rh catalysts for the reaction of N_2O decomposition and it is structured in seven chapters. **Chapter I** describes the environmental problems associated with the N_2O emission to the atmosphere, the main anthropogenic sources and the current European legislation for this greenhouse gas control. **Chapter II** describes the procedure to prepare the catalysts used in this research, the techniques for their characterization and the experimental devices employed to carry out the catalytic tests. The following four chapters (chapters III to VI) are dedicated to the presentation and discussion of experimental results, and the final chapter (chapter VII) summarizes the major conclusions.

Chapter III studied N_2O decomposition catalysts consisting of Rh, Pd and Pt supported on γ-Al_2O_3, CeO_2 and CeO_2 doped with La or Pr. The catalytic activity for N_2O decomposition of the noble metal catalysts followed the trend Rh > Pd > Pt, and the support significantly affected the activity. A correlation between the reducibility of the support (by H_2) and activity of the noble metal/ceria catalysts for N_2O decomposition was found. The following publication describes the results of this study: S. Parres-Esclapez, M.J. Illán-Gómez, C. Salinas-Martínez de Lecea, A. Bueno-López. **On the importance of the catalyst redox properties in the N_2O decomposition over alumina and ceria supported Rh, Pd and Pt.** Applied Catalysis B: Environmental 96 (2010) 370.

The N_2O decomposition mechanism on Rh/CeO_2 and Rh/γ-Al_2O_3 catalysts was studied by pulse techniques with isotopic gases and by *in-situ* spectroscopies in **chapter IV**. The higher catalytic activity shown by Rh/CeO_2 is related to the Rh-CeO_2 interaction and to the participation of the CeO_2 support in the N_2O decomposition mechanism. The CeO_2 support interacts strongly with Rh, partially stabilising cationic species of the noble metal during N_2O decomposition. By contrast, rhodium in Rh/γ-Al_2O_3 is reduced to Rh^0 under reaction conditions and N_2O decomposition mainly occurs via the Eley-Rideal mechanism. The results of this chapter were published in the article: S. Parres-Esclapez, J. Such-Basañez, M.J. Illán-Gómez, C. Salinas-Martínez de Lecea, A. Bueno-López. **Study by isotopic gases and *in situ* spectroscopies (DRIFTS, XPS and Raman) of the N_2O decomposition mechanism on Rh/CeO_2 and Rh/γ-Al_2O_3 catalysts.** Journal of Catalysis 276 (2010) 390.

In **chapter V** the activity of a Rh/CeO_2(Pr)/γ-Al_2O_3 catalyst was studied in simulated nitric acid plants streams. The catalyst activity is inhibited in the presence of O_2, H_2O and NO. Despite the inhibition, the catalyst has a good activity for N_2O decomposition, achieving total conversion at 500 ºC which would be high enough for practical application. Diffuse Reflectance Infrared Fourier Transform Spectroscopy (DRIFTS) experiments were performed to study the inhibiting effect of H_2O and NO. The results of this chapter have been submitted for publication with the title "**Preparation and characterization of γ-Al_2O_3 particles-supported Rh/$Ce_{0.9}Pr_{0.1}O_2$ catalyst for N_2O decomposition in the presence of O_2, H_2O and NOx.**"

Chapter VI presents the results of a Rh/CeO_2(Pr)/γ-Al_2O_3 catalyst, tested for N_2O decomposition in a nitric acid plant. The catalyst is active enough to ensure 100% N_2O removal under typical industrial reaction conditions and it maintains high catalytic activity for N_2O decomposition during 40 hours of operation, at least. The characterization of fresh and used catalysts by different techniques revealed that the main physico-chemical properties of the catalyst do not change during the N_2O decomposition tests.

CHAPTER I

Introduction: Global Warming and N_2O Emissions

This chapter describes the environmental problems associated with N_2O, its main anthropogenic sources and the current European legislation for this gas. Additionally, a review of the main catalysts used for N_2O removal, including previous work performed in the Carbon Materials and Environment research group (MCMA) is presented.

1.1. Introduction

1.1.1. Greenhouse effect and global warming

The climate is strongly affected by changes in the atmospheric concentration of certain gases that trap infrared radiation from the surface of the Earth. As outlined in Figure 1, a fraction of the solar radiation that is reflected at the surface does not penetrate the atmosphere. This is due to the presence of gases like water vapour and carbon dioxide, which absorb this radiation and return it to the earth's surface, causing a phenomenon known as the greenhouse effect. The greenhouse effect is the natural process by which the atmosphere traps some of the Sun's energy, warming the Earth enough to support life. Without this natural "greenhouse effect," temperatures on earth would be about 33 ºC lower and life as we know it today would not be possible [1-3].

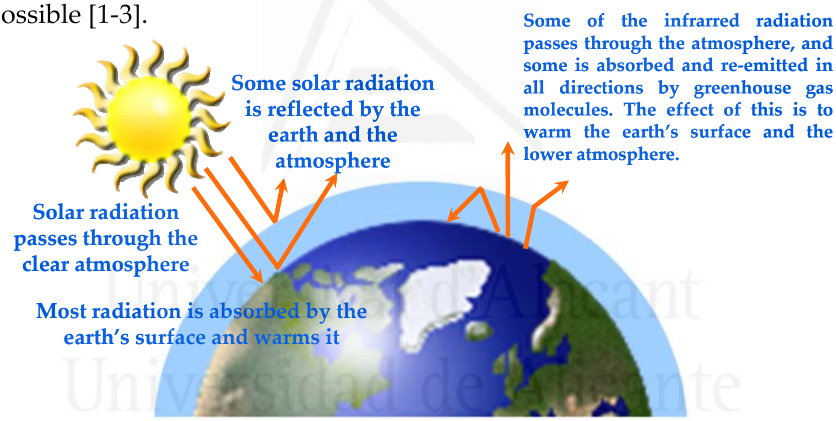

Figure 1. Schematic representation of the surface radiation retention responsible for the greenhouse effect.

During the past century, humans have substantially increased the amount of greenhouse gases in the atmosphere (*e.g.* by burning fossil fuels and deforestation). These gases are enhancing the natural greenhouse effect, and very likely to contribute to an increase in average global temperature and the related climate changes. The strategies used to reduce the greenhouse effect have focused mainly on the removal of CO_2 which is, by volume, the major greenhouse gas. However, the effect of other greenhouse gases, such as methane, nitrous oxide (N_2O) and halogenated compounds (such as chlorofluorocarbons (CFCs) and perfluorocarbons (PFCs)) has been also considered in recent years.

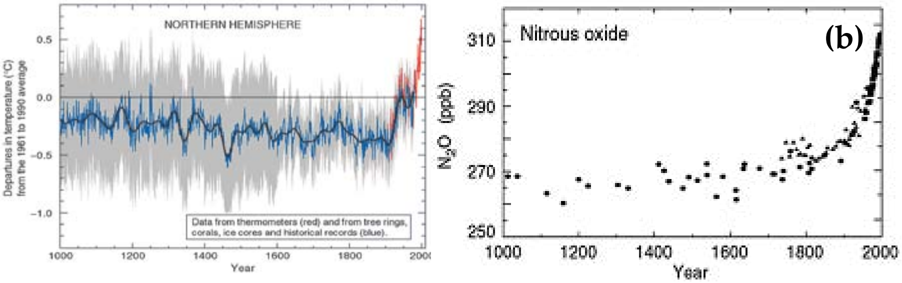

Figure 2. (a) Variation´s of the Earth´s surface temperature for the past 1000 years, (b) Indicators of the human influence on the N_2O atmosphere concentration during the industrial era. (Information provided by IPPC (Intergovernmental Panel on Climate Change) [4]).

In relation with climate change, the long-term data sets for global temperature, shown in Figure 2a, indicate a clear and consistent increase of the global temperatures, mainly since the Western countries industrial revolution. Large variations, resulting from special events, such as volcanic eruptions, cause the short term trend in global temperature change to be difficult to analyze, but the long term analysis of the data sets allows a wider picture to be analyzed. Much of the argument surrounding climate change hinges not on whether global warming is occurring, but rather whether this warming is a result of human activity. Natural causes, such as sun-spot activity, have been invoked to explain the accelerated rate of global warming in recent decades. However, recently the important role of human generated greenhouse gas emissions has been largely recognised, even by those who were previously sceptical about human-induced global warming in climate change. As the concentration of the main greenhouse gases in the atmosphere increased, global temperatures increased at a similar rate. Figure 2b shows indicators of the human influence on N_2O emission. Since the industrial revolution, the levels of carbon dioxide, methane and nitrous oxide have increased dramatically. Fossil fuel combustion, increasingly more intensive agriculture and an expanding global human population have been the primary causes for this rapid increase.

The rapid increase in greenhouses gas emissions observed during the last 250 years is expected to continue for several decades. Various scenarios have been examined, depending on factors such as fuel use and efficiency and even in the best possible scenario, a further increase in greenhouses gas is predicted until about 2040. If the predictions in the greenhouse gas concentrations are translated into temperature changes, a global temperature increase between 1 and 5.5 Celsius degrees is expected for 2100 (Figure 3). The average predicted temperature increase over the next 100 years is about 3 ºC which is about 1 ºC higher than what is predicted to be caused only by man-made greenhouse gas emissions. The large discrepancy between predictions of different scenarios underlines the difficulty involved in making such predictions and the large uncertainty inherent to climate change models. Even though the complexity of the predictions, there is still reason to believe that global warming is taking place and is due to human interaction.

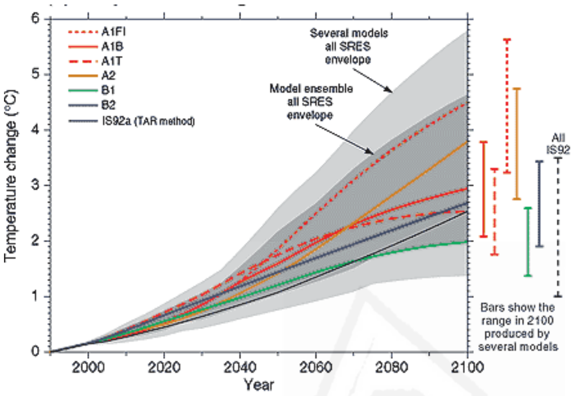

Figure 3. Predictions for the evolution of temperature change (Information provided by IPPC [4]).

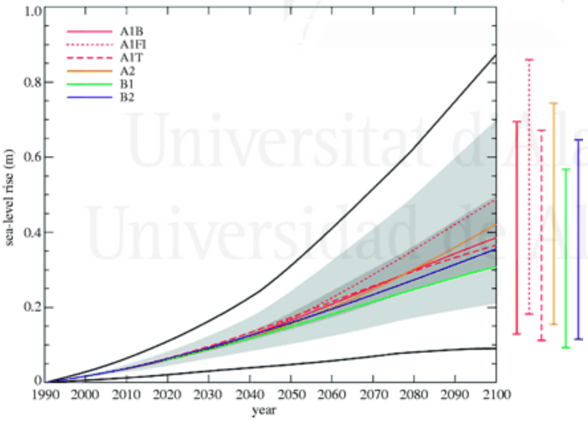

Figure 4. Predictions for the evolution of sea level rise. (Information provided by IPPC [4]).

A common feature of global warming effects is that average sea level is rising (Figure 4). The sea level rise, due to the thermal expansion of water and melting ice around the world, is a serious potential threat to millions of people. As for temperature changes, predictions vary widely: from 20 cm to 60 cm.

Recently, the scientific community has recognized that it is vital to determine how far the adverse impacts of climate change can be reduced through control measures. The time that it would cost to outline a key action policy is also important, as there is a long delay between the reduction in the emission of greenhouse gases and stabilization of atmospheric concentrations.

1.1.2. N_2O emissions

The present research work is focused on the problem of N_2O emissions to the atmosphere. N_2O is naturally produced by biological processes that occur in soil and water and by a variety of anthropogenic activities related with agricultural, energy-related, industrial, and waste management fields. N_2O was considered innocuous for a long time, but now we know it contributes to the ozone layer depletion and to global warming. For these effects, N_2O is much more harmful than CO_2. Even though total N_2O emissions are much lower than CO_2 emissions, N_2O is approximately 300 times more powerful than CO_2 at trapping heat in the atmosphere [5]. Since 1750, the global atmospheric concentration of N_2O has risen by approximately 18 percent (IPCC 2007). The annual emission of N_2O to the atmosphere due to anthropogenic activities is estimated at 8 million tons. Some scientists suggest that the anthropogenic emissions should be reduced by 70-80% to achieve a zero balance between the N_2O emitted into the atmosphere and that the planet is able to eliminate by natural means. Thus, the control of the anthropogenic N_2O emissions that is needed is estimated to be equivalent, from the point of view of greenhouse effect, to the CO_2 emissions decrease signed in the Kyoto agreement.

Figure 5 shows the sources of N_2O emissions. From the figure it can be observed that the main activities that contribute to N_2O emissions are agricultural soil management, fuel combustion in motor vehicles, manure management, nitric and adipic acids production and stationary fuel combustion. The increased use of catalytic converters in gasoline engine cars around the world has led to an increase in transport related nitrous oxide emissions, because they substantially reduce emissions of nitrogen oxides (NO and NO_2), carbon monoxide and hydrocarbons, but release a certain amount of nitrous oxide, as a result of catalyst aging.

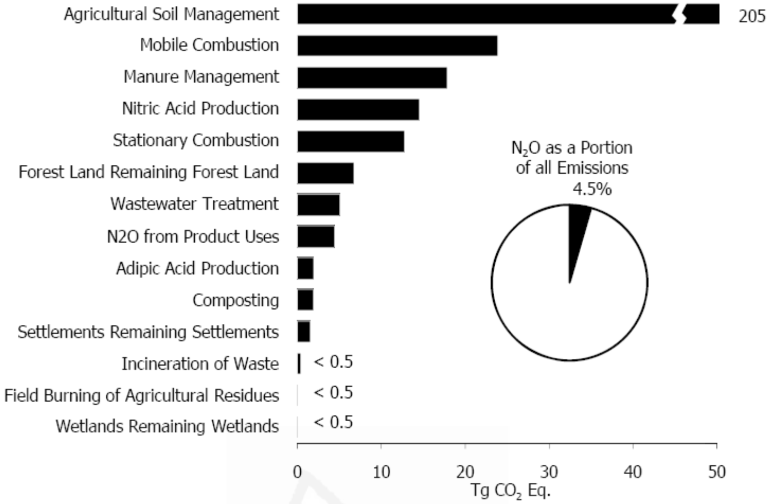

Figure 5. 2009 Sources of N2O Emissions in CO2 equivalent Teragrams. (Information provided by EPA (Environmental Protection Agency) [6]).

In this study Rh/CeO2 catalysts have been studied and tested for N2O decomposition in nitric acid plants. Nitric acid is obtained in an industrial process with several steps, and first one is the catalytic oxidation of ammonia. During this reaction, N2O is formed as a by-product and it is released to the atmosphere. Currently, the nitric acid industry uses control system for NO and NO2 emissions (NOx). The systems used are a combination of non-selective catalytic reduction (NSCR) and selective catalytic reduction (SCR) technologies. During NOx removal in NSCR systems, an effective N2O removal also takes place. However, NSCR units are generally not preferred in modern plants because of a high energy costs and alternative strategies are required.

1.1.3. Legislation

At present there is no regulation for N2O emissions to the atmosphere. As described in section 1.1.2, these emissions come largely from adipic and nitric acid plants. 500-600 nitric acid plants are thought to be in operation world-wide, an approximately 100 of them are located in Europe. It is difficult to get accurate data on the number of plants and on the total amount of nitric acid produced annually because these plants are often integrated into larger chemical facilities.

In Europe, in order to support the implementation of the "Integrated Pollution Prevention and Control Directive" (EC 2008a), the European Commission (EC) published in 2007 guidelines on Best Available Technologies (BAT) that set a benchmark of 2.5 kg of N_2O or less N_2O abatement per tonne of nitric acid in new nitric acid production plants and 4 kg per tonne of nitric acid for existing plants (EC 2006). For EU Directives to be enforceable, they have to be integrated into national legislation by the respective member states. However, not all EU countries have adopted this legislation and it is unclear how many member states are actually enforcing this directive. In all EU member countries, except for Greece and Italy, some type of N_2O abatement is either required through to the European Union Emissions Trading Scheme (EU-ETS) (Austria, the Netherlands, Norway, United Kingdom) (EC 2008, 2009a), or it is possible to voluntarily abate and earn credits through Joint Implementation (JI). Furthermore, two (non-JI) pilot projects were implemented in Norway and Austria as part of their national climate policy. All EU nitric acid plants will be included in the third phase of the EU-ETS and benchmark emission levels of around 0.8 kg of N_2O per tonne of nitric acid are currently being discussed between the EU member states and the EU Commission's Climate Action. The main problem with applying these regulations is the high costs involved in its implementation [7].

1.1.4. Catalytic decomposition of N_2O

To prevent N_2O emission to the atmosphere, the most effective solution is to use catalysts that allow decomposition to N_2 and O_2 or to facilitate the reaction with a reducing agent.

N_2O decomposition is an exothermic reaction, but it presents Kinetic restrictions at low temperature:

$$2N_2O \rightarrow 2N_2 + O_2 \qquad \Delta H^{o}(25\ ^{o}C) = -163\ kJ/mol$$

Figure 6 shows a diagram of the N_2O molecule, indicating some of their bond properties.

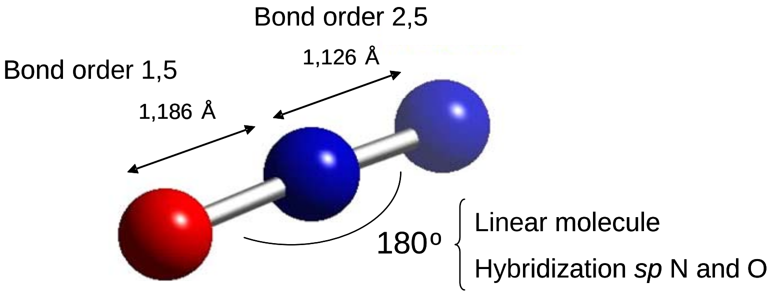

Figure 6. Bond properties of the N_2O molecule.

In the asymmetric N_2O molecule, the N-N bond order is 2.5 while that of N-O is 1.5, making the N-O bond the easiest to break. The activation energy for thermal dissociation of the N-O bond is about 250-270 kJ/mol, and temperatures above 625 ºC are required for significant rates. Good N_2O decomposition catalysts consist of metal particles that donate electrons into the antibonding orbital of the N-O bond, weakening it and lowering the activation energy of the process. N_2O removal is favoured by the presence of reducing species such as CO or hydrocarbons.

A wide number of catalysts have been proposed for N_2O decomposition including supported and unsupported metals, pure and mixed oxides, and zeolitic systems [5,8-11]. Metal based catalysts, which include Pt, Pd, Ag, Au and Ge, are generally active only above 375 ºC. For pure oxides catalysts, the highest activities are exhibited by the transition metal oxides of group 9 (Rh, Ir, Co, Fe, Ni), CuO and by some rare earth oxides such as La_2O_3. As stated by Kapteijn et al. [5], supported oxides are not as frequently studied as pure and mixed oxides, but for practical applications they could be the most suitable due to their higher dispersion by combination with a large specific surface area support.

The activity of many N_2O decomposition catalysts is inhibited by oxygen due to either reversible dissociative or molecular adsorption of oxygen on the catalyst active sites. Other gases, such as H_2O, NO, SO_2, CO, CO_2 and halogens, that can be present along with oxygen in real N_2O-containing industrial streams, also inhibit the catalysts due to reversible competitive adsorption, irreversible poisoning or because involve the catalysts in parallel reactions [11,12]. Therefore, it is necessary to develop active catalysts for N_2O decomposition that are able to maintain high catalytic activity in the presence of the typical inhibitors.

Analysis of the published information on the subject suggests that metal catalysts or metal oxides combining active metals, for example, Rh_2O_3 with active support such as CeO_2 (pure and doped) can be interesting for the N_2O decomposition. It has to be underlined that this type of support has proven highly effective in other applications, such as NOx reduction with CO and hydrocarbons [13,14]. Therefore, this research work is focused on studying N_2O decomposition catalysts consisting of noble metals supported on cerium oxide.

1.1.5. Previous background of the MCMA group in the topic of this thesis

In the MCMA group (Carbon Materials and Environment research group) of the Department of Inorganic Chemistry, University of Alicante, where this research has been developed, intensive work has been done on the development of Pt catalysts for selective catalytic reduction NOx (NO + NO_2) from exhaust diesel engines streams. As a result of these studies efficient Pt catalysts have been prepared for NOx removal [15-17]. However, one of the disadvantages of these Pt catalysts is the high production of N_2O as a product of the NOx reduction process.

Figure 7 shows, as example, the results obtained using a Pt/Al_2O_3 catalyst for NOx reduction with propene in a real diesel engine exhaust stream. The data indicate that only about 20% of NOx is reduced with propene to produce N_2 and N_2O as the main reduction products.

As a solution for this problem, the use of a dual catalytic bed was proposed. In the first bed, a platinum catalyst was used to reduce NOx. In the second bed, a Fe-based catalyst decomposes N_2O formed in the first stage [18]. The main drawback of this system is that the second bed operates at a higher temperature than the first one. So, for a practical application, the heating of gas stream is required, which results in extra fuel consumption. The optimal conditions for the dual bed catalysts would be achieved when both beds operate in a similar temperature window, which has to be close to the temperature range of gases in the diesel engine exhaust. These conditions would avoid exhaust stream heating and, consequently, the system would be easier to use.

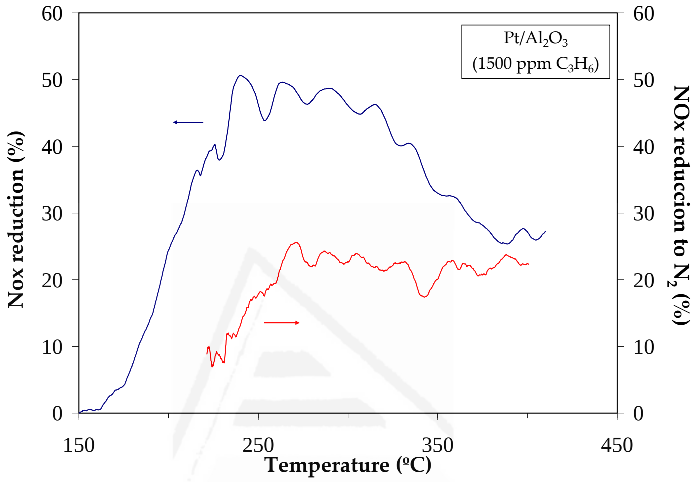

Figure 7. Activity and selectivity of a catalyst Pt/Al_2O_3 for selective catalytic reduction of NOx with propene in the exhaust of a diesel engine [15].

Thus, in order to optimize the formulation of the active phases of the N_2O decomposition catalyst in the described conditions, research work using rhodium catalysts supported on ceria was initiated. In a previous study conducted in the MCMA group [10] catalysts of rhodium supported on pure and doped cerium oxides were used for N_2O decomposition and Figure 8 summarizes (as and example) some of the results [10]. The figure illustrates the high activity shown by these catalysts, and for instance, around 50% N_2O decomposition is achieved at 225 °C.

It was concluded that the nature of the support is crucial for the activity of rhodium-based catalysts and rhodium supported on solid solutions of cerium and praseodymium ($Rh/CeO_2(Pr)$ or lanthanum ($Rh/CeO_2(La)$) were the most active catalysts. The improvement in the activity of rhodium when is supported on a suitable ceria carrier seems to be related with the redox properties of the support that allows the noble metal to be in an oxidized form, increasing its catalytic activity [10].

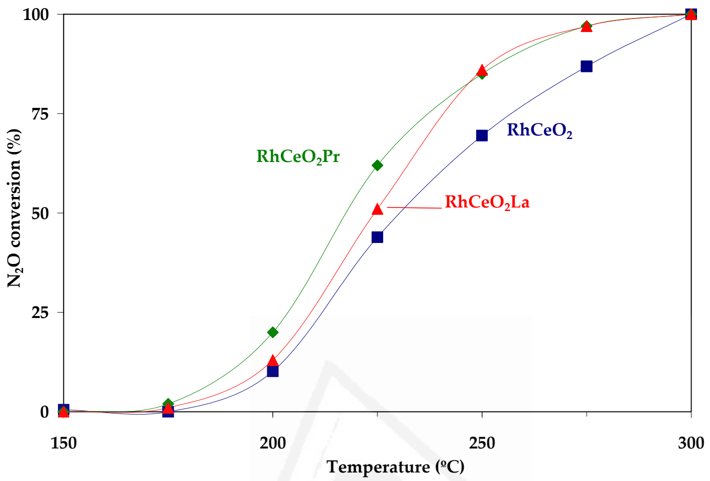

Figure 8. Previous results of decomposition of N_2O with rhodium catalysts supported on different oxides and mixed cerium pure [10].

These previous results suggested that rhodium catalysts supported on doped cerium oxide could be an interesting option for low and mild temperature N_2O removal. Currently, these types of catalysts are being investigated by researchers of the MCMA group to solve the problem of N_2O emissions in SCR systems for diesel vehicles. In addition, the promising results previously obtained lead us to think that these catalysts could be also useful for some other N_2O sources, and this thesis is focused both on the study of the N_2O decomposition mechanism on rhodium/ceria catalysts and to its application in nitric acid plants.

1.1. Objectives

Taking into account the above described background, the overall objective of this work is to develop an effective catalyst for N_2O removal from gas streams. The specific objectives are:

- Studying the catalytic decomposition of N_2O using Rh, Pd and Pt supported on alumina, ceria and ceria doped with La or Pr. The purpose is to try to correlate the catalytic activity on laboratory scale experiments with the chemical and physical properties of the materials.

- Determining the effect of the support on the mechanism of N_2O decomposition, using Rh/CeO_2 and $Rh/\gamma\text{-}Al_2O_3$ catalysts. To achieve this, steady state catalytic decomposition experiments at the laboratory scale, estimation of kinetic parameters, characterization by X-ray Photoelectron Spectroscopy (XPS) under reaction conditions and experiments under transient conditions using the isotopic gas pulses technique, have been combined.

- Supporting the most suitable active rhodium/ceria phase on alumina particles and to study the catalyst physicochemical properties, the Ce-Al interaction and the influence of different poisons (O_2, H_2O and NO_x) in the performance of this supported catalysts.

- Analysing the performance of a $Rh/CeO_2(Pr)/\gamma\text{-}Al_2O_3$ catalyst for N_2O decomposition in a real nitric acid plant gas stream, and the characterization of the catalyst before and after the catalytic tests, in order to identify potential changes in the catalyst physicochemical properties.

References

[1] C. Baird. Química Ambiental. Reverté (2001).
[2] T.G. Spiro, W.M. Stigliani. Química Medioambiental. Pearson Prentice Hall (2005).
[3] http://www.ghgonline.org/index.htm "acces in September 2011"
[4] European Climate Change Programme:
http://ec.europa.eu/environment/climat/eccp_review.htm
"acces in September 2011"
[5] F. Kapteijn, J. Rodriguez Mirasol, J.A. Moulijn. Appl. Catal. B, 9 (1996) 25.
[6] INVENTORY OF U.S. GREENHOUSE GAS EMISSIONS AND SINKS: 1990 – 2009. APRIL 15, 2011. U.S. Environmental Protection Agency.
[7] J. Pérez-Ramírez. Appl. Catal. B 70 (2007) 31.
[8] H.S. Gandhi, G.W. Graham, R. McCabe. J. Catal. 216 (2003) 433.

[9] S.J. Lee, I.S. Ryu, B.M. Kim, S.H. Moon. Int. J. Greenhouse Gas Control 5 (2011) 167.

[10] A. Bueno-López, I. Such-Basáñez, C. Salinas-Martínez de Lecea. J. Catal. 244 (2006) 102.

[11] J. Oi, A. Obuchi, G.R. Bamwenda, A. Ogata, H. Yagita, S. Kushiyama, K. Mizuno. Appl. Catal. B 12 (1997) 277.

[12] J. Pérez-Ramírez, F. Kapteijn, K. Schöffel, J.A. Moulijn. Appl. Catal. B 44 (2003) 117.

[13] J. Kăspar, P. Fornasiero, M. Graziani. Catal. Today 50 (1999) 285.

[14] S. Bernal, G. Blanco, J.J. Calvino, J.M. Gatica, J.A. Perez-Omil, J.M. Pintado. Top. Catal. 28 (2004) 31.

[15] G. Garrigós-Pastor, S. Parres-Esclapez, A. Bueno-López, M. J. Illán-Gómez, C. Salinas-Martínez de Lecea. Appl. Catal. A 354 (2009) 63.

[16] A. Bueno-López, M.J. Illán-Gómez, C. Salinas-Martínez de Lecea. Appl. Catal. A 302 (2006) 244.

[17] A. Bueno-López, D. Lozano-Castello, I. Such-Basáñez, J.M. Garcia-Cortes, M.J. Illan-Gomez, C. Salinas-Martínez de Lecea. Appl. Catal. B 58 (2005) 1.

[18] J. Pérez-Ramírez, J.M. García-Cortés, F. Kapteijn, M.J. Illán-Gómez, A. Ribera, C. Salinas-Martínez de Lecea, J.A. Moulijn. Appl. Catal. B 25 (2000) 191.

CHAPTER II

Materials, Experimental Methods and Characterization Techniques

This chapter describes the preparation of the catalysts used in this research work, the techniques applied for their characterization and the experimental devices used for the catalytic tests.

2.1. Introduction

This chapter describes the materials, characterization techniques and experimental methods used in this research. Firstly, a description of the preparation method used for cerium, praseodymium and lanthanum mixed oxides and for the final catalysts is presented. Secondly, the characterization techniques employed to study the physicochemical properties of different materials and the experimental devices used to perform catalytic N_2O decomposition tests are introduced.

2.2. Materials

In this study both powered and supported catalyst were prepared and tested. The powdered catalysts were tested at laboratory scale to obtain the results presented and discussed in chapters III and IV. A supported catalyst, where the active phase was loaded on alumina particles, has been used for catalytic tests performed both at laboratory scale and in a nitric acid production plant, and the results obtained are discussed in chapter V and VI, respectively.

For the preparation of the catalysts, commercial γ-Al_2O_3 pellets (Alfa Aesar. 78 m^2/g), $Ce(NO_3)_3{\cdot}6H_2O$ (Sigma Aldrich, 99,99%), $La(NO_3)_3{\cdot}6H_2O$ (Sigma Aldrich, 99,99%), $Pr(NO_3)_3{\cdot}6H_2O$ (Sigma Aldrich, 99,9%), $Pt(NH_3)_4(NO_3)_2$ (Sigma Aldrich, 99,995%), $Rh(NO_3)_3$ (Sigma Aldrich, 99,9%) and $Pd(C_2H_3O_2)_2$ (Sigma Aldrich, 99,98%) were used.

2.2.1. Preparation of powder catalysts

Bare CeO_2 and 10 wt.% La or Pr doped-CeO_2 supports were prepared. The required amounts of the metal precursors were physically mixed in a mortar and calcined in static air at 600 ºC for 90 min (heating rate 10 ºC/min). The bare, La doped and Pr doped-ceria supports are denoted by CeO_2, CeO_2(La) and CeO_2(Pr), respectively. Commercial γ-Al_2O_3 pellets were crushed and the fine powder obtained was also used as support. This support is denoted by γ-Al_2O_3.

These four supports were impregnated using a water solution of $Rh(NO_3)_3$, $Pt(NH_3)_4(NO_3)_2$ or $Pd(C_2H_3O_2)_2$, dried at 200 ºC and calcined at 500 ºC for 2 hours. The target content of noble metal in the catalysts after the calcinations step was 0.5 wt. %. The nomenclature of the catalysts includes "Rh, Pt or Pd" before the support notation.

2.2.2. Preparation of supported catalyst

The Ce and Pr precursors were loaded on γ-Al_2O_3 particles (0.4-0.71 mm; crushed and sieved from commercial pellets) by incipient wetness impregnation using a water solution of $Ce(NO_3)_3 \cdot 6H_2O$ and $Pr(NO_3)_3 \cdot 6H_2O$. After drying at 110 ºC, the impregnated particles were calcined in static air at 600 ºC for 90 min (heating rate 10 ºC/min). The amounts of Ce and Pr precursors used were those required to obtain 50 wt.% $Ce_{0.9}Pr_{0.1}O_2$ + 50 wt.% γ-Al_2O_3. This sample is denoted by $CeO_2(Pr)/\gamma$-Al_2O_3.

$CeO_2(Pr)/\gamma$-Al_2O_3 was impregnated using a water solution of $Rh(NO_3)_3$ and subsequently dried at 200 ºC and calcined at 500 ºC for 2 hours. The target content of noble metal in the catalysts after the calcination was 0.5 wt. % of the cerium and praseodymium mixed oxide (0.25% in total basis). The nomenclature of the catalyst is $Rh/CeO_2(Pr)/\gamma$-Al_2O_3.

2.3. Characterization techniques

Information about the chemical and physical properties of the catalysts allows identifying the key factors that determine the catalysts performance, including the composition, structure and surface distribution of the active phase. To obtain this information, the following experimental techniques were used: N_2 physisorption, X-ray Diffraction (XRD), X-ray Photoelectron Spectroscopy (XPS), Raman Spectroscopy, Temperature Programmed Reduction with H_2 (H_2-TPR), Transmission Electron Microscopy (TEM), Scanning Electron Microscopy (SEM) and Diffuse Reflectance Infrared Fourier Transform Spectroscopy (DRIFTS). A detailed description of the techniques and equipment used is presented below.

2.3.1. N_2 physisorption at -196 ºC

The physical adsorption (or physisorption) of gases and vapors is one of more used techniques to study the porous texture of solids. The objective is to obtain adsorption isotherms that allow calculating the specific surface area, the porosity and the pore size distribution of a solid.

When a gas (adsorbate) is in contact, at a certain pressure and temperature, with a porous solid (adsorbent), the solid adsorbs the gas, increasing its weight and decreasing the gas pressure in the container. Once the equilibrium is reached, the pressure will be constant and the amount of gas adsorbed at a determinate temperature and pressure can be calculated if both the weight gain (gravimetric techniques) and the pressure loss are registered. The adsorbate must to be chemically inert, to have a relatively high saturation pressure, and to have a near-spherical shape to minimize the difficulty for calculating the molecule cross section. N_2, CO_2, Ar, He, CH_4 and H_2O are examples of suitable adsorbate molecules. N_2 (at its boiling point (-196 ºC)) is the most frequently adsorbate used to obtain adsorption isotherms [1, 2].

Figure 1. Equipment for obtaining N_2 gas adsorption isotherms at -196 ºC.

The equipment employed for the physisorption measurements was a Autosorb-6B, from Quantachrome, which is shown in Figure 1. The system consists of two units, a degassing unit and an adsorption unit. The degassing unit consists of a vacuum system and six independent furnaces. The samples used in this research work were degassed for 4 hours at 150 ºC. The degassed sample is moved to the physical adsorption unit, where all subsequent experimental steps take place. The measurement process is controlled by a computer. The steps include a vacuum step and a filling step during while different pressures of adsorbate ($0<P/P_0<1$, for N_2 at -196 °C) are supplied. The system is able to calculate the adsorbed gas volume at each relative pressure.

Several models can be used to analyze the data of adsorption isotherms and to determine the characteristic parameters of surface area, porosity and pore size distribution of the material [2]. The BET model (Brunauer, Emmet and Teller) is one of the most commonly applied:

$$\frac{\frac{P}{P_0}}{n\left(1-\frac{P}{P_0}\right)}=\frac{1}{n_m C}+\frac{(C-1)}{n_m C}\frac{P}{P_0} \tag{1}$$

where:
P is the pressure
P_0 is the saturation pressure
n is the number of moles adsorbed
n_m is the number of moles adsorbed in the monolayer
C is a parameter related to the heat of adsorption

By plotting $\frac{\frac{P}{P_0}}{n\left(1-\frac{P}{P_0}\right)}$ versus $\frac{P}{P_0}$, a linear relationship is obtained from which the values of C and n_m can be calculated. From the value of n_m the specific area of the material is determined by the following equation:

$$S=n_m\cdot a_m\cdot N_a\cdot 10^{-21} \tag{2}$$

where:
S = apparent surface area of the material (m^2/g).
a_m = area occupied by one adsorbate molecule (nm^2/molecule, in the case of N_2 at -196 ºC is 0.162 nm^2).
N_a = Avogadro's number ($6{,}023\cdot 10^{23}$ molecules/mol).

The BET equation is fulfilled in partial pressures between $0.05 < P/P_0 < 0.3$ [3].

2.3.2. *X-ray Diffraction (XRD)*

X-rays are electromagnetic radiation of short wavelength, between 10^{-5} and 100 Å approximately. For analytical purposes, wavelengths between 0.1 to 25 Å are usually employed. The interaction between the electric field of the X-ray radiation and the electrons of the materials causes dispersion. For a crystalline solid, the overlap of different wave fronts diffracted by successive layers of atoms can generate constructive and destructive interference. The kind of interference depends on the distance between the atomic planes in the crystal structure, the radiation wavelength and the incidence angle of such radiation on the surface of the solid.

In 1912, Bragg [4] demonstrated that for constructive interference:

$$n\lambda = 2d_{hkl}\sin\theta \tag{3}$$

Where d_{hkl} is the distance between the atomic planes, λ is the wavelength, θ is the angle of the diffracted X-ray beam with the surface normal and n is an integer number. For interference to occur d_{hkl} should be close to λ, and scattering centers (atoms or ions) must be regularly distributed in the space.

The representation of the radiation intensity after interaction with the sample as a function of incidence angle (usually 2θ) is called diffractogram and is characteristic of each crystal. XRD provides both qualitative and quantitative information about crystalline solids and indicates the structure and position of atoms within the structure [5].

The crystallinity of the sample can be deduced from the peaks position and peaks width, which decreases with increasing crystallinity, *i.e.* increasing the size of the crystal. The Scherrer equation (Equation 4), can be used to determine the average size of the crystals (D) for a crystalline solid:

$$D = \frac{K\lambda}{\beta\cos\theta} \tag{4}$$

where,
λ is the radiation wavelength used to obtain the diffractogram.
θ is the diffraction angle.
K is the Scherrer constant or form factor (for ceria has been proposed 0.94).
β is the peak width at half height expressed in radians.

However, the Scherrer equation, although widespread, does not take into account factors such as the crystalline perfection, glass bending, strain, etc., which also affect the width of the diffraction peaks [5]. These factors are very important in real solids with a large number of defects, such as doped cerium oxides used in this study. For these oxides anomalous values of crystal size are usually obtained by using the Scherrer equation. So, in order to obtain more accurate values, some other equations are required, and the use of the Williamson-Hall equation (equation 5) would be more appropriate:

$$\beta_{\mathrm{Total}} = \beta_{\mathrm{Size}} + \beta_{\mathrm{Strain}} = \frac{0.9 \cdot \lambda}{D \cdot \cos\theta} + \frac{4 \cdot \Delta d \cdot \sin\theta}{d \cdot \cos\theta} \qquad (5)$$

In this equation, β_{Total} is the peak width at half height, λ is the wavelength of the incident radiation, θ is the diffraction angle, D is the crystal size, and $\Delta d/d$ is the strain, defined as the deformation divided by the ideal size of the glass. The Williamson-Hall method can separate the contribution of the crystal size and strain, (caused by atoms that are not in their ideal positions in a non-uniform crystal), in the width at half peak height diffraction [6]. When $\beta_{\mathrm{Total}} \cdot \cos\theta$ is graph versus $4 \cdot \sin\theta$ the crystal size can be calculate from the intercept value and the tension value from the slope of the straight line [7].

In this work, XRD was used to analyze the crystal structure of the cerium oxides and to determine the average crystallite sizes. The crystal sizes were estimated using both the Scherrer equation (equation 4) and the Williamson-Hall equation (Equation 5).

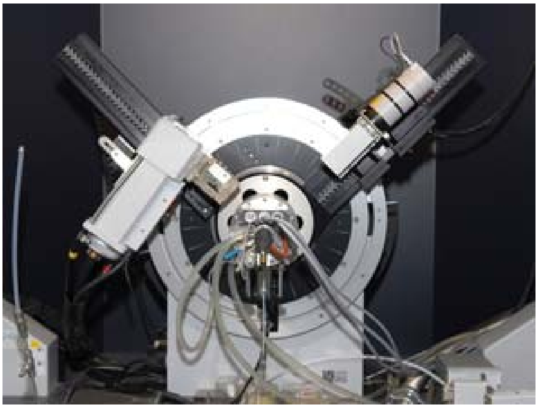

Figure 2. Powder diffractometer Seifert JSO-model DEBYEFLEX 2002.

The equipment used was a powder diffractometer Seifert JSO-DEBYEFLEX model 2002 that is equipped with a copper cathode and a nickel filter (λ = 1.5418 Å) (Figure 2). The X-ray diffraction patterns were recorded in a 2θ range from 20° to 80° with a step of 0.02° and time per step of 3 seconds. For alumina particles-supported catalysts, the particles were crushed and the powder was used to obtain the diffractograms.

2.3.3. X-ray photoelectron spectroscopy (XPS)

XPS is a surface analysis technique based on the kinetic energy required for the core electrons ejection from an atom when a sample is irradiated with an X-ray beam of a certain energy (about 1.4 KeV). Using this kinetic energy and the radiation energy the binding energy of the electron can be calculated. The binding energy depends on the atom and is affected by the oxidation state of a specie. This technique is quantitative, and allows obtaining reliable results for atomic surface composition and chemical nature of the surface species.

XPS spectra were obtained with a VG-Microtech Multilab 3000 spectrometer (Figure 3) equipped with a hemispherical electron analyzer with 9 channeltrons (with energy of 2-200 eV step) and Mg and Al X-ray radiation sources. Mg Kα radiation (1253.6 eV) was used, with the detector in constant energy mode and a pass energy of 50 eV. The pressure in the analysis chamber was maintained at $5 \cdot 10^{-10}$ mBar. The binding energy scales (BE) and Auger kinetic energy (KE) were established using the C1s transition at 284.6 eV as reference.

The accuracy in the determination of BE (Binding Energy) and KE (Kinetic Energy) values is ± 0.2 and ± 0.3 eV respectively. The BE and KE values were obtained using the Peak-fit Program. The equipment was equipped with a pretreatment chamber with controlled atmosphere and temperature. Using this chamber XPS data were obtained before and after carrying out *in-situ* heat treatments. Data, after putting in contact the sample with a 1000 ppmN_2O/He stream for one hour at different temperatures (ranging between 250 ºC and 325 ºC), were obtained.

Figure 3. Multilab VG-Microtech spectrometer for XPS.

2.3.4. Raman spectroscopy

Raman spectroscopy is a powerful tool to study the dynamic structure of crystalline and non-crystalline materials.

When electromagnetic radiation interacts with a molecule, the oscillating electric field of the radiation causes an oscillation of the electron density in the molecule. This oscillation induces an oscillating electric dipole moment that acts, in turn, as a radiation source. This process is referred to as Rayleigh or Raman scattering. The radiation is emitted in all directions, except in the own dipole direction. The maximum scattered intensity, I_{max}, is given to a 90º to the axis of the dipole.

When visible light is used as a radiation source, the Raman spectrum typically resembles a vibrational spectrum and provides very similar information to that offered by conventional infrared spectrocopy. The vibrations reflected in the Raman spectrum are not the same, since the spectroscopy selection rules are different. A vibrational mode will be active in Raman spectroscopy if it is able to change the polarizability of the bond or of the molecule analyzed and, consequently, generate an induced dipole moment [8,9].

In this work, Raman spectroscopy has been used to obtain information about the structure of pure and doped cerium oxide. The equipment used was a dispersive Raman spectrometer (Bruker RFS/100 model) coupled to a microscope (Figure 4). This device uses a laser excitation source in the near infrared (1064 nm Nd-YAG) and a Ge detector cooled by liquid nitrogen [10].

Figure 4. FT-Raman spectrometer Bruker RFS/100.

The incident beam and the direction of measurement of the scattered radiation were at an angle of 180º, performing 64 scans for each spectrum at a laser power of 85 mW. To carry out the characterization experiments, the catalyst particles supported on alumina were adequately ground.

2.3.5. Temperature Programmed Reduction by H_2 (H_2-TPR)

Temperature Programmed reduction by H_2 is a technique to study the reduction process of oxidized species. To carry out the experiments a H_2 flow was used and the reduction was carried out in temperature programmed conditions, *i.e.*, increasing the temperature using a constant heating rate.

In this study, this technique allows us to determine the reducibility of the catalysts, which will be related to its catalytic performance.

Figure 5. Micromeritics chemisorbed Pulse 2705.

A Micromeritics chemisorbed Pulse 2705 (Figure 5) apparatus, which consists of a tubular U-shaped quartz reactor (5 mm internal diameter) coupled to a thermal conductivity detector was used to obtain the H_2-TPR profiles. Experiments were conducted using 20 mg of sample and a gas flow composed of 5 vol. % H_2 in Ar. The heating rate was 10 °C/min. To quantify the amount of H_2 consumed in the experiments CuO was used a as reference sample. The catalyst particles supported on alumina were ground to obtain the H_2-TPR profiles.

2.3.6. Transmission Electron Microscopy (TEM)

To carry out Transmission Electron Microscopy analysis [12,13], a thin film of sample (maximum thickness 100 nm, to be transparent to electrons) is irradiated with an electron beam of uniform current density with an energy of 100 keV or higher. As shown in Figure 6, some of these electrons are transmitted, another part is scattered and others cause different phenomena such as radiation emission, secondary and Auger electrons, X rays, etc. These signals can provide information about the nature of the sample (morphology, composition, crystal structure and electronic structure, etc.). The TEM device uses transmission/scattering of electrons to create images, the diffraction of electrons to obtain information about crystal structure and the characteristic X-ray emission to determine the elemental composition of the sample.

As shown in Figure 6, the electrons passing through the sample may scatter due to interaction with the sample (elastic or inelastic) or may not experience any trajectory change. Elastically scattered electrons can be used to record diffraction images. Unscattered electrons project direct images of the dispersed material. Inelastically scattered electrons are responsible for the background noise in electron microscopy.

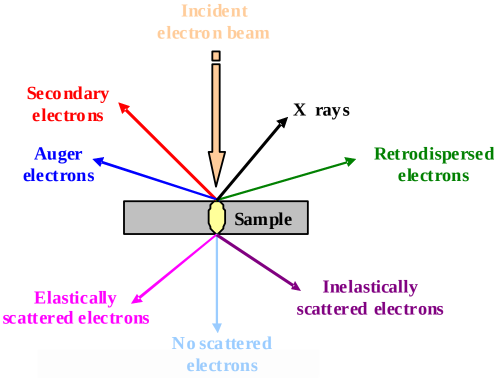

Figure 6. Scheme of the electron beam interaction with the sample.

The diffraction pattern, can be obtained from the analysis of the spatial distribution of elastically scattered electrons. Depending on the crystallinity of the material, different types of diffraction patterns can be observed: i) an amorphous or very small crystal size appears as a series of faint rings, ii) if the sample consists of several crystals with different orientations, the diagram presents the appearance of concentric rings and, iii) in the case of a single crystal, plot consists of regularly distributed points. Based on the measurement of distances, or between points or between the rings of the diagram, information about the interatomic distances of each material can be obtained.

The energy of the X-rays generated when the sample interacts with electrons depends on the type of element. Electrons are able to eject electrons from the inner atomic orbitals, causing ionization. An electron from an higher energy orbital can subsequently fill the lower energy orbital hole. This step results in the emission of energy with a magnitude equal to the difference between the energies of the two orbitals which is unique for each element. When representing the intensity of electromagnetic radiation versus the energy, an X-ray spectrum consisting of a series of discrete peaks is obtained. Based on the characteristic peaks of the elements present, the atomic ratio and, therefore the composition of the sample can be determined.

The transmission electron microscope that was used in this study is a JEOL, JEM-2010 model (Figure 7). The microscope can work in accelerating voltage mode at 100, 120, 160 or 200 kV. A resolution of 0.14 nm between lines and 0.25 nm between points can be obtained. In general, the results obtained with this technique allow observing the catalysts at nanometer scale and enable analyzing the crystal size and morphology of the samples. The samples composition was measured by EDX, using an Oxford Instruments probe (model INCA Energy TEM100).

Figure 7. JEOL transmission electron microscope, JEM-2010 model.

2.3.7. Scanning Electron Microscopy (SEM)

Scanning Electron Microscopy provides morphological and topographical surface information of solids. The images obtained in the scanning electron microscope are produced by secondary electrons or backscattered electrons emitted as a result of the interaction between an incident beam of 5 to 30 KeV and the sample.

The image is obtained by scanning a beam of electrons across the surface of the sample in two directions. The brightness of each point on the screen is proportional to the signal emitted by the sample at that point. The secondary electron signal is emitted from a thin layer of the surface ranging from 50 to 100 Å. Low-energy electrons, with less than 50 eV, can be deflected from their emerging trajectory giving information from areas hidden to the detector. Thus, the signal can provide information about the surface roughness of the sample.

The backscattered electron signal depends strongly on the atomic number of the material irradiated. This means that different areas of a sample with different composition appear with different intensity even if there is no difference in topography among them. The X-rays generated from the

Figure 8. Scanning Electron Microscope Hitachi S3000N.

scattering of the electron beam allow identification the elements present in the sample and their concentration. A Hitachi S3000N Scanning Electron Microscope was used in this study. The microscope was equipped with an Bruker XFlash 3001 X-ray detector for microanalysis (EDS) and chemical mapping (Figure 8).

2.3.8. Diffuse Reflectance Infrared Fourier Transform Spectroscopy (DRIFTS) coupled to Mass spectrometer (MS)

The infrared region of the electromagnetic spectrum consists of radiation with wavenumbers ranging between 12800 and 10 cm^{-1}. For analytical applications, the mid-infrared region (MIR), with wavenumbers between 4000 to 200 cm^{-1} (wavelengths between 2.5 and 50 μm) is usually employed.

The working principle of infrared spectroscopy is the excitation of vibrational and rotational modes of the bonds when irradiated with a beam of infrared light. Each molecule, according to the bond characteristics, will absorb radiation from one or several specific wavelengths, allowing its identification.

There are different analytical techniques based on infrared spectroscopy. Diffuse reflectance spectroscopy is most convenient for working with finely divided solid, as is the case of the samples used in this work. When a powder is irradiated, the radiation penetrates through the surface layer of particles, exciting the vibration modes of the different species present. Infrared light is absorbed and reflected back in all directions. The reflected radiation is guided through a

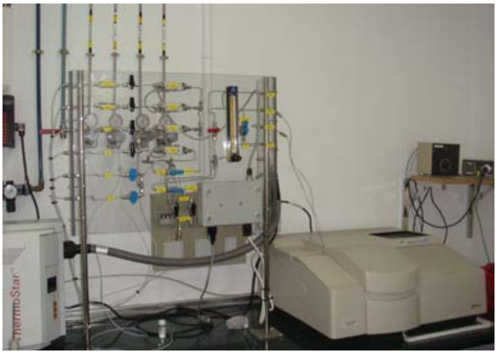

Figure 9. Diffuse reflectance infrared spectrometer.

set of mirrors and measured at the detector, producing a reflectance spectrum.

In this study, *in-situ* DRIFTS experiments were performed on a Mattson FTIR spectrophotometer, model MI60 Infinite (Figure 9), equipped with diffuse reflectance accessory (SpectraTech COLLECTOR model) and a controlled environment chamber (Spectra Tech, model 0030-100). The environment chamber allows controlling temperature and gas flow over the sample and was equipped with $CaCl_2$ windows. The gas composition was monitored during the experiments with a mass spectrometer (OmniStar, Pfeiffer Vacuum).

The N_2O decomposition on the catalysts prepared in this study has been studied by *in situ* DRIFTS-MS experiments. Before the DRIFTS experiments under N_2O-containing gas mixtures, the catalysts were treated *in situ* at 450 ºC under helium flow to remove adsorbed species. Afterwards, the temperature was lowered to 30 ºC and a gas mixture of 1000 ppm N_2O/He, 1000 ppm N_2O/ 5 % O_2/He, 1000 ppm N_2O/2.6% H_2O or 1000 ppm N_2O/1000 ppm NO/ 5% O_2 was introduced. The temperature was raised in steps of 25 ºC, and once the steady state conditions were attained, the spectrum was recorded with a resolution of 2 cm^{-1}. Background spectra were recorded for each sample at room temperature under He flow, and therefore, carbonate bands and some other catalyst features were substrated and do not appear in the spectra recorded under reaction conditions.

2.4. Catalytic activity tests

In this research, catalytic experiments were carried out both at the laboratory and pilot plant scales. At laboratory scale, two types of experiments were performed: N_2O decomposition and pulse experiments using isotopic gases. The experiments carried out at pilot plant scale were carried out in a nitric acid plant.

2.4.1. N_2O decomposition tests at laboratory scale

Figure 10 shows a scheme of the set-up used to carry out the catalytic experiments at laboratory scale.

The experimental set-up is composed of:

- A gas control system, which allows preparing the reaction mixture required from three gas inlets, independently regulated by mass flow controllers (range 0-500 ml / min STP).
- A four-way manual valve, which allows selecting between gases for pretreatment of the sample (helium or hydrogen), and the reactive gas mixture.
- A U-shaped fix-bedquartz reactor, located in a vertical furnace. The temperature of both the sample in the reactor and the furnace are measured by two thermocouples connected to a temperature controller.
- A HP6890 gas chromatograph, equipped with a thermal conductivity detector and two columns (Porapak Q for N_2O and CO_2, and Molecular Sieve 13X for N_2, O_2 and CO) (Figure 11).
- A Chemiluminiscence NO–NO_2 analyzer (SIGNAL 400VM) for NO and NO_2 monitoring (Figure 11).

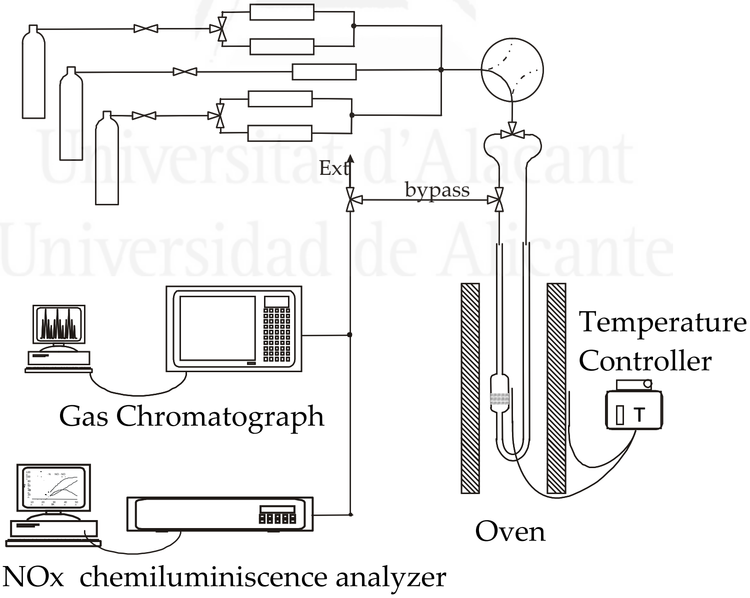

Figure 10. Scheme of the experimental device used to carry out the catalytic experiments.

Figure 11. Gas análisis system: Gas chromatograph + NOx chemiluminiscence analyzer.

In chapter III and IV, N_2O decomposition experiments were carried out at atmospheric pressure in a cylindrical reactor of 10 mm internal inner diameter, using 100 mg of catalyst diluted in 700 mg of SiC to improve the heat transfer inside the catalytic bed and get a more uniform gas flow. A total gas flow of 100 ml/min (GHSV = 10000 h^{-1}) composed of N_2O in He at different concentrations (100, 300, 650, 1000 and 1400 ppm) was used. For experiments, in oxidizing and reducing gas mixtures composed of $O_2/N_2O/He$ and $CO/N_2O/He$, respectively, were employed. The concentration of these gasses is: 5% O_2, 1000 ppm CO and 1000 ppm of N_2O in all cases. Isothermal reactions were carried out at temperatures between 200 ºC and 400 ºC. To perform the experiments, the temperature was kept at 200 ºC until steady state conditions were achieved. After this, the temperature was increased by 25 ºC steps and maintained until steady state was reached at each temperature. In most cases 15-20 minutes were required.

In chapter V, N_2O decomposition tests were also performed in the fixed-bed reactor in 25 ºC steps between 200 and 500 ºC until the steady-state at each temperature was reached. A gas mixture with one or more of the following gases was used: 1000 ppm N_2O; 1000 ppm NO; 1, 2.2 or 5% O_2; 2.4 % H_2O; carrier gas He. The individual gases were mixed by using a set of mass flow controllers to fix the desired composition, except for H_2O, which was fed to the main stream by flowing the carrier gas through a water-containing gas saturator at 22 ºC. Due to the fact that experiments with different GHSV have been performed, the particular conditions (GHSV, mass of catalyst and total gas flow) of each set of experiments is indicated in the figure captions.

From some of the data obtained during the catalytic experiments, the following parameters will be considered in the discussion of the results:

- Equation 1 allows obtaining the percentage of conversion of N_2O.

$$N_2O\ \text{conversion}\ (\%) = \frac{P^i_{N_2O} - P^f_{N_2O}}{P^i_{N_2O}} \times 100 \qquad \text{Equation 1}$$

where $P^i_{N_2O}$ y $P^f_{N_2O}$ are the partial pressures of N_2O at the inlet and outlet of the reactor, respectively.

- The reaction order was calculated using the empirical kinetic model shown in Equation 2.

$$N_2O \longrightarrow N_2 + \tfrac{1}{2} O_2$$

$$v = \frac{-dN_2O}{dt} = k(T) \cdot P^n_{N_2O} \qquad \text{Equation 2}$$

where,
v is the N_2O decomposition rate
k (T) is the kinetic constant, which is a function of temperature and
n is the reaction order with respect to the N_2O partial pressure.

This equation has been integrated with the following boundary conditions:

$$\text{Reactor inlet}: t = 0\ \text{s y}\ P_{N_2O} = P^i_{N_2O}$$
$$\text{Reactor outlet}: t = \tau\ \text{s y}\ P_{N_2O} = P^f_{N_2O}$$

where τ is the residence time of gases in the catalytic bed, which has been calculated as bed volume/flow of gas.

Integration of equation 2 gives equation 3, which relates the partial pressure of N_2O at the output of the reactor with the inlet partial pressure, residence time and kinetic parameters "n" and "k ". The value of these kinetic parameters are estimated by a least squares error function (Equation 4), *i.e.* minimizing the sum of the squared difference between the partial pressures experimentally measured and those predicted by the model calculated by equation 3.

$$P^{f}_{N_2O} = \left[\left(P^{i}_{N_2O}\right)^{1-n} - (1-n)\cdot k\cdot \tau\right]^{\frac{1}{1-n}}$$

Equation 3

$$\text{Error} = \sum \frac{\left(P^{f,exp}_{N_2O} - P^{f,calc}_{N_2O}\right)^2}{\left(P^{f,exp}_{N_2O} + P^{f,tcalc}_{N_2O}\right)^2}$$

Equation 4

Once k(T) values were calculated, the activation energy (Ea) was obtained from the Arrhenius equation (equation 5)

$$k(T) = A\cdot e^{\frac{-Ea}{RT}}$$

Equation 5

where,
k (T): kinetic constant (temperature dependent)
A: preexponential factor
Ea: activation energy in KJ mol^{-1}
R: universal gas constant (8.31 J mol^{-1} k^{-1})
T: absolute temperature in K

The activation energy value can be calculate from the slope of the straight line of the plot ln(k) vs $\frac{1}{RT}$.

$$\ln(k) = \ln(A) - Ea\cdot\left(\frac{1}{RT}\right)$$

Equation 6

In order to apply this kinetic model, experiments with several inlet N_2O partial pressures have been done and this calculation method has been used in chapter IV. In a more simple approach, it can be assumed than N_2O conversion is proportional to N_2O decomposition rate. This is only true if N_2O conversion is very low, that is, if can be assumed that P_{N_2O} is almost constant along the catalytic bed.

$$N_2O\ \text{conversion}\alpha V = k(t)\cdot P^{n}_{N_2O}$$

Equation 7

Substituting equation 5 and taking the logarithms yields:

$$\ln(N_2O\ \text{conversion})\ \alpha A - \frac{\Delta E}{RT} + n \cdot \ln\left(P_{N_2O}\right)$$

ΔE is calculated from the slope of the plot ln(N_2O conversion) vs $-\frac{1}{RT}$.

This simplified method do not requires previous calculation of k(T) valves to determine ΔE, and therefore, can be applied to experimental results obtained with only one N_2O partial pressure. This approach has been followed in chapter III to determine ΔE.

2.4.2. Experiments with isotopic gases

To obtain information about the reaction mechanism, experiments were performed in transient conditions using the pulse method. The tests consist of the injection of $^{18}O_2$ or $^{15}N_2{}^{18}O$ pulses of known volume and pressure in an inert gas stream, flowing through out the catalytic bed.

Figure 12. Quartz microreactor connected to a mass spectrometer for pulse experiments with isotopic gasses.

The experimental set-up used for pulse experiments includes a control panel that feds the reaction gases to a tubular quartz reactor. The reactor is located inside a horizontal furnace with a temperature controller and two thermocouples (sample and oven). This reactor is connected to a Balzers Omnistar mass spectrometer (model GSD300) as analytical system.

The set-up is designed to minimize the dead volume. This was achieved by using 1/16 inch tube, as well as minimizing the distances between different parts of the system. In addition, two pressure controllers avoid change of pressure in the gas stream when pulses of gas are fed to the main carrier stream. The control panel consists of six mass flow controllers and a six-way valve that allows pulsing different gases in a carrier stream of He. Two positions of the valve (Figure 13) are joined by a sample loop (100 µl). The valve has two positions:

- Position A corresponds to the filling of the sample loop, and in this position, the output of the calibrated volume is kept closed with a shutoff valve to prevent losses of gas, while on routes 4 and 5 fed He to the reactor.

- In position B the pulsed gas is injected in the helium stream, and travels to the reactor and to the mass spectrometer.

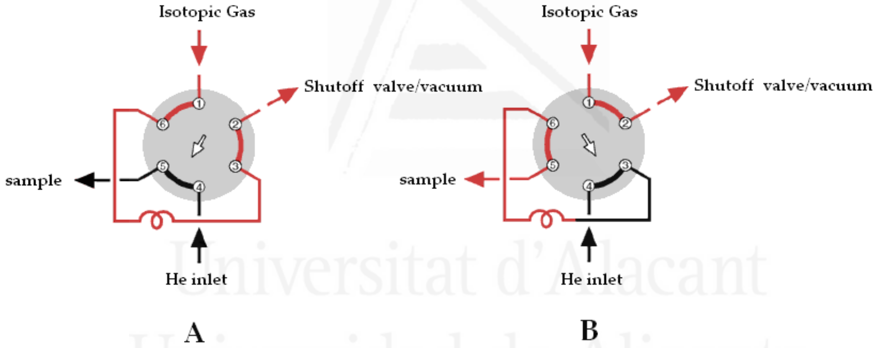

Figure 13. Six way valve. In position A, valves 2-3, 4-5 and 6-1 are connected allow the filling of the sample loop. In position B, the connection of valves changes, so that they are connected 1-2, 3-4 and 5-6, and, in this position, the pulsed gas is injected into the He carrier.

In order to recover the steady state in inert gas after each pulse, the valve is changed back to position A, in which the calibrated volume is refilled with the isotopic gas. Prior to filling, the carrier gas is evacuated from the sample loop with a vacuum pump. This ensures that the pulse introduced is pure and does not contain traces of carrier gas. This mode of operation allows analyzing quantitatively the results, since the amount of gas pulsed is known.

Isotopic gases were used to study the N_2O decomposition mechanism: $^{18}O_2$ (Isotec, 99%) and $^{15}N_2{}^{18}O$ (Isotec, min 98% ^{15}N, min 95% ^{18}O.) The experiments were carried out in a tubular reactor with an internal diameter of 5 mm, using 50 mg of catalyst. The carrier helium flow rate was 10 ml/min, and the gas volume pulsed was 100 μl at a pressure of 5 psi (~ 0.34 atm). Pulses were injected at different temperatures (50, 200, 250, 300, 350 and 400 ºC), and three equivalent pulses were fed at each temperature.

2.4.3. N_2O decomposition tests at pilot plant scale

Catalytic tests were performed in the nitric acid production plant of the Aklady Azotowe "PULAWY" company (Poland), devoted to the production of nitrogen fertilizer. The experiments were performed in a tubular fixed-bed reactor using 2 grams of catalyst. The gas stream used for the experiments was pumped out directly form the nitric acid plant, after the expansion turbine, and different gas flows between 100 and 800 ml/min were used (Gas hourly space velocity = 3800 to 3000 h^{-1}). N_2O, O_2, NO_x and H_2O were present in the gas stream, and since the composition of the gas mixture changes slightly with time (in the hour range of time), the specific concentration of each gas component in a particular experiment will be indicated as required throughout the chapter. For comparative purposes, a model gas stream with 1825 ppm N_2O/N_2 was also tested. Gas composition (at the inlet and outlet of the reactor) was analyzed with an infrared detector (GASMET).

Two types of experiments were performed: (ii) Temperature Programmed Reaction (TPR), raising the temperature at a rate of 3 º C/min to 450 ºC, and (ii) isothermal reactions at 350 ºC.

References

[1] F. Rodríguez-Reinoso, A. Linares-Solano. In: P.A. Thrower, Editor, Chemistry and physics of carbon vol. 21, Marcel Dekker, New York (1989), pp. 1-146. 1999; (21): 1-146. New York, Marcel Dekker.
[2] F. Rouquerol, J. Rouquerol, K. Sing. Adsorption by Powders & Porous Solids: Principles, Methodology and Applications. 1999. Academic Press.

[3] S. Lowell, J.E. Shields, M.A. Thomas, M. Thommas. Characterization of Porous Solids and Powders: Surface Area, Pore Size and Density. 2004. Kluver Academic Publishers.
[4] W.H. Bragg. X-Ray and Crystal Structure. 1918. London, Ed. Bell & Sons.
[5] M. Rodríguez-Gallego. La Difracción de Rayos X. 1982. Universidad de Madrid, Alhambra.
[6]http://www.chemistry.ohio-state.edu/~woodward/ch754/powder_diffraction.pdf
[7] A. Bueno-López, I. Such-Basáñez, C. Salinas-Martínez de Lecea, J. Catal. 244 (2006) 102.
[8] D.A. Skoog y J.J. Leary. Análisis Instrumental (1993). McGraw-Hill
[9] F.R. Pérez. Espectroscopía IR y Raman de cristales y minerales (1993). Universidad de Valladolid.
[10]http://www.ua.es/es/investigacion/sti/servicios/analisis_instrumental/rayosx_monocristales/raman.html
[11] D.A. Skoog, F.J. Holler, T.A. Nieman. Principios de Análisis Instrumental. 2001; 5ª Edición. Madrid, Mc Graw Hill.
[12] L. Reimer Transmision Electron Microscopy. 1989; 2nd edition. Berlin, Springer-Verlag.
[13] J.M. Albella, A.M. Cintas, T. Miranda, J.M. Serratosa. Introducción a la Ciencia de los Materiales. 1993. Madrid, Textos Universitarios, CSIC.

CHAPTER III

Catalytic decomposition of N_2O over alumina and ceria supported Rh, Pd and Pt

Rh, Pd and Pt catalysts were prepared, characterized and tested for N_2O decomposition. The catalyst activity followed the trend Rh > Pd > Pt, and the support significantly affects the activity. Rh/CeO_2(Pr) was the most active catalyst among those prepared and tested. A relationship between the noble metal/ceria catalyst activity and reducibility by H_2 was found. It is proposed that the rate-limiting step of the N_2O decomposition mechanism over noble metal/ceria catalysts is the reduction of the catalysts active sites.

3.1. Introduction

N_2O is the major source of NOx in the stratosphere and contributes to the greenhouse effect and the resulting global warming. In the last decade, the relevance of N_2O abatement has been reflected in the literature [1-5]. The main anthropogenic sources of N_2O are nitric and adipic acid production plants, fossil fuels, biomass combustion and land cultivation [1]. In addition, certain catalytic converters used for gas pollution control in vehicles also contribute to N_2O emission. The Three Way Catalyst (TWC), used in gasoline-powered engines to eliminate CO, hydrocarbons (HC) and NOx produce N_2O as by-product, and the undesired formation of N_2O has been related with catalyst aging. The TWC combines noble metals, mainly Pt, Pd and/or Rh, with CeO_2-based materials [6, 7]. The main reactions taking place are:

$$CO + 1/2\ O_2 \rightarrow CO_2 \quad (1)$$
$$C_xH_y + (x + y/4)\ O_2 \rightarrow xCO_2 + y/2\ H_2O \quad (2)$$
$$NO + CO \rightarrow CO_2 + 1/2\ N_2 \quad (3)$$
$$(2x + y/2)\ NO + C_xH_y \rightarrow x\ CO_2 + y/2\ H_2O + (x + y/4)\ N_2 \quad (4)$$

Reactions (1) and (2) are catalyzed by Pt and Pd, whereas Rh is mainly involved in NOx reduction (reactions (3) and (4)). The reduction of NO with CO can also yield N_2O instead of N_2:

$$2NO + CO \rightarrow N_2O + CO_2 \quad (5)$$

Cant et al. [8] studied the formation of N_2O in model Rh, Pd and Pt catalysts under simulated gasoline exhaust conditions, in a mixture of CO, NO, C_3H_6, C_3H_8, H_2 and O_2. Rh yielded the highest amount of N_2O, with maximum production between 250 ºC and 400 ºC. Pt generated N_2O in a narrow range of temperatures around 400 ºC, and Pd produced N_2O in two temperature ranges, below 200 ºC and above 300 ºC.

Pt catalysts for the Selective Catalytic Reduction (SCR) of NOx with hydrocarbons, currently under development for diesel vehicles [9], also result in N_2O formation. The pollutants emitted by diesel engines are soot, NOx, CO and HC [10]. The concentration of CO and HC in diesel exhausts is significantly lower than those in gasoline engine exhausts, NOx and soot being the main pollutants. Diesel engines operate under O_2 rich conditions, resulting in high levels of O_2 in the exhaust (10-20%). This high concentration of O_2 hinders NOx removal, since NOx reduction can not be performed with the reducing species present in the exhaust (HC and CO). Therefore, it is necessary to feed an additional reductant such as NH_3, urea or HC [11]. A number of catalysts have been proposed for SCR with hydrocarbons, including Pt group metals. Burch et al. [12] reviewed the behaviour of Pt, Pd, Rh, Ir and Ru in SCR of NOx with HC, with particular reference to the formation of N_2O as by-product with some of these noble metals.

The purpose of this work is to analyse the decomposition of N_2O on Rh, Pd and Pt catalysts, devoting particular attention to the effect of the support on the activity of the noble metals for this reaction. The supports studied are γ-Al_2O_3 and different cerium oxides including bare CeO_2 and La- or Pr-doped CeO_2.

3.2. Experimental

3.2.1. Catalyst preparation

The catalysts used in this chapter (Rh/CeO_2, Rh/CeO_2(Pr), Rh/CeO_2(La), Pd/CeO_2, Pd/CeO_2(Pr), Pd/CeO_2(La), Pt/CeO_2, Pt/CeO_2(Pr), Pt/CeO_2(La), Rh/γ-Al_2O_3, Pd/γ-Al_2O_3 y Pt/γ-Al_2O_3) were obtained using the preparation process previously described in chapter II (section 2.2. Materials).

3.2.2. Characterization of supports and catalysts

The BET surface area of the supports was determined by N_2 physisorption and crystalline properties were studied by X-ray diffraction and Raman spectroscopy. In addition, the reducibility of the supports and catalysts were analysed by temperature programmed reduction with H_2 (H_2-TPR). Finally, the particles size of the noble metal particles was determined from TEM microscopy.

These experimental techniques and the experimental conditions used were previously described in detail (chapter II, section 2.3. Characterization techniques).

3.2.3. N_2O decomposition tests

Catalytic N_2O decomposition tests were performed at laboratory scale. First, the behaviour of all catalysts was analyzed by using a gas stream composed by N_2O in He. Based on the results of these experiments, the Rh/CeO_2(Pr), Pd/CeO_2(Pr) and Pt/CeO_2(Pr) catalysts were selected for additional tests carried out in presence of oxidising (O_2) and reducing (CO)gases. Details of these experiments were also described in chapter II.

3.3. Results and discussion

3.3.1. Characterization of the supports by Raman spectroscopy, XRD and N_2 physisorption.

The structure of the cerium oxide-based supports was studied by Raman spectroscopy (Figure 1) and XRD (Figure 2). Both techniques provide complementary information from the sample.

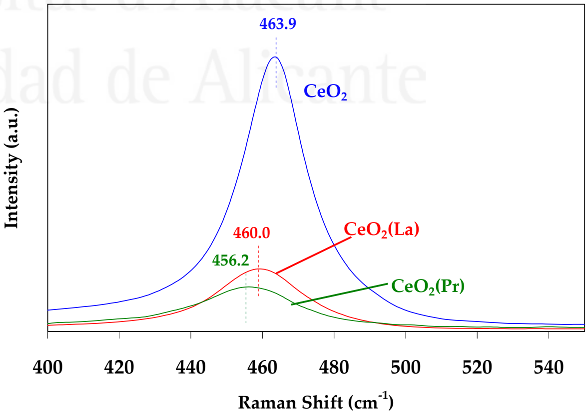

Figure 1. Raman spectra of the cerium oxide supports.

Ceria-based materials have a fluorite structure, based on a face-centered cubic cell. This structure shows a characteristic Raman band at ca. 465 cm^{-1}, assigned to the F_{2g} mode [13-15]. This band is identified in all the Raman spectra included in Figure 1. Evidence of the presence of La_2O_3 or other La or Pr species were not observed in the Raman spectra, suggesting that La and Pr cations do not form segregated phases [17]. The presence of dopants within ceria deforms the lattice and reduces the intensity of the F_{2g} band [18], as observed in Figure 1 for samples $CeO_2(La)$ and $CeO_2(Pr)$ with regard to pure CeO_2. The shift in the position of the F_{2g} band in doped samples with regard to pure CeO_2 further suggests the incorporation of dopants in the ceria lattice [19-21]. The La^{3+} cation (1.16 Å) is larger than the Ce^{4+} cation (0.97 Å) and therefore, the shift of the F_{2g} band towards lower frequencies taking place in the La-doped sample could be consequence of the expansion of the lattice. By contrast, cerium Ce^{4+} and Ce^{3+} cations have similar sizes (0.97 and 1.14 Å, respectively) than the counterpart praseodymium cations Pr^{4+} and Pr^{3+} (0.96 and 1.13 Å, respectively). In this case, the shift of the F_{2g} band due to Pr doping is attributed to alterations in the length and/or frequency of vibration of the metal-oxygen bonds, rather than to changes in the size of the unit cell.

Figure 2 shows the XRD patterns of the different supports. The alumina support shows characteristic peaks of γ-Al_2O_3, and the low intensity and broad width of the peaks reveals the low degree of crystallinity of this material. The diffractograms of pure and doped ceria samples present the reflections characteristic of solids with fluorite structure, corresponding to the (111), (200), (220), (311) (222) and (400) planes [20]. In agreement with the Raman spectroscopy results, XRD neither shows peaks of La_2O_3 or any other species of La or Pr [17].

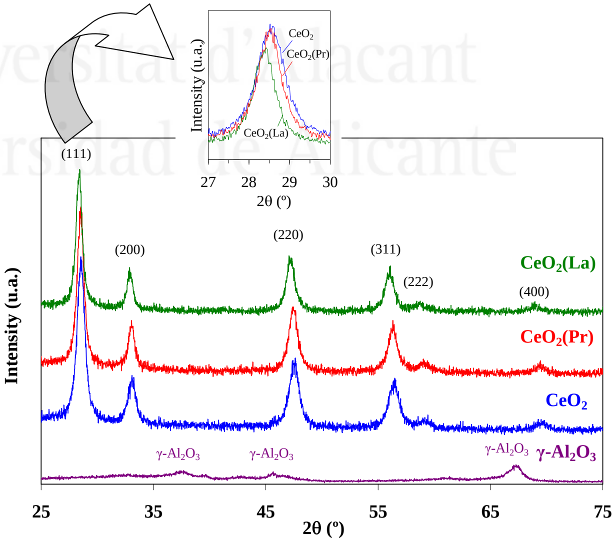

Figure 2. XRD patterns of the supports.

The detailed analysis of the XRD peak positions provides additional information about the structure of the ceria supports. As shown in the inset of Figure 2, the (111) peak shifts toward lower angles when ceria is doped with La^{3+}, because of the expansion of the unit cell [19-21]. In the case of Pr doping, the position of the (111) peak does not change significantly since the size of the Ce and Pr cations is almost equal. The lattice parameters estimated for the pure and doped ceria samples, included in Table 1, support these conclusions. The lattice parameters for Pr doped ceria and bare ceria are quite similar (0.542 and 0.541 nm, respectively), confirming that the size of the unit cell is almost identical. By contrast, La doping leads to the expansion of the unit cell (0.544 nm for CeO_2(La)). The conclusions obtained by XRD about the effect of La and Pr doping in the ceria structure are consistent with those of Raman spectroscopy.

Table 1. Support characterization data obtained from XRD and N_2 physisorption.

Support	Crystallite size by Scherrer (nm)	Crystallite size by W-H (nm)	Lattice constant (nm)	BET (m^2/g)
γ-Al_2O_3	--	--	--	78
CeO_2	11	13	0.541	76
CeO_2(La)	14	20	0.544	49
CeO_2(Pr)	13	17	0.542	44

Table 1 also includes the average crystallite sizes of the ceria supports as obtained from the X-ray diffractograms with the Scherrer and Williamson-Hall (W-H) equations. The crystallite size could not be estimated for the alumina support due to the low crystallinity of the material. The BET surface area of the supports, as determined from N_2 adsorption isotherms, are also included in Table 1. The BET surface areas of the γ-Al_2O_3 and CeO_2 supports are similar (78 and 76 m^2/g, respectively), and the introduction of dopants in the structure of CeO_2 reduces the surface area with regard to that of pure CeO_2. The surface area reduction in doped ceria samples is consistent with the increase in the average crystallite size from 13 nm for pure CeO_2, to 17-20 nm for the doped supports, as calcultated by the Williamson Hall´s equation. The promoting effect of La or Pr in ceria sintering only takes place at relatively moderate calcinations temperature (at 600 ºC in this study). It has been observed that, at higher temperatures (800-1000 ºC), La and Pr partially hinder crystal growth [22].

It is useful to compare the crystallite sizes obtained by applying the Scherrer's equation with those obtained with the Williamson Hall's equation, because evidences about the formation of mixed oxides can be deduced. The Scherrer's equation predicts similar crystallite sizes for the three supports of CeO_2 (11-14 nm). This model assumes that the peak broadening is only due to the size of the crystallites, and the crystallite size values obtained are inconsistent with the BET values. The Williamson-Hall's equation, however, takes into account that the creation of crystalline defects also affects the peaks width. Applying this equation yields a larger crystallite sizes for the doped samples regarding pure CeO_2, being consistent with the decrease in BET surface areas for doped samples in comparison with pure CeO_2. The introduction of La or Pr dopants in the ceria lattice results in the creation of crystalline defects. Therefore, the fact that better results are obtained with the Willliamsom-Hall equation in comparison with those obtained with the Scherrer equation further suggests that La and Pr dopants are incorporated into the ceria lattice.

3.3.2. Estimation of the noble metals particle size by TEM

TEM was used to determine the particle size of the noble metals on the catalysts. Selected TEM images are shown in Figure 3 where, in most cases, the noble metal particles can be clearly distinguished from the support. The noble metal particles can be distinguished in the alumina supported samples, because the atomic weights of aluminium and noble metals are very different to each other. However, the colour contrast between noble metal and cerium oxides is poor because all metals on these samples present high molecular weight. For this reason, the noble metal particles are sometimes hardly distinguishable when supported on cerium oxides. From TEM images, the size of the noble metal particles was estimated and Table 2 compiles the average particle size along with the size of the largest and smallest particle identified in each catalyst, which provides information about the degree of heterogeneity of the noble metal particles.

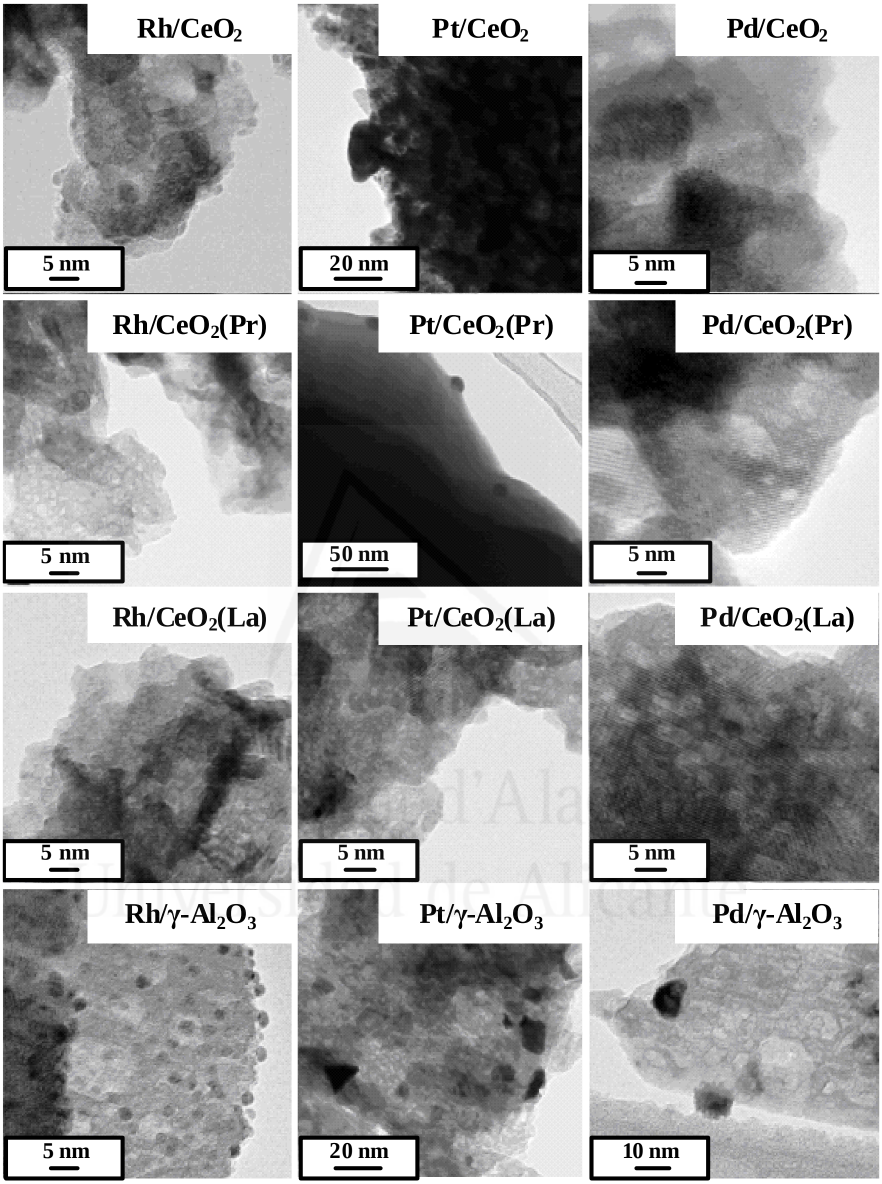

Figure 3. TEM micrographs of the catalysts.

Table 2. TEM-characterization of the noble metals particle size.

Catalyst	Average particle size (nm)	Minimum particle size (nm)	Maximum particle size (nm)
Rh/γ-Al_2O_3	2.3	1.2	3.1
Rh/CeO_2	2.2	1.1	4.9
Rh/CeO_2(La)	1.1	0.6	2.0
Rh/CeO_2(Pr)	1.2	0.6	1.9
Pt/γ-Al_2O_3	4.3	2.4	31.7
Pt/CeO_2	29.2	10.1	41.3
Pt/CeO_2(La)	---	---	---
Pt/CeO_2(Pr)	18.2	11.1	24.2
Pd/γ-Al_2O_3	12.0	1.2	24.2
Pd/CeO_2	<0.5	<0.5	<0.5
Pd/CeO_2(La)	<0.5	<0.5	<0.5
Pd/CeO_2(Pr)	<0.5	<0.5	<0.5

There are no significant differences in the particle sizes of rhodium in the Rh/γ-Al_2O_3 and Rh/CeO_2 catalysts, with an average particle size of 2.2-2.3 nm. Rhodium is slightly better dispersed on La or Pr- doped CeO_2 than on the pure oxide supports, and the average particle sizes are 1.1 and 1.2 nm for Rh/CeO_2(La) and Rh/CeO_2(Pr), respectively. The size of the largest and smallest rhodium particles identified on each catalyst suggests a narrow particle size distribution in all rhodium samples.

Among Pt catalysts, the smallest average particle size of Pt is obtained on γ-Al_2O_3 (4.3 nm). Pt particles on Pt/CeO_2 and Pt/CeO_2(Pr) are larger (average sizes of 29.2 and 18.2 nm, respectively) and show a very heterogeneous particle size distribution, as deduced from the very large difference between the smallest and largest Pt particle identified in both catalysts.

Pt particles hardly were observed in the Pt/CeO_2(La) catalyst, which is attributed to experimental limitations related to the low contrast between noble metal and support on this sample. However, the presence of Pt on this samples was confirmed by EDX analysis, and the dispersion of Pt on CeO_2(La) and CeO_2(Pr) is expected to be similar.

The size of Pd depends significantly on the support used. The Pd particles on Pd/γ-Al_2O_3 presented a very heterogeneous particle size distribution, ranging from 1.2 to 24.2 nm, with an average particle size of 12 nm. However, a very high Pd dispersion was obtained on pure and doped ceria supports. From TEM pictures, it was not possible to estimate the size of the Pd particles on the ceria supports, but it can be expected that it is lower than 0.5 nm. The presence of Pd in all ceria samples was confirmed by EDX analysis

3.3.3. Samples characterization by H_2-TPR

The reducibility of the different samples was analyzed by Temperature Programmed Reduction experiments with H_2 (H_2-TPR) and the profiles obtained are shown in Figure 4. Figure 4a shows the results obtained for the different supports. Ceria reduction profiles are characterized by two main peaks [23]: the first peak, at around 500 °C, is attributed to the reduction of surface Ce^{4+} and the second peak, at temperatures around 850 °C, is assigned to the reduction of bulk Ce^{4+}. This type of profile is found in the pure CeO_2 sample. However, the La- and Pr-containing samples do not show the peaks described, but a broad band from which surface and bulk reduction can not be clearly distinguish to each other. This type of broad profile is indicative of the high oxygen mobility in the lattice of the doped ceria samples [24]. The improve reducibility of the ceria support by La or Pr doping confirms the conclusions of XRD and Raman spectroscopy, where it was observed that the dopants are incorporated into the ceria lattice. However, despite the H_2-TPR profiles of CeO_2(La) and CeO_2(Pr) are characterized by broad bands, several peaks can still be identified. The reduction profile of CeO_2(Pr) shows a small peak with maximum at 475 ºC, which may be attributed to the reduction of Pr^{4+} to Pr^{3+} (note that Pr^{4+} can be reduced more easily than Ce^{4+} [25]). The CeO_2(La) support also presents a small peak with maximum at 490 ºC, but considering that, on one hand, La^{3+} is not reducible under the conditions employed, and on the other hand, the strong CO_2 chemisorption capacity of lanthanum oxide (forming lanthanum carbonate), this peak is tentatively attributed to the desorption of chemisorbed CO_2 species from the catalyst. The maxima at 575 and 800 ºC on the broad H_2-TPR profiles of CeO_2(La) and CeO_2(Pr) could be related with the preferential reduction of surface and bulk Ce^{4+} cations, respectively.

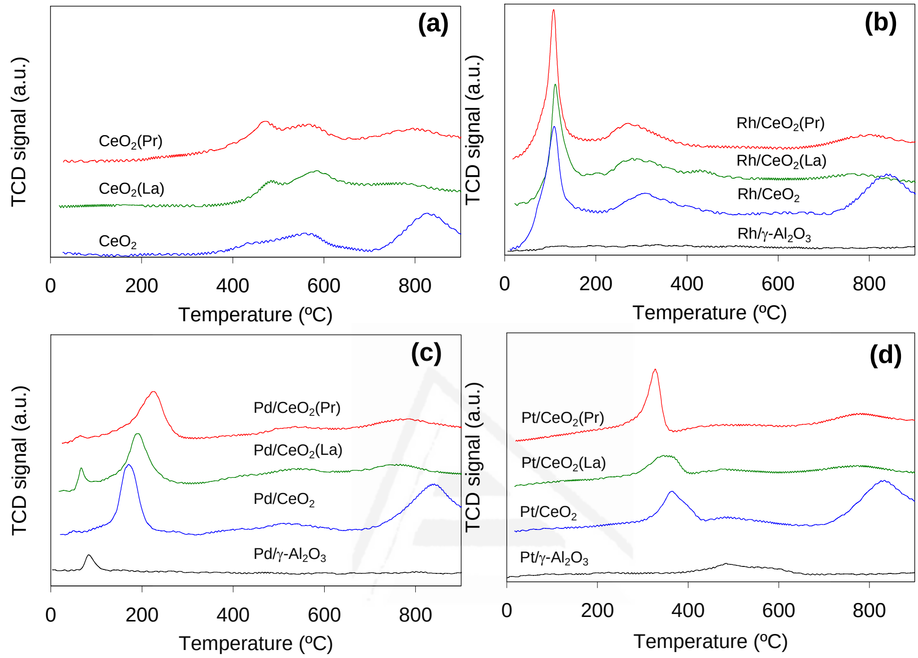

Figure 4. H_2-TPR profiles for (a) supports, (b) Rh catalysts, (c) Pd catalysts, and (d) Pt catalysts.

In the range of temperatures where bulk reduction of the supports takes place (T > 700 ºC, approximately), the H_2-TPR profiles are not significantly modified after loading with noble metals, neither for bare ceria nor for the La- and Pr-doped samples. However, the noble metals significantly modify the H_2-TPR profiles at low and mild temperature. The onset temperature for the TCD signal to increase, for the noble metal-free ceria supports is about 375 ºC, and the noble metal-containing ceria samples show H_2 consumption at much lower temperature. This effect is the largest for Rh (Figure 4b), for which two low-temperature peaks centred at about 110 ºC and 275-300 ºC are observed. The lowest-temperature peak is attributed to noble metal-catalyzed surface reduction of the ceria supports [26], which is confirmed by quantifying the amount of H_2 consumed in this peak. This amount is much higher than that necessary to reduce all the noble metal on the catalysts and, therefore, the reduction of the support can be inferred. For example, the amount of H_2 consumed in the lowest temperature peak of the Rh/CeO_2 sample is 6.5 times the amount needed to reduce the rhodium present on this catalyst. This confirms that the ceria support is reduced at this temperature. In this sense, some authors [27, 28] have observed that some noble metals can be reduced with H_2 at room temperature or even below the ambient temperature. This would explain the absence of noble metal reduction peaks in some of the catalysts with γ-Al_2O_3 support, because the sample, before H_2-TPR experiments, were submitted to a H_2/Ar flow at room temperature during around 30 minutes for the stabilization of the TCD signal.

For the Rh-containing samples, the reduction peak centred at 275-300 ºC (Figure 4b) is also attributed to the surface reduction of the cerium oxide supports. However, in this case the catalytic effect of the noble metal is lower than in the peak at 110 ºC. This is attributed to ceria reduction without close contact with the noble metal [26]. Some authors have suggested that the decomposition of surface carbonates or carbonates occluded within the CeO_2 structure may also contribute to the TCD signal in this range of temperature (around 275-300 ºC) [29, 30].

The reduction of the surface cerium oxide species occur at temperatures around 180-230°C for the Pd-containing samples (Figure 4c), and at 330-370°C for the Pt samples (Figure 4d). Taking into account the position of the low temperature peaks, the catalytic activity of the noble metals to accelerate the reduction of cerium oxide surface follows the trend Rh > Pd > Pt. As will be further shown below, the reducibility of the support plays an important role in the catalytic decomposition of N_2O.

3.3.4. Catalytic tests

3.3.4.1. Catalytic N_2O decomposition

Figure 5 shows the N_2O decomposition profiles obtained in catalytic tests conducted with 1000 ppm N_2O/He. The results obtained with Rh catalysts and bare supports are shown in Figure 5a, and those with Pd and Pt catalysts are shown in Figures 5b and 5c, respectively. Note that the non-catalytic decomposition of N_2O into N_2 and O_2 occurs to a measureable extent only above 625 ºC [1]. The noble metal-free supports (Figure 5a) have a very low catalytic activity below 500 ºC, and for instance, only 10% N_2O decomposition is reached at this temperature with bare CeO_2. The catalytic activity increases for the noble metal-containing samples in comparison with the bare supports, and Rh (Figure 5a) is the most active noble metal among those tested. Rh catalysts (Figure 5a) are active for N_2O decomposition from 200-250 ºC, depending on the support, and the complete conversion is reached in the range 300-400 ºC. The activity of the Rh catalysts for N_2O decomposition follows the trend:

$$Rh/CeO_2(Pr) > Rh/CeO_2(La) > Rh/CeO_2 > Rh/\gamma\text{-}Al_2O_3$$

Both the pure and doped ceria supports improve the catalytic activity in comparison with that of γ-Al_2O_3-supported Rh. Considering the similar size of the rhodium particles in the catalysts (see sizes on Table 2), differences in activity have to be due to metal-support interactions. The improved catalytic activity of Rh when supported on a cerium oxide carrier could be related with the redox properties of these oxides. The lowest activity of the Rh/γ-Al_2O_3 catalyst, among those with Rh, could be consequence of the non reducibility of alumina under reaction conditions. This hypothesis is supported by the conclusions of a previous study [31], where a linear correlation between the catalytic activity for N_2O decomposition and the reducibility of the support surface was obtained for a set of ceria-supported Rh samples.

The Pd (Figure 5b) and Pt (Figure 5c) catalysts are considerably less effective for N_2O decomposition than those of Rh, and do not reach 100% conversion in the studied temperature range. In the case of Pt catalysts (Figure 5c), the effect of the support in the catalytic activity is difficult to interpret. The catalytic activity of Pt/CeO_2 was higher than that of Pt/γ-Al_2O_3, while the catalytic activity of Pt supported on La- and Pr-doped ceria was lower than that of Pt/γ-Al_2O_3. For Pd catalysts, the doped ceria supported catalysts showed similar activity, being higher than that of Pd/γ-Al_2O_3. On the one hand, the TEM-estimated size of the Pd particles supported on pure and doped cerias (<0.5 nm in all cases) are much smaller than that of Pd supported on γ-Al_2O_3 (12 nm average size), which could explain the catalytic activity differences among Pd samples.

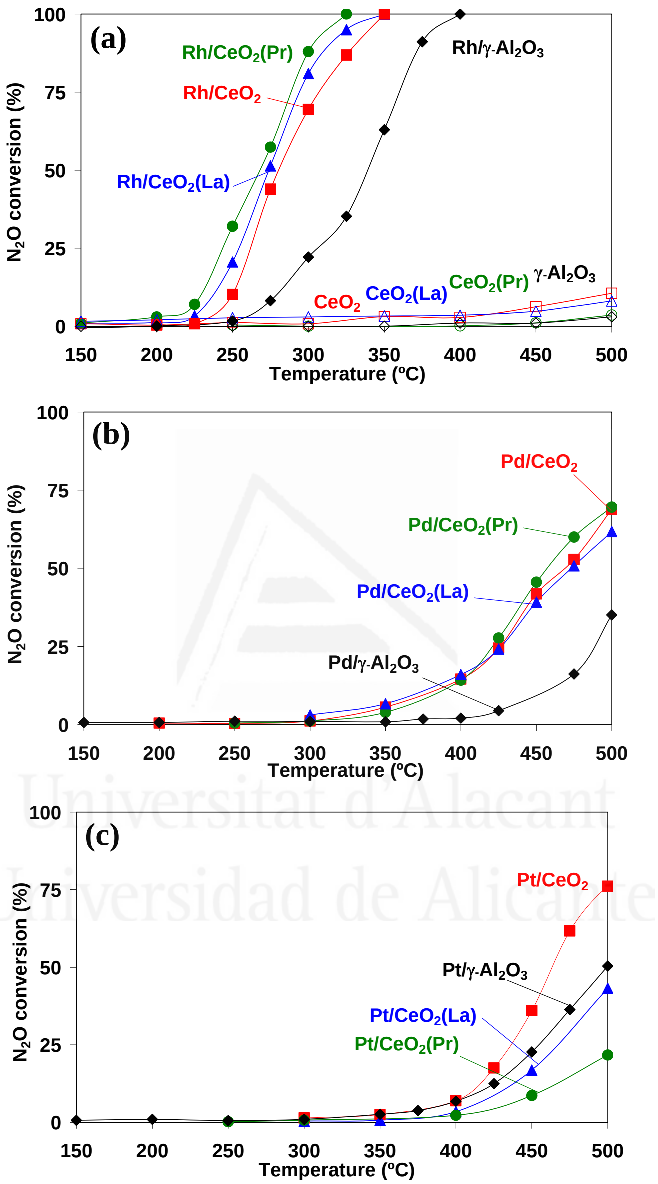

Figure 5. N2O conversion as a function of temperature for (a) supports and Rh catalysts, (b) Pd catalysts and (c) Pt catalysts.

It can not be excluded that the redox properties of the ceria supports could also improve the activity of Pd to some extent. However, all the Pd samples with ceria supports, either bare or doped, behave equal in catalytic tests (Figure 5b) while differences in the redox properties among the bare and doped ceria supports were observed (Figure 4c). This suggests that the effect of the particle size of Pd on ceria supports prevails against the potential improvement due to their redox properties.

In Figure 6, the N_2O decomposition onset temperature, obtained from the Figure 5 curves, is plotted versus the temperature of support surface reduction by H_2, obtained from Figure 4. The N_2O decomposition onset temperature was defined as the temperature required to achieve 10% N_2O decomposition and the temperature of surface reduction by H_2 corresponds to the maximum of the lowest temperature peak in H_2-TPR experiments (Figure 4). This peak was attributed to the noble metal-catalyzed reduction of the support. Figure 6 shows some correlation between the reducibility of the supports and the activity for N_2O decomposition of the noble metal/ceria catalysts. For instance, the most easily reduced catalysts are those with Rh, and they are also the most active catalysts. Both the catalytic activity for N_2O decomposition and for catalytic reduction of the support surface by H_2 follow the trend Rh > Pd > Pt, suggesting that the rate-limiting step for N_2O decomposition is the reduction of the catalytic active sites. However, the effect of the redox properties of the ceria supports on the catalytic activity for N_2O decomposition is evident for Rh catalysts but it is not for Pd and Pt catalysts.

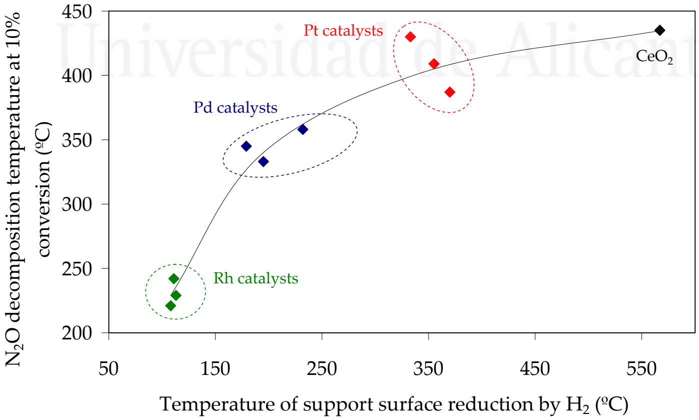

Figure 6. N_2O decomposition onset temperature against temperature for cerium oxide supports surface reduction by H_2.

3.3.4.2. Catalytic removal of N_2O under oxidising ($N_2O + O_2$) and reducing (N_2O + CO) conditions

To further investigate the role of the redox processes in the N_2O decomposition on noble metal/ceria catalysts, catalytic tests were carried out under oxidising ($N_2O + O_2$) and reducing (N_2O + CO) conditions. For these experiments, the noble metal catalysts with CeO_2(Pr) support were selected. Figure 7 shows the N_2O conversion curves for the different experiments performed with these catalysts under 1000 ppm N_2O + 5%O_2/He (N_2O +O_2) and 1000 ppm N_2O +1000 ppm CO/He (N_2O + CO). The experiments conducted with 1000 ppm N_2O/He (N_2O) are included for comparative purposes. The analysis of the reaction products confirms that N_2O is decomposed into N_2 and O_2 in experiments performed in the absence of CO, both with and without O_2 in the feed. In experiments conducted under N_2O + CO, once the steady state is reached, N_2O reduction takes place with consumption of CO and N_2O and formation of N_2 and CO_2 in stoichiometric amounts.

O_2 partially inhibits the catalytic decomposition of N_2O over all catalysts tested, as deduced by comparison of curves in Figure 7 obtained under N_2O and $N_2O + O_2$. This is consistent with the relationship obtained in Figure 6 between the activity of the noble metal/ceria catalysts for N_2O decomposition and the reducibility of the support, since O_2 hinders the reduction and therefore the activity. These results also evidences that the rate-limiting step of the N_2O decomposition mechanism is the reduction of the catalytic active sites, and the partial inhibition of the catalytic activity in the presence of O_2 supports this hypothesis. Kapteijn et al. [1] reported that O_2 inhibits the catalytic activity of most N_2O decomposition catalysts, in a different extent depending on the nature of the catalyst.

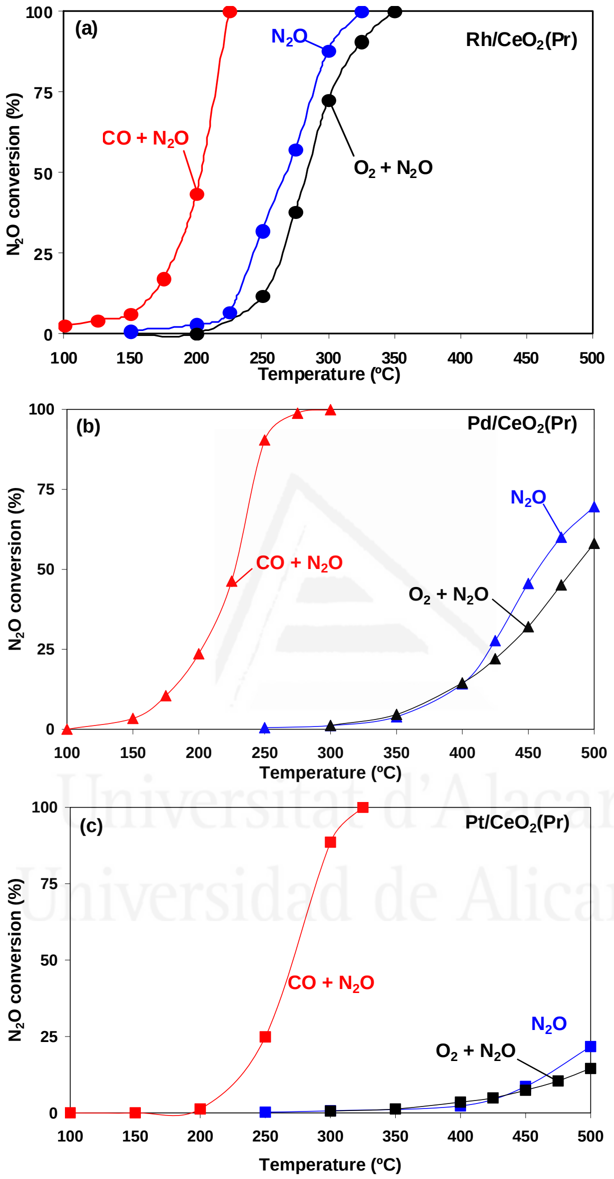

Figure 7. Catalytic conversion of N_2O under 1000 ppmN_2O/He (N_2O), 1000 ppm N_2O + 5%O_2/He (N_2O +O_2), and 1000 ppm N_2O +1000 ppm CO/He (N_2O + CO) with the catalysts (a) Rh/CeO_2(Pr), (b) Pd/CeO_2(Pr) and (c) Pt/CeO_2(Pr).

By contrast, CO enhances the conversion of N_2O on all the noble metal/CeO_2(Pr) catalysts tested, as deduced by comparison of curves obtained under N_2O and N_2O + CO (Figure 7). This improvement is moderate for Rh/CeO_2(Pr) but is very important for Pd and Pt catalysts. As observed in the H_2-TPR experiments (Figure 4), the surface of the Rh/CeO_2(Pr) catalyst is reduced more easily than that of the counterpart Pd and Pt catalysts. CO has a smaller beneficial effect on the catalytic removal of N_2O for the catalysts that are more readily reduced. The catalytic tests performed under N_2O + CO suggest once more that the rate-limiting step of the N_2O decomposition mechanism is the reduction of the active sites of the catalysts, and because CO accelerates the reduction, an activity increase is observed for the less reducible Pd and Pt catalysts.

Arrhenius plots, shown in Figure 8, were obtained for the experiments performed under N_2O atmosphere for the noble metal catalysts with CeO_2(Pr) or γ-Al_2O_3 supports and, additionally, for N_2O decomposition in the presence of O_2 or CO by the noble metal/CeO_2(Pr) catalysts. All the obtained values are lower than those reported for the non-catalytic N-O bond splitting in the N_2O molecule (250-270 kJ/mol) [32-34].

In the absence of CO and O_2, the most significant result is the difference in the activation energies for Rh/γ-Al_2O_3 and Rh/CeO_2(Pr) catalysts, 145 and 91 kJ/mol, respectively. This difference suggests a different reaction mechanism and the participation of the CeO_2(Pr) support in the reaction mechanism.

On the other hand, for CeO_2(Pr) supported catalysts, the addition of O_2 to the gas stream does not change the activation energy, and values in the range 91-100 kJ/mol were obtained. This supports that O_2 neither changes the N_2O decomposition mechanism nor the rate-limiting step of the catalytic N_2O decomposition. It has been previously proposed that O_2 partially inhibits the activity for N_2O decomposition of the noble metal/ceria catalysts because it hinders the reduction of active sites. The similar activation energies found for the catalytic decomposition of N_2O in the presence and absence of O_2 support this hypothesis.

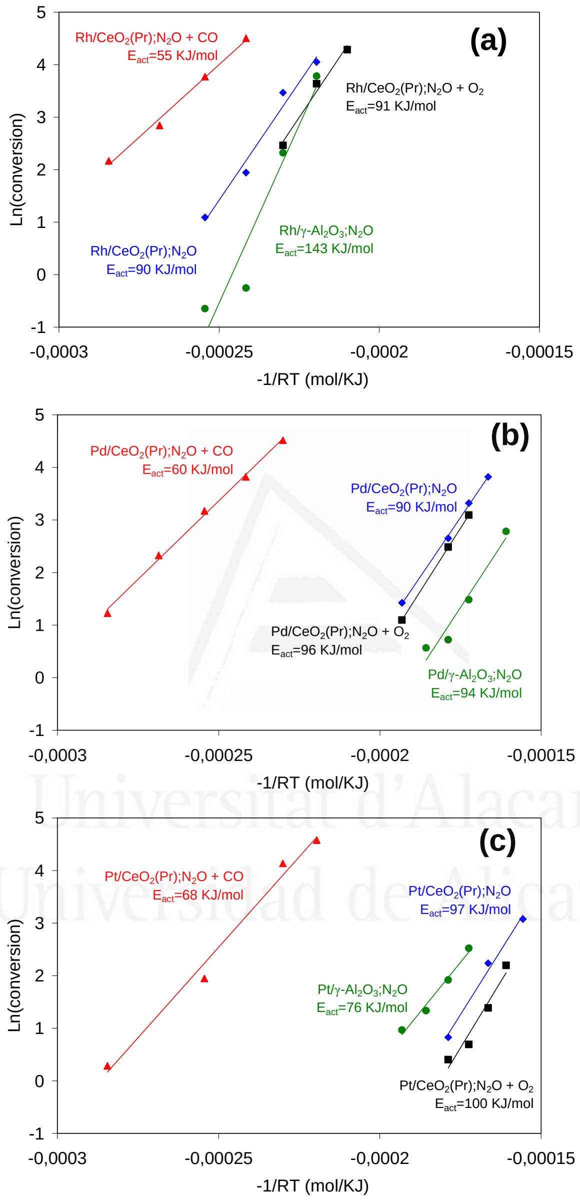

Figure 8. Arrhenius plots for the decomposition/reduction of N_2O in different atmospheres for (a) Rh catalysts, (b) Pd catalysts and (c) Pt catalysts.

In the presence of CO, however, the activation energy for the CeO_2(Pr) supported catalysts decreases from 90-97 kJ/mol to 55-68 kJ/mol. This decrease in the activation energies supports that CO accelerates the rate-limiting step of the mechanism, which seems to be the reduction of the catalysts active sites.

3.4. Discussion on the N_2O decomposition mechanism

Considering both the results obtained in this study and the N_2O decomposition mechanisms described in the literature [1], it is proposed that the decomposition of N_2O over the Rh, Pd and Pt catalysts tested in the current study occurs with the successive reduction and oxidation of noble metal active sites by N_2O (Eley-Rideal mechanism):

$$NM^{*}\text{-}O + N_2O \rightarrow NM^{*} + N_2 + O_2 \qquad \text{Step 1}$$

$$NM^{*} + N_2O \rightarrow NM^{*}\text{-}O + N_2 \qquad \text{Step 2}$$

where "NM*" and "NM*-O" are reduced (not necessarily to the metallic state) and oxidized noble metal active sites, respectively.

Besides these two steps, another O_2 formation pathway, consisting of the recombination of two oxygen atoms located in two oxidized active sites should also be considered (Langmuir-Hinshelwood mechanism):

$$2NM^{*}\text{-}O \leftrightarrow 2NM^{*} + O_2 \qquad \text{Step 3}$$

The participation of the noble metals in the N_2O decomposition mechanism is confirmed by the fact that the noble metal-free supports have very low or null activity under the experimental conditions of the current study.

However, it is reasonable to think that the reaction mechanism is more complex than that described by steps 1 to 3. For example, it can be assumed that steps 1 and 2 are a combination of steps involving dissociative chemisorption of N_2O or molecular chemisorption followed by dissociation of N_2O molecules. Also, the found relationship between the reducibility of the ceria support and catalytic activity (Figure 6), and the differences in activation energy (Figure 8) suggest that, for Rh catalysts, ceria participates in the N_2O decomposition mechanism. This participation could be related to the reoxidation of noble metal active sites with ceria oxygen, following the sequence of reactions steps described by step 4 and 5:

$$NM^* + Ce^*\text{-}O \rightarrow NM^*\text{-}O + Ce^* \qquad \text{Step 4}$$

$$Ce^* + N_2O \rightarrow Ce^*\text{-}O + N_2 \qquad \text{Step 5}$$

In these reactions, "Ce*" represents a reduced active site of the ceria support, most probably associated with an oxygen vacancy link to a "Ce^{3+}" cation (or "Pr^{3+}"in the CeO_2(Pr) support), and "Ce*-O" represents an oxidised active site on the ceria support that is able to transfer oxygen to the noble metal. The transfer of oxygen from ceria to the noble metal (step 4) leads to the local reduction of the support, which must restore the oxygen balance by reoxidation of the vacant sites created with oxygen of a N_2O molecule (step 5). Steps 4 and 5 are valid for catalysts with CeO_2-based supports, but not for catalysts with γ-Al_2O_3 support, since γ-Al_2O_3 cannot be reduced under typical reaction conditions. However, for Pd/CeO_2(Pr) and Pt/CeO_2(Pr) catalysts, their low catalytic activity for N_2O decomposition in comparison to that of the Rh/CeO_2(Pr) catalyst, and the similar activation energy value for both ceria and alumina catalysts, suggest that steps 4 and 5 are not significant steps in the reaction mechanism for Pd and Pt catalysts.

The rate of each step of the described mechanism will depend on the nature of both the noble metal and the support. However, the experimental data suggest that, in all cases, the rate-limiting step is the reduction of the active sites (steps 1 and/or 3) and CO accelerates the slowest step of the mechanism:

$$NM^*\text{-}O + CO \rightarrow NM^* + CO_2 \qquad \text{Step 6}$$

For catalysts with a ceria-based support, the partial reduction of the support by CO may also take place:

$$Ce^*\text{-}O + CO \rightarrow Ce^* + CO_2 \qquad \text{Step 7}$$

The reduction of the ceria support by CO (step 7) will also enhance the N_2O decomposition rate, since the active sites created on the ceria supports upon CO reduction will also be involved in N_2O removal (step 5).

The partial inhibition of the catalytic N_2O decomposition by O_2 is attributed to the competition between N_2O and O_2 for the catalysts active sites (competition between steps 8 and 2). Either the sites located on the noble metal or those on the support (competition between steps 8 and 9 with steps 2 and 5) can be affected by O_2.

$$NM^* + O_2 \rightarrow NM^*\text{-}O_2 \rightarrow 2NM^*\text{-}O \qquad \text{Step 8}$$

$$Ce^* + O_2 \rightarrow Ce^*\text{-} O_2 \rightarrow 2Ce^*\text{-}O \qquad \text{Step 9}$$

In steps 8 and 9 both dissociative and molecular chemisorption of O_2 can occur.

3.5. Conclusions

Rh, Pd and Pt were supported on γ-Al_2O_3, pure CeO_2 and La- or Pr-doped CeO_2, and these catalysts were tested for N_2O decomposition. The following conclusions have been drawn:

- The three noble metals tested (Rh, Pd and Pt) catalyze the decomposition of N_2O, Rh being the most active catalyst.
- The redox properties of the support affect the catalytic activity for Rh catalysts and ceria-based support present higher activity than alumina support.
- The activity for N_2O decomposition of the ceria-based noble metal catalysts is related to the reducibility of the catalysts by H_2, the easier is the reduction the higher is the catalytic activity.
- The rate-limiting step of the N_2O decomposition mechanism over ceria-based noble metal catalyst seems to be the reduction of the catalytic active sites. For Rh catalysts, it is evident that ceria

supports, either bare or doped, are directly involved in the N_2O decomposition process, while ceria participation is not so evident for Pd and Pt catalysts.

References

[1] F. Kapteijn, J. Rodríguez-Mirasol, J.A. Moulijn, Appl. Catal. B 9 (1996) 25.
[2] J. Pérez-Ramírez, F. Kapteijn, K. Schoffel, J.A. Moulijn, Appl. Catal. B 44 (2003) 117.
[3] K. Yuzaki, T. Yarimizu, K. Aoyagi, S. Ito, K. Kunimori, Catal. Today 45 (1998) 129.
[4] G. Centi, S. Perathoner, F. Vazzana, M. Marella, M. Tomaselli, M. Mantegazza, Adv. Environ. Res. 4 (2000) 325.
[5] S. Imamura, R. Hamada, Y. Saito, K. Hashimoto, H. Jindai, J. Mol. Catal. A 139 (1999) 55.
[6] H. S. Gandhi, G.W. Graham, R.W. McCabe, J. Catal. 216 (2003) 433.
[7] P. Vidmar, P. Fornasiero, J. Kašpar, G. Gubitosa, M. Graziani, J. Catal. 171 (1997) 160.
[8] N.W. Cant, Dennys E. Angove, D.C. Chambers, Appl. Catal. B 17 (1998) 63.
[9] G. Garrigós-Pastor, S. Parres-Esclapez, A. Bueno-López, M.J. Illán-Gómez, C. Salinas-Martínez de Lecea, Appl. Catal. A 354 (2009) 63.
[10] J.P.A. Neeft, M. Makkee, J.A. Moulijn, Fuel Proces. Technol. 47 (1996) 1.
[11] B.A.A.L. Van Setten, M. Makkee, J.A. Moulijn, Catal. Rev. Sci. Eng. 43 (2001) 489.
[12] R. Burch, P.J. Millington, Catal. Today 26 (1995) 185.
[13] L.N. Ikryannikova, A.A. Aksenov, G.L. Markaryan, G.P. Murav'eva, B.G. Kostyuk, A.N. Kharlanov, E.V. Lunina, Appl. Catal. A 210 (2001) 225.
[14] J. Kašpar, P. Fornasiero, M. Grazini, Catal. Today 50 (1999) 285.
[15] A. Mineshige, T. Taji, Y. Muroi, M. Kobune, S. Fujii, N. Nishi, M. Inaba, Z. Ogumi, Solid State Ion. 135 (2000) 481.
[16] M. Fernández-García, A. Martínez-Arias, A. Iglesias-Juez, C. Belver, A. B. Hungria, J.C. Conesa, J. Soria, J. Catal. 194 (2000) 385.
[17] A. Bueno-López, K. Krishna, M. Makkee, J.A. Moulijn, J. Catal. 230 (2005) 237.
[18] J.R. Mcbride, K.C. Hass, B.D. Poindexter, W.H. Weber, J. Appl. Phys. 76 (1994) 2435.

[19] J. E. Spanier, R.D. Robinson, F. Zheng, S.W. Chan, I.P. Herman, Phys. Rev. B 64 (2001) 2454071.
[20] F. Zhang, S.W. Chan, J.E. Spanier, E. Apak, Q. Jin, R.D. Robinson, I.P. Herman, Appl. Phys. Lett. 80 (2002) 127.
[21] S. Rossignol, C. Descorme, C. Kappenstein, D. Duprez, J. Mater. Chem. 11 (2001) 2587.
[22] K. Krishna, A. Bueno-López, M. Makkee, J.A. Moulijn, Appl. Catal. B 75 (2007) 210.
[23] J.M. García Cortes, J. Pérez Ramírez, M.J. Illán Gómez, F. Kapteijn, J.A. Moulijn, C. Salinas Martínez de Lecea, Appl. Catal. B. 30 (2001) 399.
[24] G.L. Markaryan, L.N. Ikryannikova, G.P. Muravieva, A.O. Turakulova, B.G. Kostyuk, E.V. Lunina, V.V. Lunin, E. Zhilinskaya, A. Aboukais, Colloids Surf. A 151 (1999) 435.
[25] K. Krishna, A. Bueno-López, M. Makkee, J.A. Moulijn, Appl. Catal. B 75 (2007) 189.
[26] J. Silvestre-Albero, F. Rodríguez-Reinoso, A. Sepúlveda-Escribano. J. Catal. 210 (2002) 127.
[27] P. Fornasiero, J. Kaspar, V. Sergo, M. Graziani, J. Catal. 182 (1999) 56.
[28] P. Fornasiero, J. Kaspar, T. Montini, M. Graziani, V. Dal Santo, R. Psaro, S. Recchia, J. Molec. Catal. A 204 (2003) 683.
[29] F.M.Z. Zotin, L. Tournayan, J. Varloud, V. Perrichon, R. Frety, Appl. Catal. A 98 (1993) 99.
[30] P. Fornasiero, R. DiMonte, G.R. Rao, J. Kaspar, S. Meriani, A. Trovarelli, M. Graziani, J. Catal. 151 (1995) 168.
[31] A. Bueno-López, I. Such-Basáñez, C. Salinas-Martínez de Lecea, J. Catal. 244 (2006) 102.
[32] K. Jones, in J.C. Bailar, H.J. Emeleus, R. Nyholm and A.F. Trotman-Dickenson (Editors), Comprehensive Inorganic Chemistry, Pergamon Press, Oxford, 1984, pp. 316.
[33] W.M. Kalback, C.M. Sliepcevich, Ind. Eng. Chem. Fundam., 17 (1978) 165.
[34] B.G. Reuben, J.W. Linnett, Trans. Faraday Soc., 55 (1959) 1543.

CHAPTER IV

Study of the N_2O decomposition mechanism on Rh/CeO_2 and Rh/γ-Al_2O_3 catalysts

The N_2O decomposition mechanism on Rh/CeO_2 and Rh/γ-Al_2O_3 catalysts was studied by isotopic gas pulses and by *in situ* spectroscopies. The higher catalytic activity shown by Rh/CeO_2 is related to the Rh-CeO_2 interaction and to the participation of the CeO_2 support in the N_2O decomposition mechanism. The ceria support interacts strongly with rhodium partially stabilises cationic species of the noble metal during N_2O decomposition. By contrast, rhodium on Rh/γ-Al_2O_3 is reduced to Rh^0 under reaction conditions and N_2O decomposition over this catalyst mainly occurs via the Eley-Rideal mechanism.

4.1. Introduction

In chapter III, the catalytic decomposition of N_2O into N_2 and O_2 using Rh, Pd and Pt supported on γ-Al_2O_3, CeO_2 and CeO_2 doped with La or Pr was studied, and it was concluded that Rh is the most active noble metal for N_2O decomposition among those tested. It was also observed that the support has a significant effect on the noble metal catalytic activity. Rh supported on pure and doped CeO_2 is more active than Rh supported on γ-Al_2O_3. These results suggest that CeO_2 has an active role in the N_2O decomposition mechanism. Therefore, the objective of this chapter is to further study this issue.

Several mechanisms have been proposed to describe the catalytic decomposition of N_2O [1-6]. The study of these mechanisms is based, in most cases, on the analysis of the effect of N_2O partial pressure and temperature on the decomposition rate. The catalytic decomposition reaction has been described as a molecular adsorption of N_2O on catalyst (*) active site, followed by decomposition and N_2 release.

$$* + N_2O \leftrightarrow *\text{-}N_2O$$
$$*\text{-}N_2O \leftrightarrow N_2 + *\text{-}O$$

For instance, transient kinetic studies, performed with MnO_2 catalysts, demonstrated that not all adsorption sites that are suitable for N_2O adsorption are active for N_2O decomposition [7]. On the other hand, depending on the catalyst nature, dissociative chemisorption of N_2O can occur in a single step instead of molecular adsorption followed by surface decomposition:

$$* + N_2O \leftrightarrow N_2 + *\text{-}O$$

The oxygen atoms left on the active sites (*-O) can be desorbed by recombination with O_2 release (Langmuir-Hinshelwood mechanism):

$$2*\text{-}O \leftrightarrow 2* + O_2$$

or by reaction with another N_2O molecule (Eley-Rideal mechanism):

$$*\text{-}O + N_2O \rightarrow * + N_2 + O_2$$

Note that the recombination of oxygen atoms is a reversible process while the regeneration of active sites by N_2O is irreversible [4]. The reversibility of the former reaction explains why O_2 has an inhibitory effect on most N_2O decomposition catalysts: since N_2O and O_2 compete for the active sites of the catalyst [4].

The interaction of O_2 molecules with catalytic surfaces has been thoroughly studied [8-13], and the knowledge about these interactions is useful to explain some aspects of the N_2O decomposition mechanism and to develop catalysts for N_2O decomposition in O_2-rich streams. Isotopic gases are very useful to study the interaction of gas molecules with solid catalysts, and many studies have been carried out with $^{18}O_2$ [14, 15]. From these studies, it has been concluded that there are three main processes involved in the oxygen exchange mechanisms between molecular oxygen and metal oxide surfaces: the dissociative chemisorption of molecular oxygen, the exchange of atoms or adsorbed ions, and the desorption of molecular oxygen. The exchange of oxygen atoms can occur in a single step or in two consecutive steps, and the nature of the solid surface significantly affects these processes.

The interaction of ceria-based oxides with isotopic O_2 has been widely studied [9, 18-20], and the oxygen exchange capacity of this type of oxides is high. In some cases, the interaction of ceria-based materials with other oxygen-containing isotopic gases different to $^{18}O_2$ has been studied. For example, Cunningham et al. [18] studied the exchange of oxygen between $^{15}N^{18}O$ and CeO_2, which takes place from 175 ºC, and evidence of the oxygen exchange between $C^{18}O_2$ and CeO_2 has been also reported [21, 22]. The oxygen exchange mechanism between isotopic CO_2 and a Pt/CeO_2 catalyst occurs in two consecutive steps and the exchange of both $C^{18}O_2$ oxygen atoms prevails with regard to the single exchange. However, as far as we know, the interaction of isotopic N_2O with Rh/ceria catalysts has not been reported.

Thus, the aim of this chapter is to study the Rh-catalyzed N_2O decomposition mechanisms, in order to understand the improved activity of Rh/ceria with regard to Rh/alumina catalysts. In our approach pulse experiments with isotopic $^{15}N_2{}^{18}O$ and $^{18}O_2$ was combined with *in situ* XPS, DRIFTS-MS and Raman spectroscopy experiments. The combination of these techniques provides complementary information about the reaction mechanism. The experiments with isotopic gases provide information about the participation of catalyst oxygen in the N_2O decomposition mechanism, *in situ* DRIFTS-MS allows monitoring the surface nitrogen groups during the reaction while *in situ* XPS and Raman spectroscopy are able to identify changes in the catalyst during N_2O decomposition, such as changes in the oxidation states of the metals involved in the reaction.

4.2. Experimental

4.2.1. Catalyst preparation

The preparation of the catalysts used in this chapter, referred to as Rh/γ-Al_2O_3 and Rh/CeO_2, is described in detail in chapter II, section 2. In addition the bare γ-Al_2O_3 and CeO_2 supports have been also studied.

4.2.2. Characterization of supports and catalysts

The support and catalysts were characterized by Raman spectroscopy, XRD, N_2 physisorption, H_2-TPR and TEM. Detailed information about these characterization techniques was reported in chapter III. It is noted here that both supports present similar BET surface area (76 m²/g CeO_2 and 78 m²/g γ-Al_2O_3) and similar rhodium particles size (average size of rhodium particles 2.2 nm in Rh/CeO_2 and 2.3 nm in Rh/γ-Al_2O_3, as observed by TEM).

4.2.3. Catalytic tests

In this chapter, two types of tests were performed to get information about the N_2O decomposition mechanism.

- *N_2O decomposition tests in a fixed-bed reactor*. Different N_2O/He mixtures with N_2O concentrations of 100, 300, 600, 1000 and 1400 ppm were used. Additionally, experiments with 1000 ppm N_2O/5 % O_2/He were performed. All experiments were carried out with the same sample of each catalyst. In order to ensure that the catalyst activity does not change during the tests, a control test was performed every few catalytic cycles under 1000 ppm N_2O/He.

- *Pulse experiments with isotopic gases ($^{15}N_2{}^{18}O$ and $^{18}O_2$).* $^{18}O_2$ and $^{15}N_2{}^{18}O$ were used in the pulse experiments. Firstly, experiments with Ar, non-isotopic N_2O and O_2 were carried out in order to evaluate the system response. After the non-isotopic gas pulses, pulses with $^{15}N_2{}^{18}O$ and $^{18}O_2$ were performed.

Details related to the development of these experiments were included in chapter II of this thesis.

4.2.4. In situ DRIFTS-MS experiments and XPS characterization after in situ treatments under reaction conditions

In situ DRIFTS-MS experiments were carried out with gas mixtures of 1000 ppm N_2O/He or 1000 ppm N_2O/5 % O_2/He. After steady state conditions were achieved both in the gas composition and catalyst surface, the temperature was raised in steps of 25 ºC. The temperatures studied ranged from 30 ºC to 300 ºC.

The catalysts were also characterized by XPS before and after heat treatments in N_2O conducted for one hour at different temperatures between 250 ºC and 325 ºC.

The experimental details about these techniques are described in chapter II (section 3. Characterization techniques).

4.3. Results and discussion

4.3.1. N_2O decomposition tests

Figure 1 presents the N_2O decomposition rates as a function of temperature obtained with Rh/γ-Al_2O_3 (Figure 1a) and Rh/CeO_2 (Figure 1b) during the first and second run (performed under 1000 ppm N_2O/He) and during the third run (performed under 1000 ppm N_2O/5 % O_2/He). The N_2O decomposition rate on CeO_2 and γ-Al_2O_3, also included in Figure 1, is negligible under the reaction conditions of these experiments. The rates affected by mass transfer effects (dashed lines) are distinguished from those measured under chemical control (continuous lines).

For experiments conducted under equal conditions, the N_2O decomposition rate on Rh/γ-Al_2O_3 (Figure 1a) is lower than that on Rh/CeO_2 (Figure 1b). The N_2O decomposition rates measured with Rh/CeO_2 during the first and second cycle are equal, while the decomposition rates of Rh/γ-Al_2O_3 increases after the first run. This activation process will be studied and discussed in the coming sections. As expected, the N_2O decomposition rates partially decrease in the presence of O_2 (3rd run) due to O_2 chemisorption on the catalyst active sites. This decrease is reversible, that is, the N_2O decomposition rate increases to the original level if O_2 is removed from the gas stream. It has been reported that O_2 partially inhibits the catalytic activity of most N_2O decomposition catalysts [1] and this inhibition affects in a different extent depending on the nature of the catalyst.

The N_2O decomposition rates measured for Rh/γ-Al_2O_3 and Rh/CeO_2 catalysts under chemical control of the reaction rate are higher than some values reported by other authors. For instance, N_2O decomposition rates catalysts (under 1000ppm N_2O + 5% O_2 at 300 ºC) are 0.36 and 0.71 $mol(N_2O)\cdot g^{-1}\cdot h^{-1}$ for Rh/γ-Al_2O_3 and Rh/CeO_2, respectively. In literature, a N_2O decomposition rate of 0.37 $mol(N_2O)\cdot g^{-1}\cdot h^{-1}$ at 400 ºC has been reported [2,3,23] for a 0.5 wt% Rh/CeO_2 catalyst measured under a gas mixture with 950ppm N_2O + 5% O_2. The lower rate obtained with this Rh/CeO_2 catalyst [23] in comparison with the results shown here could be due to the low surface area the catalyst tested (9 m^2/g) with regard to the surface area of samples used in this work (76-78 m^2/g). The present N_2O decomposition rates are also higher than values reported for other Rh/CeO_2 and Rh/Al_2O_3 catalysts [24] (with 22 and 168 m^2/g, respectively, and both with 2 wt. % Rh). This comparison suggests that the catalytic activity for N_2O decomposition of the Rh catalysts not only depends on the nature of the active phases but also on the particular physico-chemical features of each catalyst.

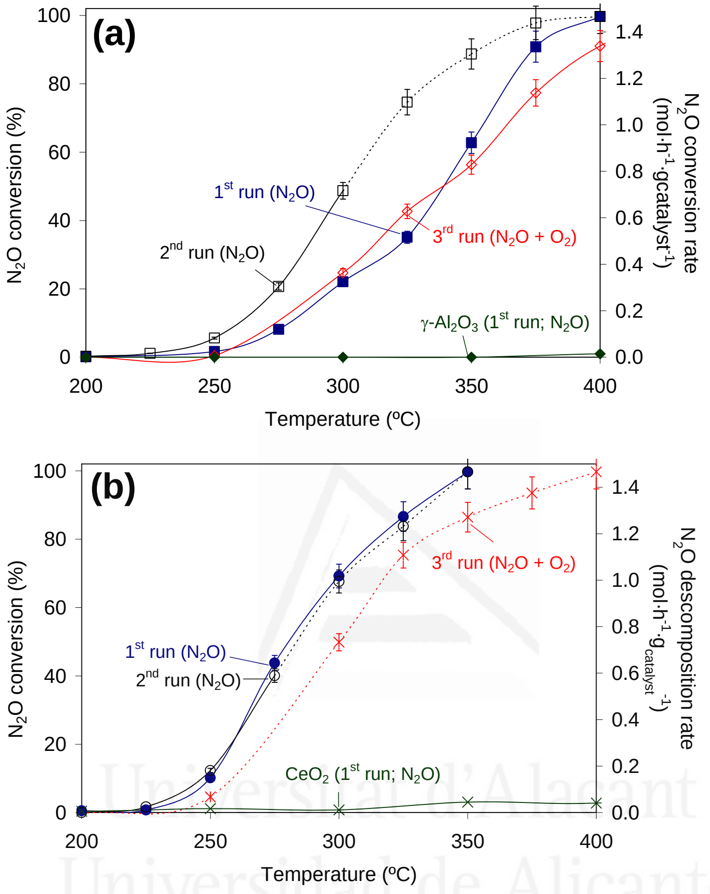

Figure 1. N_2O decomposition rates and conversion as a function of temperature in tests conducted with 1000 ppm N_2O/He (1st and 2nd runs) or with 1000 ppm N_2O/5 % O_2/He (3rd run). (a) Rh/Al_2O_3 and (b) Rh/CeO_2. (Continuous lines: Data obtained under chemical control of the reaction rate. Dashed lines: Data affected by mass diffusion).

N_2O decomposition experiments were performed with the Rh/CeO_2 and Rh/γ-Al_2O_3 catalysts under N_2O/He gas streams with different N_2O partial pressures in the range 100-1400 ppm. The results obtained were fitted with n-order kinetic equations. Figure 2 shows the experimental rates and the corresponding model fitting, from which the rate constants and the apparent N_2O reaction orders were estimated. Once the reaction constants where determined, Arrhenius type plots were used to determine the apparent activation energies.

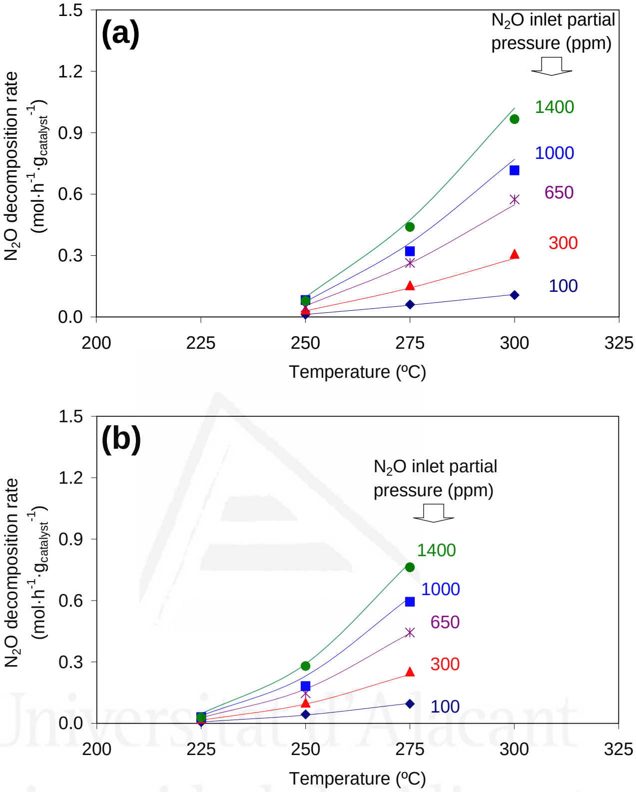

Figure 2. N_2O decomposition rates as a function of temperature in tests conducted with different N_2O inlet partial pressures. (a) $Rh/\gamma\text{-}Al_2O_3$ and (b) Rh/CeO_2.
Symbols: Experimental rates (all of them measured under kinetic control)
Lines: Kinetic model fitting.

The kinetic data obtained are compiled in Table 1. The apparent N_2O reaction orders are quite similar for both catalysts and the values obtained are lower than 1. This means that the N_2O decomposition rates are not linearly proportional to the N_2O partial pressure. The decomposition rate is faster in concentrated streams than in those diluted, which has important relevance for practical applications. Kapteijn et al. [1] performed a literature review on the catalytic decomposition of N_2O using a wide variety of materials including pure metals and metal oxides, spinel type mixed oxides, perovskites and hydrotalcites, zeolites and metals and transition metal oxides supported on alumina, silica and zirconia. In all cases, it was found that the apparent reaction order with respect to the N_2O partial pressure is 1 or slightly lower, suggesting that values below 1 may be related to the inhibitory effect of O_2 formed as reaction product. This argument appears to be valid for the catalysts studied in this chapter.

The estimated apparent activation energies, listed in Table 1, were different for Rh/γ-Al_2O_3 and Rh/CeO_2 (146 and 121 kJ/mol, respectively). These values are consistent with activation energies reported in the literature for noble metal and transition metal oxide catalysts (typically between 80 and 170 kJ/mol) [1], and are lower than the energy required to break the N-O bond in the N_2O molecule without catalyst participation (250-270 KJ/mol) [25-28], which needs about 625 ºC to occur spontaneously [29]. The different apparent activation energy obtained with Rh/γ-Al_2O_3 and Rh/CeO_2 implies that the N_2O decomposition mechanisms are different on the two catalysts or that there are differences in the rate-limiting step. In this chapter, the decomposition mechanism is studied by using different techniques and, as will be discussed in coming sections, important differences between Rh/γ-Al_2O_3 and Rh/CeO_2 were observed.

Table 1. Apparent N_2O reaction orders and activation energies for Rh/CeO_2 and Rh/γ-Al_2O_3 catalysts.

	N_2O reaction order	**Activation Energy (kJ/mol)**
Rh/γ-Al_2O_3	0.74±0.03	146±5
Rh/CeO_2	0.68±0.03	121±5

4.3.2. XPS characterization

The changes in the oxidation states of Rh and Ce surface species during the catalytic decomposition of N_2O and also the Rh/Al and Rh/Ce ratios, were studied by XPS. The fresh Rh/CeO_2 and Rh/γ-Al_2O_3 catalysts and also the catalysts after *in situ* treatments with 1000 ppm N_2O/Ar at different temperatures have been characterized by XPS.

Table 2 presents the Rh/Al and Rh/Ce atomic surface ratios measured by XPS. Rh/Ce ratios were higher than Rh/Al ratios regardless the temperature of the pre-treatment, suggesting that Rh dispersion on ceria is higher than on alumina both in fresh an in used catalysts. This result is not in agreement with the TEM-estimated rhodium particle sizes because, as mentioned, the average size of rhodium particles was almost equal in both catalysts (2.2 nm in Rh/CeO_2 and 2.3 nm in Rh/γ-Al_2O_3 [16]). In the TEM pictures, however, particles lower than 1 nm are hardly observed in the Rh/CeO_2 catalyst. However, they should exist (on Rh/CeO_2) but not on Rh/γ-Al_2O_3. It must be taken into account that the molecular weight of cerium is much higher to that of aluminium, and therefore the Rh-Al colour contrast is much better than the Rh-Ce contrast. This experimental limitation of TEM would overestimate the average particle size of Rh on the Rh/CeO_2 catalyst.

According to data on Table 2, the rhodium particles sinter under reaction conditions between 250 and 275 ºC, since the Rh/Al and Rh/Ce atomic ratios decrease above this threshold. However, Rh sintering seems to affect more to Rh/γ-Al_2O_3 than to Rh/Ceria, which is in agreement with the well-known stabilizing effect of ceria [30].

Table 2. XPS-measured atomic surface ratios in fresh catalysts and after 1 hour *in situ* treatments under 1000 ppm N_2O/He at different temperatures.

Temperature (ºC)	Rh/Al atomic ratio in Rh/γ-Al_2O_3	Rh/Ce atomic ratio in Rh/CeO_2
Fresh catalysts	0.013	0.084
250	0.011	0.099
275	0.006	0.066
300	0.007	0.063
325	0.006	0.056

Figure 3 shows XPS spectra obtained for Rh/γ-Al_2O_3 (Figure 3a) and Rh/CeO_2 (Figure 3b) corresponding to the electronic transitions from the Rh $3d^{3/2}$ and Rh $3d^{5/2}$ orbitals, with binding energies at 312-315 eV and 306-310 eV, respectively. It has been reported that the Rh $3d^{5/2}$ peaks of CeO_2-supported Rh^0 appear with binding energies in the range 307.0-307.7 eV, while Rh^{3+} species on the same support appear at 308.3-310.5 eV [17, 31, 32]. For Al_2O_3-supported Rh, it has been reported that the peaks corresponding to Rh^0 are shifted towards lower binding energies in comparison to Rh/CeO_2, appearing at ~ 306 eV [33]. In our fresh Rh/γ-Al_2O_3 and Rh/CeO_2 catalysts the Rh 3d$^{5/2}$, binding energies of about 309 eV are observed, suggesting the presence of Rh^{3+} species in both catalysts. This was expected, taking into account that the catalysts were calcined in air at 500 ºC.

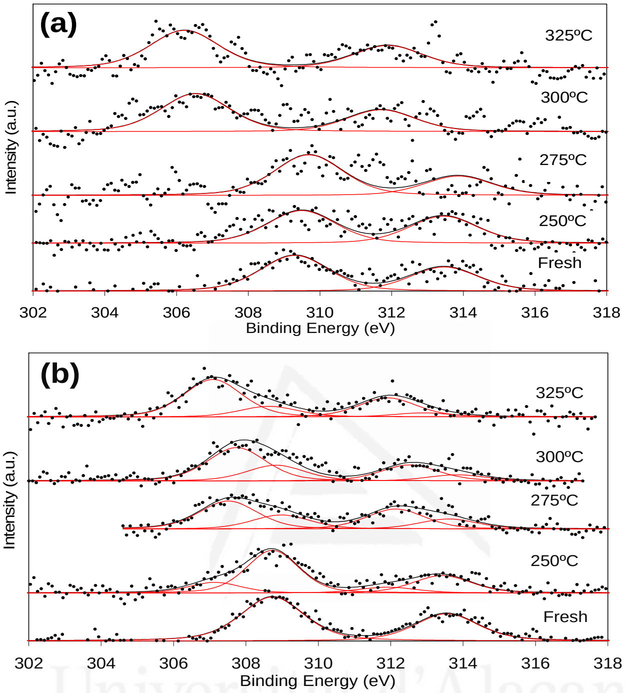

Figure 3. XPS spectra of the Rh 3d transition for the fresh catalysts and after *in situ* treatments with 1000 ppm N_2O/Ar for 1 hour at different temperatures. (a) Rh/γ-Al_2O_3 and (b) Rh/CeO_2.

These Rh^{3+} species are partially or totally reduced to Rh^0 during the catalytic decomposition of N_2O, as deduced from Figure 3, and the support has a major influence in this reduction process. For Rh/γ-Al_2O_3 (Figure 3a), the binding energy of the Rh 3d$^{5/2}$ transition decreases from around 309 eV at 275 ºC to about 306.4 eV at 300 ºC and higher temperature, suggesting the reduction of Rh^{3+} to Rh^0. Note that N_2O decomposition rates on Rh/γ-Al_2O_3 (see Figure 1, 1st run) are low below 275 ºC and increase significantly above this temperature. This would mean that Rh^0 is the most active species of rhodium when supported on alumina, which would also explain the increase in the N_2O decomposition rate during the second run, once Rh^{3+} species are reduced to Rh^0.

By contrast, the reduction of rhodium under reaction conditions progressively occurs with temperature in the Rh/CeO_2 catalyst (Figure 3b). In this case, the Rh $3d^{5/2}$ peaks can be deconvoluted into two peaks corresponding to species of Rh^{3+} and Rh^0 (high and low binding energy contributions, respectively). From the area of these deconvoluted peaks, the percentages of Rh^{3+} and Rh^0 could be estimated and the results obtained for Rh^0 are presented in Table 3. These results reveal that part of the Rh^{3+} species on the Rh/CeO_2 catalyst remain oxidized under reaction conditions at 325 ºC. According to these XPS results, the ceria support strongly interacts with rhodium and partially stabilises the cationic species under reaction conditions. This stabilising effect would explain the equal catalytic results (Figure 1b) obtained during the first and second cycle of experiments performed with the Rh/CeO_2 catalyst.

Table 3. XPS-estimated Rh^0 percentage in fresh catalysts and after 1 hour *in situ* treatments under 1000 ppm N_2O/He at different temperatures.

Temperature (ºC)	$Rh/\gamma\text{-}Al_2O_3$	Rh/CeO_2
Fresh catalysts	0	0
250	0	20
275	0	66
300	100	68
325	100	78

The behaviour of the cerium oxidation state under N_2O decomposition conditions has been also studied by XPS with the Rh/CeO_2 catalyst. For comparison, the same *in situ* treatments performed with 1000 ppm N_2O/Ar were repeated with fresh Rh/CeO_2 catalyst under pure Ar. The Ce 3d core level XPS spectra were analysed and, after deconvolution of the experimental spectra, the degree of ceria reduction was calculated from the ratio of the sum of the intensities of the u_0, u_1, v_0, and v_1 bands to the sum of the intensities of all the bands, following the method proposed elsewhere [34]. The Ce 3d photoelectron spectra of Rh/CeO_2 after *in situ* thermal treatments at 325 ºC under Ar and N_2O/Ar are shown as an example in Figure 4.

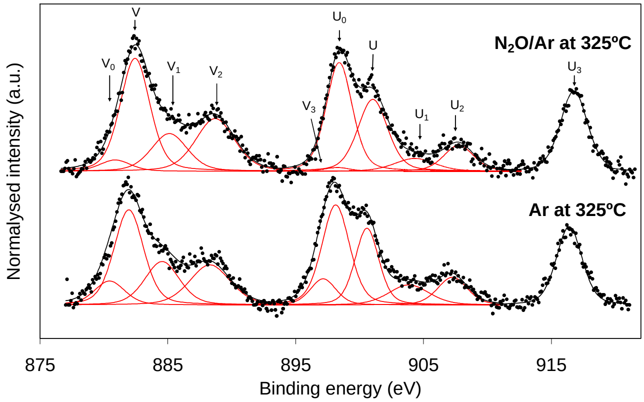

Figure 4. Ce 3d photoelectron spectra of Rh/CeO$_2$ after in situ thermal treatments at 325 ºC under Ar and N$_2$O/Ar.

The Ce^{3+} percentages determined by XPS after *in situ* treatments in 1000 ppm N$_2$O/Ar or pure Ar as a function of temperature are plotted in Figure 5. It is important to mention that ceria can be partially reduced under the high vacuum conditions of the XPS measurements. For this reason, the Ce^{3+} percentages determined by XPS are expected to differ from the real values under reaction conditions in a fixed-bed reactor. However, the differences between the Ce^{3+} trends obtained under Ar and N$_2$O/Ar provide valuable information about the catalysts behaviour. At 250 ºC, where the catalytic activity is very low (see Figure 1a), the Ce^{3+} percentage is equal (32.7%) after both thermal treatments performed, regardless the gas used. The Ce^{3+} percentage increases with temperature for experiments performed under pure Ar while it remains almost constant under 1000 ppm N$_2$O/Ar. This means that the ceria support loses oxygen during the thermal treatment under inert conditions,

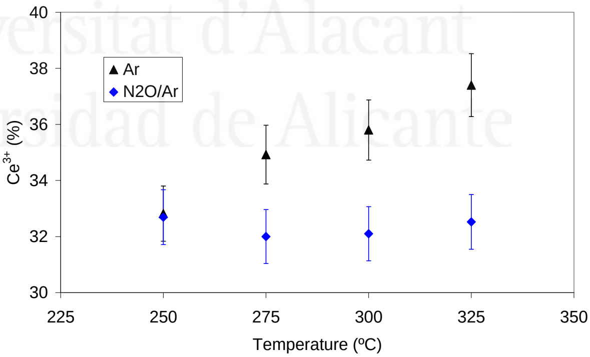

Figure 5. Ce^{3+} percentage with regard to Ce^{3+} + Ce^{4+} estimated from XPS analysis of the Rh/CeO$_2$ catalyst after *in situ* treatments with 1000 ppm N$_2$O/Ar or pure Ar for 1 hour at different temperatures.

while N_2O is able to restore the oxygen balance of ceria by oxidation of the vacant sites that are created on ceria upon thermal reduction.

4.3.3. In situ Raman spectroscopy characterization of the Rh/CeO_2 catalyst

The Rh/CeO_2 catalyst was characterized by Raman spectroscopy under reaction conditions. Raman spectra were recorded at different temperatures under gas streams of pure Ar or 1000 ppm N_2O/Ar. The spectra obtained at 150 and 350 ºC are shown in Figure 6a (Ar) and 6b (N_2O/Ar) as examples. The main peak at around 460 cm^{-1} is the typical fluorite peak of ceria assigned to the F_{2g} mode. This peak presents a shoulder between 500 and 700 cm^{-1} assigned to vacant sites of ceria and RhO_x species. The small peak at 230 cm^{-1} can be also attributed to RhO_x species, and is only observed in some of the spectra [35-37]. The gas composition used for the thermal treatments significantly affects the changes observed in the Raman spectra of the Rh/CeO_2 catalyst. The RhO_x peak at 230 cm^{-1} decreases at 350 ºC in Ar (Figure 6a) but remains unchanged in N_2O/Ar. This indicates that the RhO_x species are thermally unstable in Ar atmosphere while they are stabilized in the presence of N_2O.

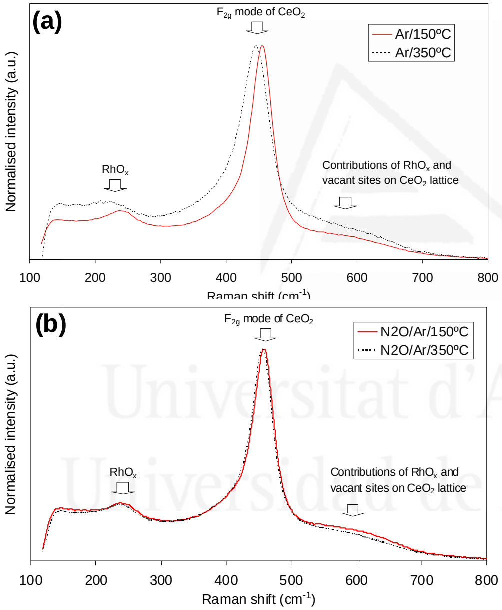

Figure 6. Raman spectra of the Rh/CeO_2 catalyst obtained at different temperatures under (a) Ar and (b) 1000 ppm N_2O/Ar.

On the other hand, the intensity of the shoulder between 500 and 700 cm^{-1} increases from 150 to 350 ºC in Ar (Figure 6a), due to the creation of oxygen vacancies on ceria, while it slightly decreases under N_2O/Ar, because some oxygen vacancies are filled up by N_2O. Finally, attention must be paid to the position of the F_{2g} peak. In Figure 7, the position of the F_{2g} peak for experiments performed under Ar and N_2O/Ar is plotted versus temperature. In both gases, the position of the F_{2g} peak decreases with temperature reaching a roughly constant value at 150 ºC in N_2O/Ar and at 250 ºC in pure Ar. This decrease in the F_{2g} peak position can be attributed to the expansion of the unit cell of ceria due to the partial reduction of Ce^{4+} cations (0.97 Å) to larger Ce^{3+} cations (1.14 Å). Once more, it is likely that the reduction that occurred under the inert gas atmosphere is partially inhibited by N_2O, and the shift in the F_{2g} position is lower in N_2O/Ar than in pure Ar. These differences are mainly important above 250 ºC, where N_2O decomposition takes place (see Figure 1b). This further suggests the active participation of the CeO_2 support in the N_2O decomposition mechanism over the Rh/CeO_2 catalyst.

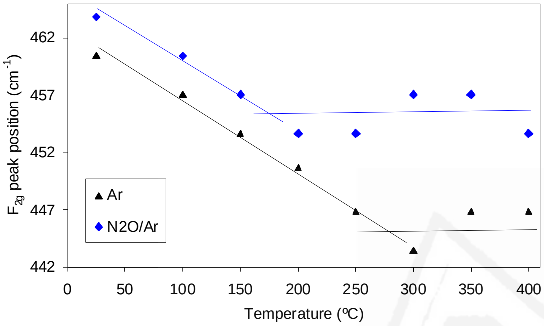

Figure 7. Position of the F_{2g} ceria peak determined by Raman spectroscopy during *in situ* thermal treatments of the Rh/CeO_2 catalyst under Ar or 1000 ppm N_2O/Ar.

4.3.4. Pulse experiments with isotopic gases ($^{15}N_2{}^{18}O$ and $^{18}O_2$)

In order to further analyse the catalyst oxygen participation in the N_2O decomposition mechanism, pulse experiments were performed with isotopic gases ($^{15}N_2{}^{18}O$ and $^{18}O_2$). Qualitative information was obtained from the shape of the reactant ($^{15}N_2{}^{18}O$ and $^{18}O_2$) and product profiles. As an example, the MS profiles monitored after $^{15}N_2{}^{18}O$ pulses to Rh/CeO_2 at 300 ºC and 400 ºC are included in Figure 8. These profiles reveal that there is no delay neither between the profiles of reactants and products, nor regarding the reference Ar pulses. This means that the rates of all the oxygen exchange processes taking place upon $^{15}N_2{}^{18}O$ and $^{18}O_2$ pulsing, are much faster than the measuring time (1 second frequency; complete relaxation of the system takes about 80 seconds). This is consistent with previous $^{18}O_2$ pulse experiments performed with bare and La^{3+}-doped ceria in a TAP device, which operates in the milliseconds range of time [19, 20].

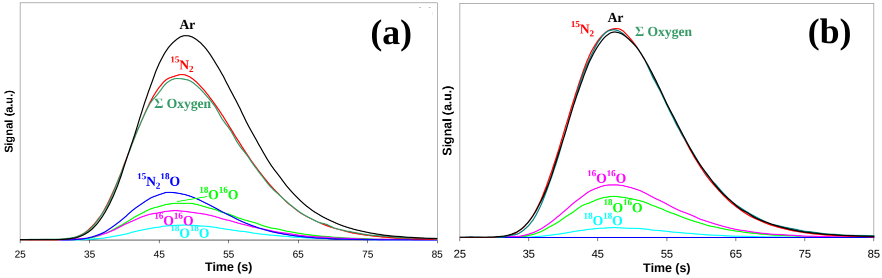

Figure 8. MS profiles monitored after $^{15}N_2{}^{18}O$ pulses to Rh/CeO_2 at (a) 300 ºC and (b) 400 ºC.

4.3.4.1. $^{15}N_2{}^{18}O$ pulses

Figure 9 presents results of $^{15}N_2{}^{18}O$ pulses over $Rh/\gamma\text{-}Al_2O_3$ and $\gamma\text{-}Al_2O_3$ (Figure 9a), and Rh/CeO_2 and CeO_2 (Figure 9b). The $^{15}N_2{}^{18}O$, $^{15}N_2{}^{16}O$ and $^{15}N_2$ percentages in the gas mixture after the interaction with the solid bed are plotted as a function of temperature. Additionally, Total oxygen (ΣOxygen) profiles are also plotted, calculated as twice the sum of the percentage of the different O_2 species, that is:

$$\sum\text{Oxygen: } 2\cdot({}^{18}O_2 + {}^{18}O^{16}O + {}^{16}O_2)$$

Note that the ^{16}O atoms come from the solids ($Rh/\gamma\text{-}Al_2O_3$, $\gamma\text{-}Al_2O_3$, Rh/CeO_2 or CeO_2) while ^{18}O atoms come from the pulsed gas.

For $^{15}N_2{}^{18}O$ pulses, the processes that cause breaking and formation of bonds are: (i) Oxygen exchange between $^{15}N_2{}^{18}O$ and solids, which would lead to $^{15}N_2{}^{16}O$ release and/or (ii) $^{15}N_2{}^{18}O$ decomposition with $^{15}N_2$ and O_2 release ($^{18}O_2$, $^{18}O^{16}O$ and/or $^{16}O_2$). The contribution of process (i) is negligible in most cases and no significant $^{15}N_2{}^{16}O$ formation is observed in most pulse experiments. N_2O decomposition (ii) is the main process taking place. Only the CeO_2 support exchanges a very small amount of oxygen with the $^{15}N_2{}^{18}O$ gas leading to $^{15}N_2{}^{16}O$ release at 400 ºC (Figure 9b), but this phenomenon is not observed for $\gamma\text{-}Al_2O_3$ (Figure 9a).

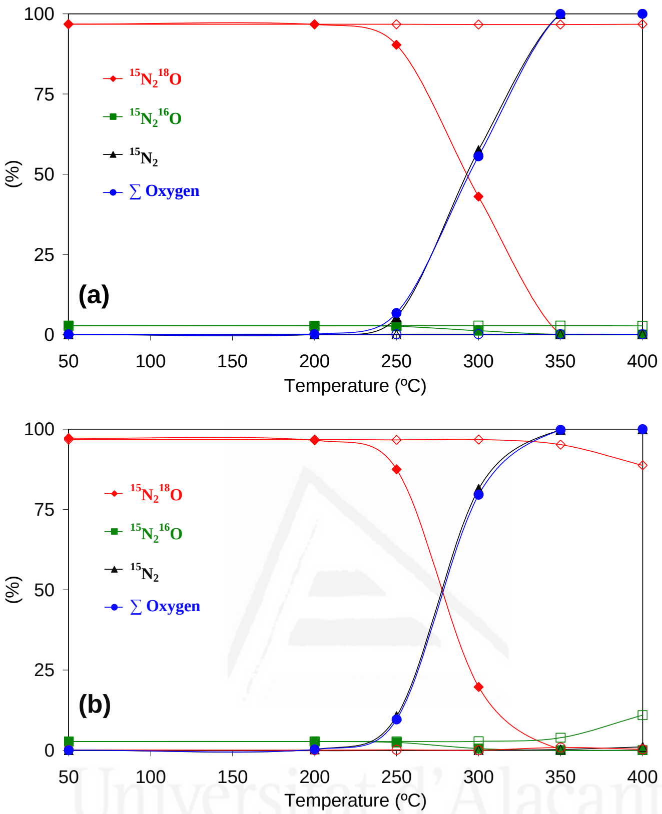

Figure 9. $^{15}N_2{}^{18}O$ decomposition over (a) Rh/γ-Al_2O_3 and γ-Al_2O_3 (b) Rh/CeO_2 and CeO_2. Open symbols: supports; solid symbols: catalyst.

N_2O decomposition in the pulse experiments (Figure 9) occurs above 250 ºC for both catalysts. This temperature is quite consistent with the range of temperatures of N_2O decomposition in the conventional flow experiments (Figure 1), in spite of the differences between both experimental procedures. The pulse experiments confirm that the Rh/CeO_2 catalyst is more active for N_2O decomposition than Rh/γ-Al_2O_3 and that the supports have no activity in the range of temperature studied in these experiments.

The stoichiometric formation of O_2 and N_2 from N_2O is observed in pulse experiments, since the ΣOxygen and $^{15}N_2$ percentage profiles overlap in Figure 9. This means that the amount of nitrogen species stored on the catalysts during the N_2O decomposition process, which were identified by *in* *situ* DRIFTS experiments (see Figures 13 and 14 and further discussion), is negligible relative to the amount of N_2O pulsed, and that there is no appreciable oxygen accumulation on the catalysts under the experimental conditions of the pulse experiments.

Special attention must be paid to the nature of the O_2 molecules evolved as $^{15}N_2{}^{18}O$ decomposition product. In Figure 10, the percentage of each O_2 species ($^{18}O_2$, $^{18}O^{16}O$ and $^{16}O_2$) with regard to the total O_2 has been plotted. Important differences in the O_2 species distribution are noticed between Rh/γ-Al_2O_3 (Figure 10a) and Rh/CeO_2 (Figure 10b). The most abundant O_2 specie obtained with the Rh/γ-Al_2O_3 catalyst is $^{18}O_2$, which means that most of the O_2 delivered as N_2O decomposition product comes from the $^{15}N_2{}^{18}O$ molecules pulsed. The formation of $^{18}O^{16}O$ (and some $^{16}O_2$), which also occurs in a lower extent than $^{18}O_2$, implies a certain participation of the catalyst oxygen in the N_2O decomposition pathway. This will be discussed in detail afterwards.

The proportion of the different O_2 species evolved as $^{15}N_2{}^{18}O$ decomposition product significantly changes for Rh/CeO_2 (Figure 10b). The main O_2 products are $^{16}O_2$ and $^{18}O^{16}O$, pointing out that the catalyst oxygen is actively involved in the N_2O decomposition mechanism. This will be discussed in more detail below.

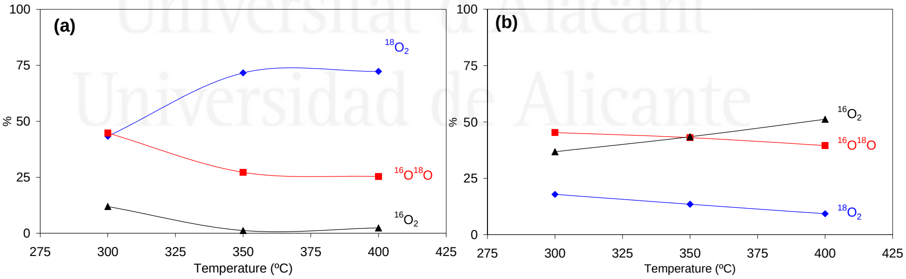

Figure 10. Nature of the O_2 species evolved as $^{15}N_2{}^{18}O$ decomposition product with catalysts (a) Rh/γ-Al_2O_3 (b) Rh/CeO_2.

4.3.4.2. $^{18}O_2$ pulses

Understanding the oxygen exchange between $^{18}O_2$ and the catalysts presents a double interest in the context of this study. On the one hand, O_2 released as N_2O decomposition product could interact again with the catalysts, and on the other hand, N_2O decomposition in O_2 rich streams has practical relevance.

The exchange of oxygen between $^{18}O_2$ molecules and the catalyst can yield $^{18}O^{16}O$ and/or $^{16}O_2$. Figure 11 shows the $^{18}O_2$, $^{16}O_2$ and $^{18}O^{16}O$ percentages upon $^{18}O_2$ pulses over Rh/γ-Al_2O_3 and γ-Al_2O_3 (Figure 11a) and over Rh/CeO_2 and CeO_2 (Figure 11b) at different temperatures. Oxygen exchange between the $^{18}O_2$ gas molecules pulsed and the supports is negligible in most experiments, but the presence of rhodium in the catalysts leads to the exchange of oxygen. With both catalysts, ^{16}O-containg O_2 molecules release above 200 ºC, the oxygen exchange increasing with temperature. As expected, the phenomenon is much higher for Rh/CeO_2 than for Rh/γ-Al_2O_3 [8-16, 21, 22].

For Rh/γ-Al_2O_3 (Figure 11a), the main ^{16}O-containing product is $^{18}O^{16}O$. This indicates that the exchange of the oxygen atoms from the pulsed $^{18}O_2$ molecules occurs sequentially, and only single exchange takes place under the experimental conditions used in these tests. Therefore, since re-adsorption of $^{16}O^{18}O$ upon $^{18}O_2$ pulses does not occur after the first oxygen exchange, the re-adsorption of O_2 molecules on Rh/γ-Al_2O_3, evolving as N_2O decomposition product is expected to be also minor under the experimental conditions of these pulse experiments.

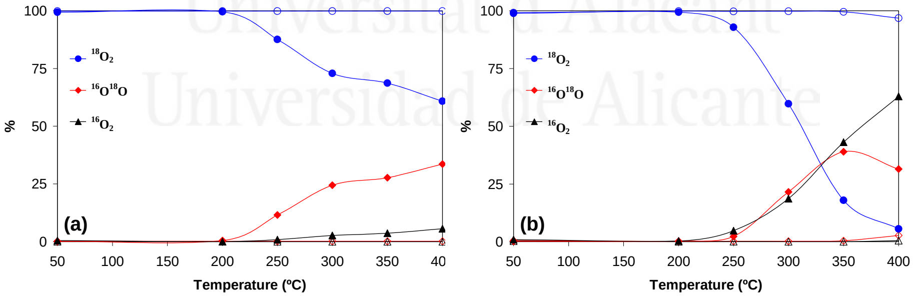

Figure 11. Nature of the O_2 species evolved upon $^{18}O_2$ interaction with (a) Rh/γ-Al_2O_3 and γ-Al_2O_3 (b) Rh/CeO_2 and CeO_2. Open symbols: supports; solid symbols: catalysts.

By contrast, both $^{16}O^{18}O$ and $^{16}O_2$ evolve above 200 ºC after $^{18}O_2$ pulses over the Rh/CeO_2 catalyst (Figure 11b). The $^{16}O^{18}O$ percentage reaches a maximum level at 350 ºC while the $^{16}O_2$ percentage rises monotonically with temperature. The formation of $^{16}O^{18}O$ shows that single exchange of the $^{18}O_2$

oxygen atoms takes place. The formation of $^{16}O_2$ can occur by re-adsorption of $^{16}O^{18}O$ molecules and/or by double exchange of oxygen atoms once $^{18}O_2$ is adsorbed on the catalyst surface.

Table 4 shows the total amounts of ^{16}O atoms exchanged by the two catalysts during the pulse experiments, calculated on the basis of ^{16}O present in each catalyst as Rh_2O_3 or total (Rh_2O_3 + support oxygen). For Rh/CeO_2, the amount of ^{16}O exchanged is much higher than the amount of oxygen on Rh_2O_3 (442%), confirming that oxygen atoms in CeO_2 are involved in the exchange processes. However, the amount of oxygen exchanged by Rh/CeO_2 with regard to the total amount of oxygen on this catalyst (Rh_2O_3 + CeO_2 oxygen) is very low (0.055%), pointing out that a large reservoir of non-exchanged oxygen remains on the catalyst after the pulse experiments. In the case of Rh/γ-Al_2O_3, the amount of oxygen exchanged only slightly exceeds the amount of Rh_2O_3 oxygen (145%). This confirms that the support γ-Al_2O_3 is only able to exchange a very low amount of oxygen with the isotopic gases, much less than CeO_2.

Table 4. Oxygen exchanged between gas molecules and catalysts in the pulse experiments performed with isotopic gases.

	Oxygen exchanged on Rh_2O_3 basis (%)	**Oxygen exchanged on Rh_2O_3 + support basis (%)**
Rh/γ-Al_2O_3	145	0.011
Rh/CeO_2	442	0.055

4.3.5. In situ DRIFTS-MS experiments

The surface of the catalysts was studied by DRIFT spectroscopy during *in situ* N_2O decomposition experiments. Also, MS monitoring has been recorded during the DRIFTS experiment. As an example, the data for Rh/γ-Al_2O_3 in 1000 ppm N_2O/He is shown in Figure 12. It is noted here that the catalytic decomposition of N_2O in the DRIFTS cell occurs in the same range as temperatures observed in the flow reactor (Figure 1) for both catalysts. The only difference between the results obtained in the flow reactor and in the DRIFTS cell is the N_2O decomposition rate reached at each temperature, which is lower in the DRIFTS cell due to gas diffusion effects. Figures 13 and 14 show the DRIFT spectra recorded during the DRIFTS-MS experiments.

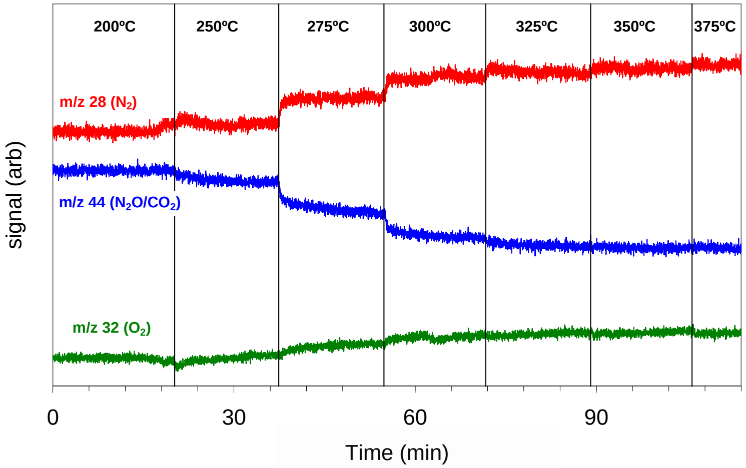

Figure 12. MS profiles measured during the DRIFTS-MS experiment performed with Rh/γ-Al_2O_3 under 1000 ppmN_2O/He.

Figure 13 shows the DRIFT spectra recorded with the support γ-Al_2O_3 in N_2O and N_2O + O_2 (Figures 13a and 13b, respectively). The spectra for the Rh/γ-Al_2O_3 catalyst under the same conditions are shown in Figures 13c and 13d, respectively. To clearly observe nitrogen-containing surface species both on the support and on the catalyst, 200 ºC or higher temperatures are required. The N-N stretching frequency of adsorbed N_2 or N_2O on metal oxides was reported to absorb within a wide range of frequencies, typically between 2400 and 2150 cm^{-1} [38-41]. In Figures 13 (a-d), above 200 ºC, a quite intense absorption band is observed at 2315 cm^{-1} which could be assigned to adsorbed N_2O. Nitrites, nitrates and nitro compounds typically show bands below 1700 cm^{-1}. In all spectra recorded at temperatures higher than 200 ºC several peaks are identified below this wavenumber. The spectra of the γ-Al_2O_3 support and Rh/γ-Al_2O_3 catalyst under N_2O flow (Figures 13a and 13c, respectively) are consistent with the formation of monodentate nitrites (bands in the range 1500-1400 cm^{-1}), monodentate nitrates (bands at 1570-1540 cm^{-1} and at 1290-1250 cm^{-1}) and/or nitro compounds (bands around 1345 cm^{-1}). The existence of nitrites, nitrates or nitro compounds in these spectra implies that the reaction between N_2O and oxygen at the support or catalyst surface is taking place.

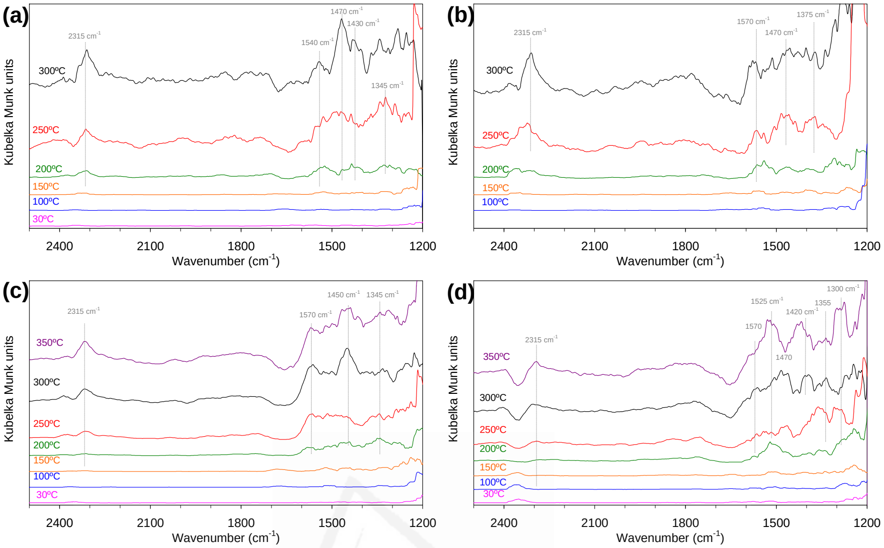

Figure 13. *In situ* DRIFT spectra of (a) γ-Al_2O_3 under N_2O, (b) γ-Al_2O_3 under N_2O +O_2, (c) Rh/γ-Al_2O_3 under N_2O, and (d) Rh/γ-Al_2O_3 under N_2O + O_2.

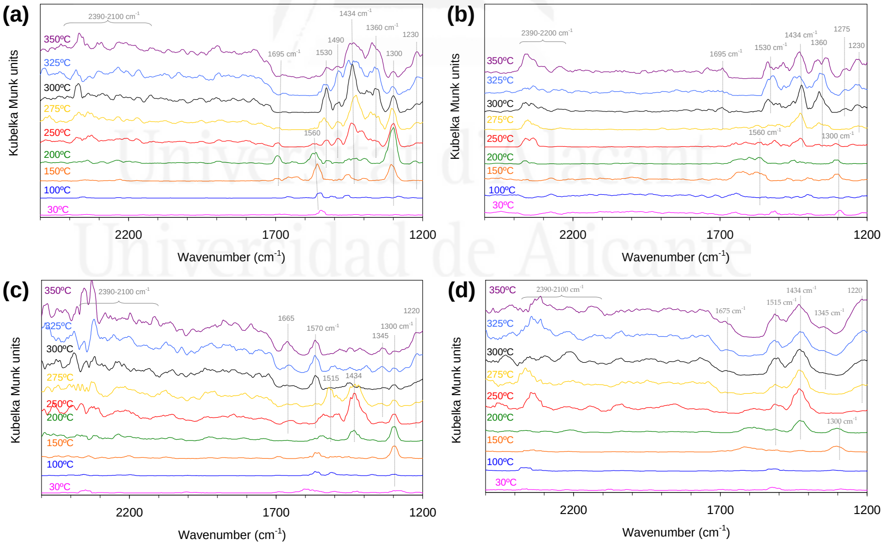

Figure 14. *In situ* DRIFT spectra of (a) CeO_2 under N_2O, (b) CeO_2 under N_2O +O_2, (c) Rh/CeO_2 under N_2O, and (d) Rh/CeO_2 under N_2O + O_2.

In the presence of N_2O + O_2 (Figures 13b and 13d) similar bands are observed, but the relative intensity of these bands is different from that measured under N_2O only. The formation of nitrates seems to be favoured at expenses of nitrites, suggesting that, as expected, the surface species appear to be more oxidized under N_2O + O_2 than under N_2O only.

The main conclusion from the DRIFTS experiments presented in Figure 13 is that the spectra of γ-Al_2O_3 (without catalytic activity in the temperature range studied) and Rh/γ-Al_2O_3 (with catalytic activity) are quite similar. This suggests that most nitrogen species observed on the alumina samples upon N_2O exposure are spectator species and are not involved in the N_2O decomposition mechanism. This also confirms, as suggested earlier in this chapter, that not all the adsorption sites suitable for N_2O adsorption are active for N_2O decomposition. The similarities between the Rh/γ-Al_2O_3 and γ-Al_2O_3 spectra further suggest that the surface nitrogen species are mainly created on the γ-Al_2O_3 support and not on rhodium.

This scenario significantly changes with the ceria samples. Figure 14 shows the DRIFT spectra recorded with the CeO_2 support under N_2O and N_2O + O_2 (Figures 14a and 14b, respectively), and their counterpart spectra for the Rh/CeO_2 catalyst (Figures 14c and 14d, respectively). As a general conclusion, the number of bands in the DRIFT spectra of Figure 14 (ceria samples) is much higher than that in Figure 13 (alumina samples), which evidences that the ceria surface is more heterogeneous than that of alumina.

Bands between 2390 and 2100 cm^{-1} appeared in the ceria samples above 200 ºC, which could be assigned to the N-N stretching frequency of adsorbed N_2, produced as N_2O decomposition product, or of adsorbed N_2O [38-41]. The number of bands in this range of values is much higher in the ceria samples (Figures 14(a-d)) than in those of alumina (Figures 13(a-d)), which only showed a single band at 2315 cm^{-1}, once more evidency the higher heterogeneity of the ceria surface. The appearance of several peaks in the Rh/CeO_2 catalysts, which did not appear in Rh/γ-Al_2O_3, should correspond to the existence of N_2 and/or N_2O adsorbed on different rhodium and/or cerium oxide sites.

The formation and transformation with temperature of absorption bands below 1700 cm^{-1} is significant in Figures 14(a-d). In bare CeO_2 below 200 ºC, the absorption bands identified are consistent with the formation of monodentate nitrates, both in the absence and presence of O_2 (Figures 14a and 10b, respectively), with bands at 1560 and 1300 cm^{-1} which progressing together. Above this temperature, these bands decrease and the spectra evidence the formation of other nitrogen compounds. The bands at 1695 and 1230 cm^{-1} are consistent with the formation of bridged nitrates and those at 1530 and 1300 cm^{-1} with bidentate nitrates. Note that bridged and bidentate nitrates are more stable than monodentate nitrates, and therefore, they appear at higher temperatures. In addition, bands compatible with the formation of monodentate nitrites (1434 cm^{-1}) and nitro groups (1360 cm^{-1}) remain on bare CeO_2 between 200 and 350 ºC. The formation of nitrites, nitrates or nitro compounds in these spectra suggests the oxidation of N_2O with ceria oxygen. The complex spectra in Figures 14a and 14b are in agreement with the previously commented heterogeneity of the ceria surface, and illustrate the high affinity of this metal oxide towards N_2O chemisorption and oxidation.

Below 200 ºC, the nature of the surface species formed on CeO_2 (Figures 14a and 14b) appears to be similar to the species created on Rh/CeO_2 (Figures 14c and 14d). This suggests that in the Rh/CeO_2 catalyst these species are mainly created on ceria surface sites rather than on rhodium sites. However, the evolution of the surface species created on Rh/CeO_2 with temperature is very different to that observed on CeO_2. This could be related to the catalytic activity of Rh/CeO_2 for N_2O decomposition. Under N_2O (Figure 14c) and above 275 ºC, once N_2O is being decomposed on Rh/CeO_2, most bands in the range 1550-1200 cm^{-1} disappear. This means that monodentate nitrites and bidentate nitrates are not stable under reaction conditions. As it has been deduced from the pulse experiments with isotopic N_2O, oxygen atoms of ceria are involved in N_2O decomposition over Rh/CeO_2. This implies the constant creation of oxygen vacancies on ceria, and filling of these vacancies by oxygen from N_2O. The stabilization of certain nitrites and nitrates appears to be not possible under the dynamic behaviour of ceria oxygen atoms. In the presence of O_2 (Figure 14d), the depletion of surface nitrogen species under reaction conditions is slightly different than in the absence of O_2 (Figure 14c). For instance, monodentate nitrites, but not nitrates, seem to remain stable during N_2O decomposition under $N_2O + O_2$. This is consistent with the previous hypothesis, that under $N_2O + O_2$, O_2 keeps ceria more oxidized than under only N_2O, and as a result ceria oxidizes the chemisorbed N_2O more easily.

The main conclusion of the DRIFTS study is that both ceria and alumina chemisorb and oxidise N_2O, and that the behaviour of chemisorbed nitrogen species during N_2O decomposition on rhodium catalysts depends on the nature of the support. While N_2O decomposition over Rh/γ-Al_2O_3 does not affect the nitrogen surface species created on the γ-Al_2O_3 support, some of the oxidized nitrogen species created on ceria (monodentate nitrites and bidentate nitrates, for instance) are not stable during N_2O chemisorption. The reason for this could be that the alumina support is not involved in the N_2O decomposition mechanism while ceria oxygen, which is required to oxidise N_2O, is involved in the N_2O decomposition process on ceria.

4.4. Discussion

The different techniques used in the current study provide complementary information about the N_2O decomposition mechanisms catalysed by Rh/γ-Al_2O_3 and Rh/CeO_2, explaining why the latter catalyst is more active than the former one. As a main conclusion, it is demonstrated that the CeO_2 support, in the presence of Rh, is actively involved in the N_2O decomposition mechanism while γ-Al_2O_3 is not. The high catalytic activity for N_2O decomposition of RhO_x/CeO_2 catalysts was already reported, and it was proposed, based on ESR analysis, that the low-temperature activity of Rh/CeO_2 catalysts for N_2O decomposition relies on electron rich sites at the interface between the dispersed rhodium particles and the ceria support [42]. Further evidences of the synergy between rhodium and ceria in N_2O decomposition are observed in the current study.

Once the Rh/γ-Al_2O_3 and Rh/CeO_2 catalysts are contacted with a N_2O stream, surface nitrogen species are created on the supports as demonstrated by the *in situ* DRIFTS experiments (see Figures 13 and 14). These species include chemisorbed N_2O and oxidized nitrogen species like nitrites or nitrates. The oxidized nitrogen species are spectator species and are not involved in the N_2O decomposition mechanism. At 200 ºC or higher temperature, where

N_2O decomposition into N_2 and O_2 takes place (see Figure 1), the oxidized nitrogen species are stable on $Rh/\gamma\text{-}Al_2O_3$ while not all of them are stable on Rh/CeO_2. This is because the ceria oxygen required to oxidise N_2O is involved in the N_2O decomposition process.

From the pulse experiments performed with $^{15}N_2{}^{18}O$, it is found that several redox processes occur on the catalysts during N_2O decomposition. $^{15}N_2{}^{18}O$ decomposition on $Rh/\gamma\text{-}Al_2O_3$ yields $^{15}N_2 + {}^{18}O^{16}O$, and an oxidized rhodium site ($Rh^*\text{-}{}^{16}O$) becomes reduced (Rh^*) in this process (observed by XPS):

$$Rh^*\text{-}{}^{16}O + {}^{15}N_2{}^{18}O \leftrightarrow Rh^* + {}^{15}N_2 + {}^{18}O^{16}O \qquad \text{Step 1}$$

This reaction step explains the reduction of rhodium under reaction conditions, as deduced by XPS (Figure 3a), and the $^{18}O^{16}O$ emission in pulse experiments (Figure 10a). In the case of the $Rh/\gamma\text{-}Al_2O_3$ catalyst, the reoxidation of rhodium sites takes place with gas phase $^{15}N_2{}^{18}O$, as described by step 2:

$$Rh^* + {}^{15}N_2{}^{18}O \leftrightarrow Rh^*\text{-}{}^{18}O + {}^{15}N_2 \qquad \text{Step 2}$$

Once the redox process described by steps 1 and 2 has occurred, and part of the ^{16}O atoms (on Rh sites) have been removed, the decomposition of further $^{15}N_2{}^{18}O$ molecules yields $^{18}O_2$ instead of $^{18}O^{16}O$. This is the result of the progressive occupation of oxidized rhodium sites with ^{18}O atoms:

$$Rh^*\text{-}{}^{18}O + {}^{15}N_2{}^{18}O \leftrightarrow Rh^* + {}^{15}N_2 + {}^{18}O_2 \qquad \text{Step 1bis}$$

This explains why $^{18}O_2$ is the main molecular oxygen specie yielded in the $Rh/\gamma\text{-}Al_2O_3$-catalysed N_2O decomposition (Figure 10a).

The formation of $^{16}O_2$, which is minor when $^{15}N_2{}^{18}O$ is decomposed on the $Rh/\gamma\text{-}Al_2O_3$ catalyst (Figure 10a), would occur by recombination of two ^{16}O-containing oxidized rhodium sites:

$$2Rh^*\text{-}{}^{16}O \leftrightarrow 2Rh^* + {}^{16}O_2 \qquad \text{Step 3}$$

The preferential formation of $^{18}O^{16}O$ (step 1) with regard to $^{16}O_2$ (step 3) by the Rh/γ-Al_2O_3 catalyst (Figure 10a) suggests that the Eley-Rideal mechanism (reduction of the noble metal sites by N_2O; step 1) is the main reaction pathway, while the Langmuir-Hinshelwood mechanism (recombination of two oxygen atoms on noble metal sites yielding molecular oxygen; step 3) has a marginal contribution.

The N_2O decomposition mechanism described by steps 1, 1bis and 2 is valid for the Rh/γ-Al_2O_3 catalyst, but the reaction pathway is much more complicated on Rh/CeO_2, since the steps 1, 1bis and 2 are not able to explain the high proportion of $^{16}O_2$ yielded by this catalyst (Figure 10b). The *in situ* XPS experiments (Figure 3) demonstrate that ceria stabilises the cationic species of rhodium during N_2O decomposition while rhodium on Rh/γ-Al_2O_3 is reduced to Rh^0. Therefore, the sequence of steps 1, 1bis and 2 seems to occur preferentially on reduced rhodium, being the main reaction pathway for Rh/γ-Al_2O_3 and having a minor contribution for Rh/CeO_2.

The participation of ceria oxygen in the N_2O decomposition mechanism over Rh/CeO_2 is supported by the fact that the amount of ^{16}O atoms released during the pulse experiments with isotopic gases is much higher than the amount of oxygen on Rh_2O_3 (see Table 4). Taking the XPS results into account, the participation of the support could consist of oxygen transfer from ceria to rhodium (step 4), that is, once N_2O reduces a rhodium site via step 1, the reoxidation of this site could be accomplished by ceria oxygen:

$$Rh^* + Ce^*\text{-}^{16}O \leftrightarrow Rh^*\text{-}^{16}O + Ce^* \qquad \text{Step 4}$$

Most likely, this oxygen transfer is related to the high dispersion of Rh observed on CeO_2. In the case of Rh/CeO_2 catalyst, the active site for rhodium is unlikely to be Rh^0, but RhO_x species at the Rh-ceria interface, as proposed by Cunningham et al. [46]. The transfer of oxygen from ceria to the rhodium site leads to the creation of vacant sites on the ceria support (Ce*), and ceria must restore the oxygen balance re-oxidising such vacant sites by $^{15}N_2{}^{18}O$:

$$Ce^* + {}^{15}N_2{}^{18}O \leftrightarrow Ce^*\text{-}^{18}O + {}^{15}N_2 \qquad \text{Step 5}$$

The constant Ce^{3+} percentages found from XPS (Figure 5) on Rh/CeO_2 after *in situ* N_2O decomposition treatments supports that the step 5 takes place. The experiments demonstrate that the oxygen vacancies on ceria can be reoxidized by N_2O. Additional experimental evidence supporting the participation of step 5 is obtained by *in situ* Raman spectroscopy experiments (Figure 7). These experiments demonstrated that the thermal expansion of the ceria lattice, due to the partial reduction of Ce^{4+} cations to Ce^{3+}, is hindered by reoxidation of these Ce^{3+} cations in the presence of N_2O. The sequence of steps 1 + 4 + 5 can explain the emission of $^{18}O^{16}O$ by the Rh/CeO_2 catalyst upon $^{15}N_2{}^{18}O$ decomposition (Figure 10b). Additionally, the high proportion of $^{16}O_2$ yielded by this catalyst could be mainly attributed to the recombination of oxygen atoms on two oxidized sites. These oxidized sites could be two rhodium sites (step 3), two cerium sites (step 6) or a rhodium site and a cerium site (step 7):

$$2Ce^*\text{-}^{16}O \leftrightarrow 2Ce^* + {}^{16}O_2 \qquad \text{Step 6}$$

$$Rh^*\text{-}^{16}O + Ce^*\text{-}^{16}O \leftrightarrow Rh^* + Ce^* + {}^{16}O_2 \qquad \text{Step 7}$$

Taking the described mechanisms and the different experimental observations into account, it can be concluded that Rh^0 are the most active sites for N_2O decomposition on $Rh/\gamma\text{-}Al_2O_3$, while the opposite occurs on the Rh/CeO_2 catalyst. Despite the relative increase of Rh^0 on Rh/CeO_2 with temperature (Table 3), the highest activity is expected to remain on RhO_x sites in intimate contact with ceria [42]. The experimental evidence to support this is the participation of ceria oxygen in the N_2O decomposition mechanism (as deduced from isotopic exchange experiments) even at temperatures where Rh^0 percentage is higher than that of Rh^{+3} (>275 ºC, Table 3). The $N_2{}^{18}O$ decomposition mechanism occurring exclusively on Rh^0 sites would yield $^{18}O_2$ (mechanism described by steps 2 and 1b). However $^{16}O_2$ and $^{16}O^{18}O$ are the main O_2 species evolved above 275 ºC upon N_2O decomposition on the Rh/CeO_2 catalysts (Figure 10b). This means that most N_2O is decomposed throughout a mechanism that involves steps 4 to 7. In this reaction pathway, step 4 is responsible to keep partially oxidised rhodium sites stable under reaction conditions.

In conclusion, more than one N_2O decomposition mechanisms appear to occur in parallel on Rh/CeO_2, and all the processes described by steps 1 to step 7 participate to some extent in the N_2O decomposition pathways. The reaction mechanisms occurring on Rh/CeO_2 are more effective than those based exclusively on steps 1, 1bis and 2 (occurring on Rh/γ-Al_2O_3), because the active sites for N_2O chemisorption and decomposition are not only located on rhodium but also on ceria. Taking the well-known mobility of oxygen atoms within the ceria framework into account, it is expected that the full ceria surface can potentially form oxygen vacancies where N_2O can be decomposed.

4.5. Conclusions

The multi-technique study of the N_2O decomposition on Rh/γ-Al_2O_3 and Rh/CeO_2 as presented in this chapter allows concluding that:

- The Rh/γ-Al_2O_3 catalyst is less active for N_2O decomposition than Rh/CeO_2, and the apparent activation energies (146 and 121 kJ/mol, respectively) are consistent with such differences in activity. The different activity is related to the fact that the CeO_2 support is actively involved in the N_2O decomposition mechanism while γ-Al_2O_3 is not.

- The CeO_2 support strongly interacts with Rh and stabilises very small, oxidized noble metal particles during N_2O decomposition, while rhodium on Rh/γ-Al_2O_3 is reduced to Rh^0 under the same conditions.

- N_2O decomposition over Rh/γ-Al_2O_3 mainly occurs via the Eley-Rideal mechanism resulting in the successive oxidation and reduction of the noble metal sites by N_2O. The Langmuir-Hinshelwood mechanism, resulting in oxidation of Rh by N_2O and recombination of two oxygen atoms on Rh sites yielding molecular oxygen, has a marginal contribution.

- In Rh/CeO_2, once N_2O reduces a Rh site, this site can be reoxidized either by another N_2O molecule or by CeO_2 oxygen. In the latter case N_2O subsequently oxidizes the vacant site created on CeO_2.

- In Rh/CeO_2, the active sites for N_2O chemisorption and decomposition are not only located on Rh but also on CeO_2.

References

[1] F. Kapteijn, J. Rodríguez-Mirasol, J.A. Moulijn, Appl. Catal. B. 9 (1996) 25.
[2] J.C. Groen, J.C. Jansen, J.A. Moulijn, J. Pérez-Ramírez, J. Phys. Chem. B 108 (2004) 13062.
[3] V.A. Kondratenko, M.J. Baerns, Catal. 225 (2004) 37.
[4] E.V. Kondratenko, J. Pérez-Ramirez, Catal. Letters 91 (2003) 211.
[5] S. Tanaka, K. Yuzaki, S. Ito, H. Uetsuka, S. Kameoka, K. Kunimori, Catal. Today 63 (2000) 413.
[6] T.M. Miller, V.H. Grassian, J. Am. Chem. Soc. 117 (1995) 10969.
[7] H. Kobayashi, M. Kobayashi, Catal. Rev. Sci. Eng. 10 (1974) 139.
[8] A. Bueno-López, K. Krishna, B. van der Linden, G. Mul, J.A. Moulijn, M. Makkee, Catal. Today 121 (2007) 237.
[9] H. He, H.X. Dai, K.W. Wong, C.T. Au, Appl. Catal. A 251 (2003) 61.
[10] D. Martin, P. Kaur, D. Duprez, E. Gaigneaux, P. Ruiz, B. Delmon, Catal. Today 32 (1996) 329.
[11] Y. Madier, C. Descorme, A.M. Le Govic, D. Duprez, J. Phys. Chem. B 103 (1999) 10999.
[12] A. Holmgren, B. Andersson, J. Catal. 178 (1998) 14.
[13] A. Holmgren, D. Duprez, B. Andersson, J. Catal. 182 (1999) 441.
[14] J. Novakova, Catal. Rev. 4 (1970) 77.
[15] K. Klier, J. Nováková, P. Jíru, J. Catal. 2 (1963) 479.
[16] S. Parres-Esclapez, M.J. Illán-Gómez, C. Salinas-Martínez de Lecea, A. Bueno-López, Appl. Catal. B 96 (2010) 370.
[17] A. Bueno-López, I. Such-Basáñez, C. Salinas-Martínez de Lecea, J. Catal. 244 (2006) 102.
[18] J. Cunningham, F. Farrell, C. Gibson, J. McCarthy, Catal. Today 50 (1999) 429.
[19] A. Bueno-López, K. Krishna, M. Makkee, J.A. Moulijn, J. Catal. 230 (2005) 237.
[20] A. Bueno-López, K. Krishna, M. Makkee, J.A. Moulijn, Catal. Letters 99 (2005) 203.
[21] A. Holmgren, B. Andersson, D. Duprez, Appl. Catal. B 22 (1999) 215.
[22] A. Bueno-López, K. Krishna, M. Makkee, Appl. Catal. A 342 (2008) 144.

[23] J. Oi, A. Obuchi, G. R. Bamwenda, A. Ogata, H. Yagita, S. Kushiyama, K. Mizuno, Appl. Catal. B 12 (1997) 277.

[24] K.Yuzaki, T. Yarimizu, K. Aoyagi, S.-i. Ito, K. Kunimori, Catal. Today 45 (1998) 129.

[25] K. Jones, J.C. Bailar, H.J. Emeleus, R. Nyholm, A.F. Trotman-Dickenson, (Editors), Comprehensive Inorganic Chemistry, Pergamon Press, Oxford (1984) pp. 316-323.

[26] N.N. Greenwood, A. Eamshaw, Chemistry of the Elements, Pergamon Press, Oxford (1984).

[27] W.M. Kalback, C.M. Sliepcevich, Ind. Eng. Chem. Fundam. 17 (1978) 165.

[28] B.G. Reuben, J.W. Linnett, Trans. Faraday Soc. 55 (1959) 1543.

[29] O.R. Wulf, J. Am. Chem. Soc., 54 (1932) 833.

[30] J. Kaspar, P. Fornasiero, M. Graziani, Catal. Today 50 (1999) 285.

[31] J. Soria, A. Martinez-Arias, J.L. García-Fierro, J.C. Conesa, Vacuum 46 (1995) 1201.

[32] http://www.lasurface.com/ “acces September 2011”

[33] I. Cuauhtémoc, G. Del Angel, G. Torres, V. Bertin, Catal. Today 133 (2008) 588.

[34] A. Laachir, V. Perrichon, A. Badri, J. Lamotte, E. Catherine, J.C. Lavalley, J. El Fallal, L. Hilaire, F. le Normand, E. Quéméré, G.N. Sauvion, O. Touret, J. Chem. Soc. Faraday Trans. 87 (1991) 1601.

[35] S. Music, A. Saric, S. Popovic, M. Ivanda, J. Molec. Struct. 924–926 (2009) 221.

[36] V.V. Pushkarev, V.I. Kovalchuk, J.L. d’Itri, J. Phys. Chem. B 108 (2004) 5341.

[37] A. Nakajima, A. Yoshihara, M. Ishigame, Phys. Rev. B 50 (1994) 13297.

[38] K.I. Hadjiivanov, Catal. Rev. Sci. Eng. 42 (2000) 71.

[39] N. Oktar, J. Mitome, E.M. Holmgreen, U.S. Ozkan. J. Mol. Catal. A. 259 (2006) 171.

[40] Y. Wang, Z. Lei, B. Chen, Q. Guo, N. Liu, Appl. Surf. Sci. 256 (2010) 4042.

[41] S. Haq, A. Hodgson, Surf. Sci. 463 (2000) 1.

[42] J. Cunningham, J.N. Hickey, R. Cataluna, J.C. Conesa, J. Soria, A. Martinez-Arias. Stud. Surf. Sci. Catal. 101 (1996) 681.

CHAPTER V

$Rh/CeO_2(Pr)/\gamma$-Al_2O_3 catalysts for N_2O decomposition in presence of O_2, H_2O and NO

In this chapter, a supported catalyst composed by $Rh/CeO_2(Pr)$ active phase loaded on γ-Al_2O_3 particles was prepared and characterized. The catalytic decomposition of N_2O in the presence of O_2, H_2O and/or NOx was studied both in a flow reactor and by *in situ* DRIFTS-MS experiments. The N_2O decomposition capacity was found to be partially inhibited by O_2, H_2O and NO_x, being NO_x the strongest inhibitor and O_2 the weakest. The inhibiting effect of O_2 is attributed to its reversible chemisorption on catalytically active sites, while H_2O and NO_x are chemisorbed irreversibly. In spite of the inhibiting effect of O_2, H_2O and NO_x, the supported catalyst is able to decompose N_2O at 350-400 ºC. This temperature is suitable for N_2O decomposition in an industrial scale nitric acid production plant, without the need for additional energy input.

5.1. Introduction

As was commented in the chapter I, no specific legislation on N_2O emissions currently exists. However, stringent limits are expected for the near future [1,2] and for this reason it is important to develop technology for meeting those limits. A main source of N_2O is the industrial sector, to which 21% of the emissions can be accounted. The main industrial emissions of N_2O come from specific processes, such as adipic acid production for the manufacture of nylon and nitric acid production [1,3].

A large number of solid catalysts have been proposed for N_2O decomposition, including supported and unsupported metals, pure and mixed oxides, and zeolitic systems [2-7]. However, many of the proposed N_2O decomposition catalysts suffer inhibition by other gases present in the industrial streams together with N_2O, like O_2, H_2O, NO, SO_2, CO and CO_2. These gases can inhibit the catalysts due to reversible competitive adsorption, irreversible poisoning or because involve the catalyst in parallel reactions [1-10].

In the previous chapters, the results obtained with different powdered noble metal/CeO_2 catalysts were shown [11,12]. It was concluded that the catalyst reducibility plays an important role in N_2O decomposition, and a relationship between the low temperature reducibility by H_2 and the N_2O decomposition capacity of a set of Rh/CeO_2, Pd/CeO_2 and Pt/CeO_2 catalysts was found [11]. This relationship was rationalized by the observation that the slowest step of the N_2O decomposition redox mechanism with noble metal/CeO_2 catalysts seems to be the reduction of the actives sites upon N_2O chemisorption and oxidation of such active sites. For Rh catalysts, the CeO_2-supported samples presented higher activity than Rh/γ-Al_2O_3, and it was demonstrated that CeO_2, either pure or doped by Pr or La, is actively involved in the N_2O decomposition process [11], while CeO_2 participation is not so evident for the Pd and Pt catalysts. From all preceding studies on powdered active phases and simple gas streams (N_2O/He in most cases), it was concluded that the most active formulation, among those studied, is $Rh/CeO_2(Pr)$.

To use a catalyst in real gas streams, it is not enough to have good catalytic activity in N_2O/He, but the catalyst must also be active in the presence of inhibitors. In addition, powdered active phases are useful for basic research but not for most industrial applications, and to load active phases in an appropriate inert support is required. Recently, Rh/CeO_2(Pr) active phases were successfully supported on cordierite monoliths by impregnation and decomposition of the metal precursors [13]. Alumina carriers are also among the most used catalyst supports, including pure alumina particles, pellets or monoliths and also alumina coated-cordierite monoliths. This chapter is focussed on the use of alumina as support of the active phases.

Taking into account this background, advances in two aspects are required in order to facilitate the practical application of Rh/CeO_2(Pr) in industrial facilities: It is important to study the interaction of Rh/CeO_2(Pr) with alumina and it is necessary to evaluate the effect of typical inhibiting gases in the N_2O decomposition capacity. Therefore, the aim of this study was double: firstly, to support the active phase Rh/CeO_2(Pr) on alumina particles, and secondly, to study the physical-chemical properties of the supported catalysts and to test the catalytic decomposition of N_2O in the presence of O_2, H_2O and/or NO_x, both in a flow reactor and in an *in situ* DRIFTS cell. These gasses were selected because they are present, together with N_2O, in the end-of-pipe streams of nitric acid plants.

5.2. Experimental

5.2.1. Samples preparation

The samples used in this chapter were CeO_2(Pr)/γ-Al_2O_3, Rh/ CeO_2(Pr) and Rh/CeO_2(Pr)/γ-Al_2O_3. The detailed description of their preparation is reported in chapter II.

5.2.2. Characterization of samples

The samples were characterized by SEM, TEM, XRD, Raman spectroscopy, N_2 adsorption at -196 ºC, H_2-TPR and XPS. Information about these characterization techniques is reported in chapter II.

5.2.3. N_2O decomposition tests in a fixed bed flow reactor

N_2O decomposition tests were carried out in with the powdered ($Rh/CeO_2(Pr)$) and supported ($Rh/CeO_2(Pr)/\gamma$-Al_2O_3) catalysts, the experiments were performed using the among of catalyst necessary to have 100 mg of active phase ($Rh/CeO_2(Pr)$ in order to can compare the catalytic activity of both catalysts. The supported catalysts were carried out gas mixtures with one or more of the following components: 1000 ppm N_2O; 1000 ppm NO; 1, 2.2 or 5% O_2; 2.4 % H_2O; and balance He.

The gas composition was monitored by a Gas Chromatograph (HP 6890), and in some experiments, also with a Chemiluminescence NO_x analyzer (SIGNAL 400VM). The details related to the development of these experiments are included in chapter II of this thesis.

5.2.4. N_2O decomposition tests followed by in situ DRIFTS-MS

A FTIR spectrometer with a diffuse reflectance accessory was used for *in situ* DRIFTS experiments. A reaction cell with temperature and gas flow composition control was used. The gas composition was monitored during the experiments with a mass spectrometer (Pfeiffer Vacuum).

Before the DRIFTS measurements, the catalysts were treated *in situ* at 450 ºC under helium flow to remove any adsorbed species. Afterwards, the temperature was lowered to 30 ºC and the inert gas was replaced by a gas mixture of 1000 ppm N_2O/He, 1000 ppm N_2O/5% O_2/He, 1000 ppm N_2O/2.6% H_2O or 1000 ppm N_2O/1000 ppm NO/5% O_2. The temperature was raised in steps of 50 ºC until steady state conditions were reached in both the gas phase and catalyst surface composition (as indicated by the DRIFTS spectra). The background spectra were recorded at room temperature under He flow.

5.3. Results and discussion

5.3.1. Characterization results

SEM was used to get a rough idea about the structure of the γ-Al_2O_3 particles-supported $Rh/CeO_2(Pr)$ catalyst, and a representative SEM image is

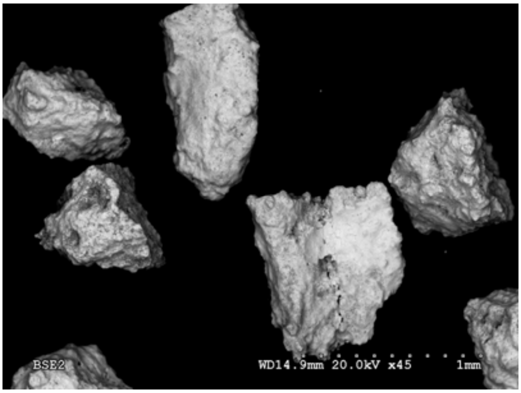

Figure 1. SEM image of the $Rh/CeO_2(Pr)/\gamma$-Al_2O_3 particles.

included in Figure 1. As expected, the size of the particles in Figure 1 is in the range 0.4-0.7 mm, and the appearance of the particles suggests that the alumina surface is covered by $Rh/CeO_2(Pr)$, which was confirmed by EDS analysis. EDS analysis was performed on different spots of the particles and the results obtained are summarized in Table 1.

Table 1. SEM-coupled EDS analysis on different spots of the $Rh/CeO_2(Pr)/\gamma$-Al_2O_3 particles (data in wt. %).

Element	spot 1	spot 2	spot 3	spot 4	spot 5	spot 6	Nominal composition[*]
Carbon	8.6	7.9	6.9	8.8	7.6	8.5	0.00
Aluminum	3.1	12.3	3.9	2.6	2.6	0.8	26.39
Rhodium	1.3	1.0	1.1	0.8	0.7	0.9	0.25
Cerium	52.6	38.1	54.7	48.2	51.8	56.9	36.52
Praseodymium	5.9	4.3	5.8	5.3	5.8	6.2	4.06
Oxygen	28.5	36.4	27.6	34.3	31.5	26.7	32.79

[*] Considering the composition 0.25 wt.% Rh + 0.485 wt.% $Ce_{0.9}Pr_{0.1}O_2$ + 0.485 wt.% Al_2O_3.

Most spots analysed present a cerium rich composition, with Ce/Pr ratios that are consistent with the composition $Ce_{0.9}Pr_{0.1}O_2$ and rhodium concentrations well above the nominal value. On the contrary, aluminium concentrations are lower than the nominal value. The high atomic weight elements (Ce, Pr and Rh) at the particles surface absorb X-rays from deeper inside the particles, where aluminium is located, confirming that alumina particles are coated with the $Rh/CeO_2(Pr)$ active phase. The presence of carbon in all EDS analyses must be attributed to adventitious carbon.

Figure 2 shows the XRD patterns of the $Rh/CeO_2(Pr)$ and $Rh/CeO_2(Pr)/\gamma$-Al_2O_3 catalysts. Both diffractograms show the characteristic reflections of

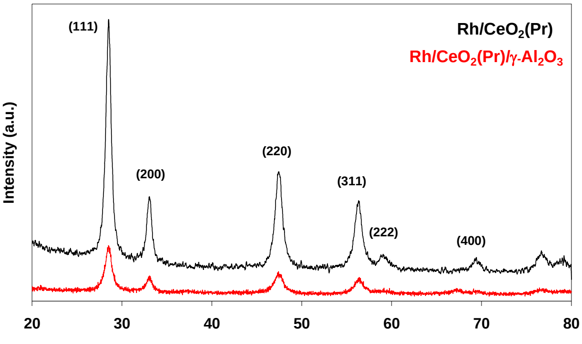

Figure 2. X-ray diffractograms of the supports Rh/CeO$_2$(Pr) and Rh/CeO$_2$(Pr)/γ-Al$_2$O$_3$.

solids with fluorite structure [11,14], and the lower intensity of the Rh/CeO$_2$(Pr)/γ-Al$_2$O$_3$ XRD peaks in comparison to those of Rh/CeO$_2$(Pr) is due to the dilution effect of γ-Al$_2$O$_3$. Rh$_2$O$_3$ peaks are not detected due to the low noble metal content and/or to its high dispersion. γ-Al$_2$O$_3$ peaks are neither detected in the Rh/CeO$_2$(Pr)/γ-Al$_2$O$_3$ diffractogram due to the low crystallinity of γ-Al$_2$O$_3$ in comparison to that of CeO$_2$, nor praseodymium oxide peaks [15]. Praseodymium could potentially form different oxides with composition of Pr$_2$O$_3$, PrO$_2$ and several intermediate phases (PrO$_{1.670}$, PrO$_{1.714}$, PrO$_{1.780}$, PrO$_{1.800}$, PrO$_{1.810}$, and PrO$_{1.833}$ [16–18]). Evidences of the formation of segregated phases of praseodymium are not detected in Figure 2.

The diffractograms of both catalysts (Rh/CeO$_2$(Pr) and Rh/CeO$_2$(Pr)/γ-Al$_2$O$_3$) are similar, with the fluorite peaks appearing exactly at the same angles. This indicates that the structures of the powder and γ-Al$_2$O$_3$-supported CeO$_2$(Pr) mixed oxide are not very different. This is confirmed by the lattice parameters of CeO$_2$(Pr) (included in Table 2), which are almost equal (~ 0.54 nm) for both the powder and supported catalysts.

Table 2. Catalysts characterization data: Rh average particle size by TEM, CeO$_2$(Pr) lattice constant and crystal size by XRD, BET by N$_2$ adsorption isotherms and percentage of Ce^{3+} by XPS.

Catalysts	Average particle size of Rh (nm)	CeO$_2$(Pr) lattice constant (nm)	CeO$_2$(Pr) crystal size (nm)	BET (m^2/g)	Ce^{3+} (at. %)
Rh/CeO$_2$(Pr)	1.2	0.5420	17	44	31
Rh/CeO$_2$(Pr)/γ-Al$_2$O$_3$	2.2	0.5390	13	62	22

The crystallite sizes of CeO_2(Pr) were determined from XRD patterns (with the Williamson-Hall's equation) and are included in Table 2. The size of the CeO_2(Pr) crystals on the powder catalyst (Rh/CeO_2(Pr); 17 nm) is slightly higher to that on the γ-Al_2O_3-supported particles (Rh/CeO_2(Pr)/γ-Al_2O_3; 13 nm), that is, the alumina particles seems to favour the formation of smaller crystals of CeO_2(Pr).

Table 2 also includes the BET surface area of the catalysts, determined from N_2 physisorption isotherms. The BET surface area of Rh/CeO_2(Pr)/γ-Al_2O_3 (62 m^2/g) is higher than that of Rh/CeO_2(Pr) (44 m^2/g), which is not surprising since the BET surface area of γ-Al_2O_3 (88 m^2/g) is much higher to that of CeO_2(Pr) (44 m^2/g). From these values, it can be concluded that rhodium does not affect the CeO_2 support surface area, since same areas are obtained with CeO_2(Pr) and Rh/CeO_2(Pr).

The geometrical area of CeO_2(Pr) in Rh/CeO_2(Pr)/γ-Al_2O_3 was calculated from the XRD-estimated crystal size (13 nm), assuming spherical shape of the CeO_2(Pr) crystals [19]. Considering the value obtained for this geometrical area (63 m^2/g), the pure γ-Al_2O_3 BET area and the weight percentage of each component, the expected area of Rh/CeO_2(Pr)/γ-Al_2O_3 would be 76 m^2/g if all γ-Al_2O_3 area were available for N_2 adsorption and 32 m^2/g if only CeO_2(Pr) were available, that is, if γ-Al_2O_3 surface were not accessible at all to N_2 because is blocked by CeO_2(Pr). The experimental value of Rh/CeO_2(Pr)/γ-Al_2O_3 (BET = 62 m^2/g) is in between both situations, which allows concluding that the alumina porosity is only partially accessible to N_2 because CeO_2(Pr) partially blocks the γ-Al_2O_3 porosity.

TEM was used to analyze the rhodium particle size in Rh/CeO_2(Pr) and Rh/CeO_2(Pr)/γ-Al_2O_3. Selected TEM images are shown in Figure 3, where the dark rhodium particles can be distinguished from the grey crystals of the support. The size of the rhodium particles was estimated from these types of images, and the average values are included in Table 2. The noble metal particle size distribution cannot be properly determined, since the number of noble metal particles identified is not high enough to achieve statistical significance. This is because, as can be observed in Figure 3, the noble metal particles are sometimes hardly distinguished when supported on CeO_2 and also because of the low loading (0.5 wt.%).

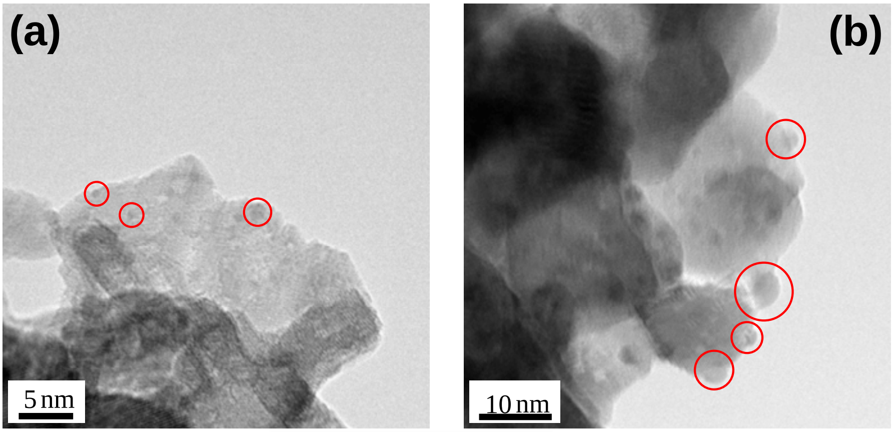

Figure 3. TEM images of (a) $Rh/CeO_2(Pr)$ and (b) $Rh/CeO_2(Pr)/\gamma$-Al_2O_3.

Nanometre rhodium particles are observed in both samples, but the size appears to be slightly smaller in the powdered catalyst ($Rh/CeO_2(Pr)$ average rhodium size 1.2 nm) than in the supported catalyst ($Rh/CeO_2(Pr)/\gamma$-Al_2O_3 average rhodium size 2.2 nm), indicating that the presence of γ-Al_2O_3 particles affect the rhodium distribution. A detailed TEM-EDS study of the $Rh/CeO_2(Pr)/\gamma$-Al_2O_3 sample was performed, and areas with Rh and γ-Al_2O_3 (without $CeO_2(Pr)$) were not found, indicating that rhodium is selectively attached to $CeO_2(Pr)$ and not to γ-Al_2O_3. This means that γ-Al_2O_3 is affecting the interaction of rhodium with $CeO_2(Pr)$, as will be evidenced by some other techniques afterwards.

The structure of the cerium oxide $CeO_2(Pr)$ was studied by Raman spectroscopy (Figure 4). Note that samples with γ-Al_2O_3 exhibit fluorescence and, as a result, the background signal in these samples is not constant. In spite of this limitation, the F_{2g} peak of CeO_2 is clearly distinguished in all spectra. The position of the F_{2g} peak (460 cm^{-1}) is exactly the same

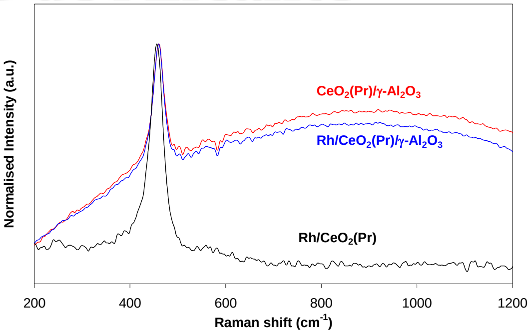

Figure 4. Raman spectra of the support $CeO_2(Pr)/\gamma$-Al_2O_3 and of the $Rh/CeO_2(Pr)$ and $Rh/CeO_2(Pr)/\gamma$-Al_2O_3 catalysts.

for all samples analyzed, and is lower to the typical value obtained with pure CeO_2 (465 cm^{-1}) [20-22]. The shift in the F_{2g} peak position in doped samples with regard to bare CeO_2 can be attributed to the introduction of other cations (Pr^{3+} in this case) into the CeO_2 lattice. The Raman spectra in Figure 4 indicates that Pr cations have been introduced into the CeO_2 structure, and that the Pr doping process is similar in the powder and γ-Al_2O_3-supported samples.

Figure 5 shows the reduction profiles of the different catalysts obtained in H_2-TPR experiments, providing information about the catalytic effect of rhodium in CeO_2(Pr) reduction and about the γ-Al_2O_3-CeO_2(Pr) interaction. The Rh/CeO_2(Pr) profile shows three peaks with maxima at 110, 275 and 810 ºC. The lowest-temperature peak is attributed to the noble metal reduction and/or to the noble metal-catalyzed surface reduction of CeO_2(Pr). The wide reduction peak centred at 275 ºC is also attributed to the surface reduction of CeO_2(Pr), but in this case corresponds to surface CeO_2 reduction which is not in tight contact with rhodium, that is, the reduction occurs with poor catalytic participation of the noble metal [23]. The third very smooth peak, at ca 810 ºC, is assigned to bulk reduction of CeO_2(Pr). The reduction of CeO_2(Pr) is quite different in the absence of rhodium (sample CeO_2(Pr)/γ-Al_2O_3). Here, the onset temperature is about 400 ºC, and the shift to higher temperature with regard to Rh/CeO_2(Pr) occurs because there is no catalytic effect of rhodium. Between 400 and 900 ºC, the CeO_2(Pr)/γ-Al_2O_3 profile shows a wide band, instead of single peaks, and this type of curve suggest high mobility of oxygen within the CeO_2(Pr) framework. In CeO_2 samples with high oxygen mobility, once the surface oxygen is depleted bulk oxygen comes out easily and the reduction continues with no distinction between surface and bulk reduction peaks. The samples with

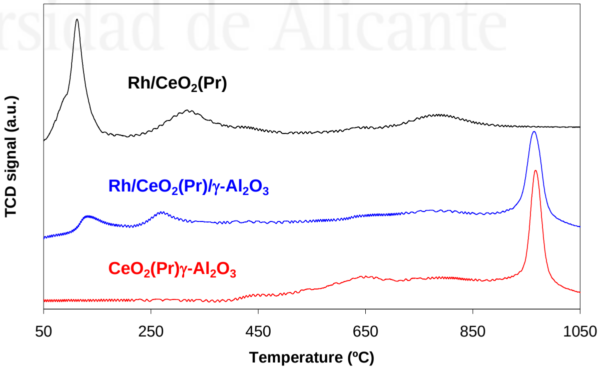

Figure 5. H_2-TPR characterisation of the support CeO_2(Pr)/γ-Al_2O_3 and of the Rh/CeO_2(Pr) and Rh/CeO_2(Pr)/γ-Al_2O_3 catalysts.

alumina show an intense peaks at 950 ºC, which has been assigned to the formation of a stable $CeAlO_3$ phase [24]. It is important to analyse in detail how the presence of γ-Al_2O_3 affects the interaction of Rh with CeO_2(Pr). The intensity of the lowest temperature peaks of Rh/CeO_2(Pr) is much higher than that of Rh/CeO_2(Pr)/γ-Al_2O_3, and is delayed from 110 ºC to 135 ºC in the latter catalyst. These changes point out that the presence of alumina hinders the formation of easily reduced Rh-Ce-Pr entities. This conclusion is consistent with the smaller particle size of rhodium in Rh/CeO_2(Pr) with regard to Rh/CeO_2(Pr)/γ-Al_2O_3, as observed by TEM (see values in Table 2), that is, the larger rhodium particles in Rh/CeO_2(Pr)/γ-Al_2O_3 are expected to interact to a less extent with CeO_2(Pr) than the smaller ones in Rh/CeO_2(Pr).

In previous studies (chapters III and IV) it was found that, for powdered noble metal/CeO_2 catalysts [11], a relationship between the temperature of the lowest temperature H_2-reduction peak and the catalyst activity in N_2O decomposition. This relationship was explained by assuming that the rate limiting step in the decomposition of N_2O over noble metal/CeO_2 catalysts is the reduction of actives sites upon N_2O chemisorption and oxidation. In combination with the H_2-TPR experiments, where it was observed that γ-Al_2O_3 hinders the formation of the most catalytically active surface Rh-Ce-Pr entities, could explain the higher catalytic activity of Rh/CeO_2(Pr) with regard to Rh/CeO_2(Pr)/γ-Al_2O_3. This will be discussed in more detail below.

XPS was used to obtain additional information about the interactions between rhodium, CeO_2(Pr) and γ-Al_2O_3. The Rh 3d photoelectron spectra obtained with Rh/CeO_2(Pr)/γ-Al_2O_3 and Rh/CeO_2(Pr) are shown in Figure 6. The Rh $3d_{5/2}$ binding energies typically are in the 307.0–307.7 eV range for Rh^0 and at 308.3–310.5 eV for Rh^{3+} [25-27]. The binding energies for Rh in the Rh/CeO_2(Pr) and Rh/CeO_2(Pr)/γ-Al_2O_3 catalysts are 309.4 and 308.6 eV, respectively, and both binding energies are consistent with the presence of Rh^{3+} cations. However, the lower value obtained with Rh/CeO_2(Pr)/γ-Al_2O_3 with regard to Rh/CeO_2(Pr) evidences that alumina hinders the interaction between rhodium and CeO_2(Pr). In other words, the average oxidation state of rhodium in the Rh/CeO_2(Pr)/γ-Al_2O_3 catalyst is lower than in Rh/CeO_2(Pr).

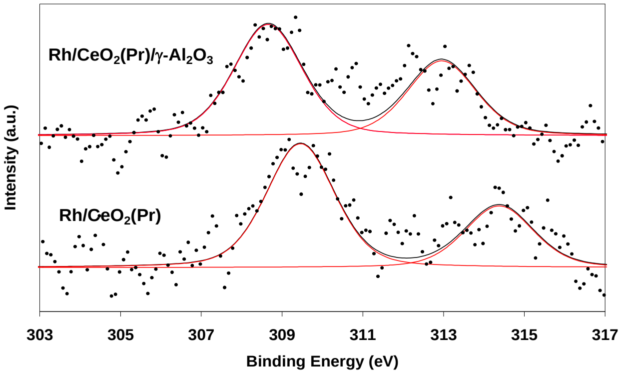

Figure 6. Rh 3d XPS spectra of the Rh/CeO$_2$(Pr) and Rh/CeO$_2$(Pr)/γ-Al$_2$O$_3$ catalysts.

The Ce 3d level was also analyzed and the spectra obtained with Rh/CeO$_2$(Pr) and Rh/CeO$_2$(Pr)/γ-Al$_2$O$_3$ are included in Figure 7. The degree of Ce reduction was calculated from these profiles (data in Table 2) as the ratio of the sum of the intensities of the u^0, u^1, v^0, and v^1 bands to the sum of the intensities of all the bands, following the method proposed elsewhere [28]. The percentages of Ce^{3+} (31% and 22% for Rh/CeO$_2$(Pr) and Rh/CeO$_2$(Pr)/γ-Al$_2$O$_3$, respectively) suggest that those cations on Rh/CeO$_2$(Pr) are more easily reduced than Ce^{4+} on Rh/CeO$_2$(Pr)/γ-Al$_2$O$_3$. The reduction of Ce^{4+} is expected to occur (at least partially) under the reduction conditions of the XPS measurements (an electron beam and high vacuum).

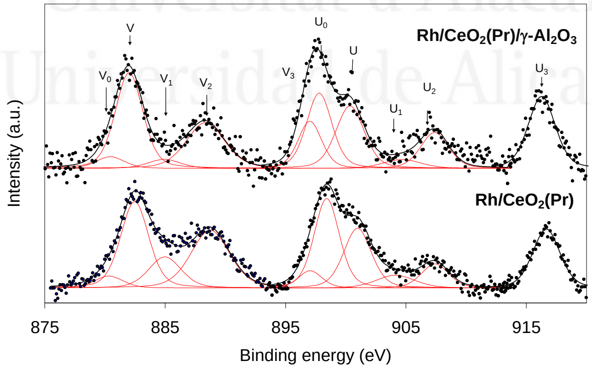

Figure 7. XPS characterization of the Rh/CeO$_2$(Pr) and Rh/CeO$_2$(Pr)/γ-Al$_2$O$_3$ catalysts: Ce 3d transition.

In summary, according to the characterization results discussed in this section, the $Rh/CeO_2(Pr)/\gamma\text{-}Al_2O_3$ catalyst consist of $\gamma\text{-}Al_2O_3$ particles, covered by the $Rh/CeO_2(Pr)$ active phase, with rhodium preferentially attached to $CeO_2(Pr)$ rather than to $\gamma\text{-}Al_2O_3$. The interaction between $CeO_2(Pr)$ and $\gamma\text{-}Al_2O_3$ affects the interaction of Rh with $CeO_2(Pr)$. Rhodium particles on $Rh/CeO_2(Pr)/\gamma\text{-}Al_2O_3$ are slightly larger than those in the counterpart alumina-free catalyst ($Rh/CeO_2(Pr)$), and the formation of easily reducible Rh-Ce-Pr entities is partially impeded by $\gamma\text{-}Al_2O_3$.

5.3.2. N_2O decomposition tests in a fixed bed reactor

The catalytic decomposition of N_2O on $Rh/CeO_2(Pr)$ and $Rh/CeO_2(Pr)/\gamma\text{-}Al_2O_3$ was compared using a gas stream of 1000 ppm N_2O/He. The N_2O conversion profiles and decomposition rates obtained are shown in Figure 8.

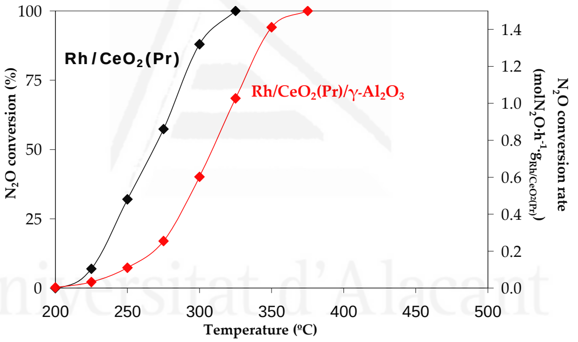

Figure 8. N_2O decomposition rates and conversion as a function of temperature in tests conducted with $Rh/CeO_2(Pr)$ and $Rh/CeO_2(Pr)/\gamma\text{-}Al_2O_3$ in 1000 ppm N_2O/He. (GHSV = 10000 h^{-1}, 100 mg of active phase ($Rh/CeO_2(Pr)$, total flow: 100 ml/min).

The onset temperature of N_2O decomposition is 225 ºC for both catalysts. Above this temperature, the activity of $Rh/CeO_2(Pr)/\gamma\text{-}Al_2O_3$ is lower than that of $Rh/CeO_2(Pr)$, with a 25-30 ºC shift in the position of the decomposition curve. As discussed in the previous section, this difference can be attributed to the interaction between $CeO_2(Pr)$ and $\gamma\text{-}Al_2O_3$, which in turns affects the interaction of Rh with $CeO_2(Pr)$ and lowers the catalytic activity. It was observed that rhodium particles on $Rh/CeO_2(Pr)/\gamma\text{-}Al_2O_3$ are slightly larger than those $Rh/CeO_2(Pr)$, and that the formation of easily reducible/highly active Rh-Ce-Pr entities is partially impeded by alumina.

The N_2O decomposition capacity of $Rh/CeO_2(Pr)/\gamma\text{-}Al_2O_3$ was also tested in the presence of O_2, H_2O and/or NO_x, and the conversion curves and reaction rates are plotted in Figure 9. The presence of O_2 in the gas stream together with N_2O (Figure 9a) has a minor effect in N_2O decomposition at 1 and 2.2% concentrations, while it slightly decreases the catalytic activity at higher concentration (5% O_2). As it will be discussed in detail in the next section, the catalytic decomposition of N_2O can be described as a redox process where the catalyst active sites are sequentially reduced and oxidized by N_2O (in Rh/CeO_2 systems not only rhodium but also CeO_2 sites are involved in this redox process, as described previously [12]), and the inhibiting effect of O_2 above a critical concentration can be attributed to the competition between N_2O and O_2 for the catalytically active sites.

The comparison between Figure 9a and 9b illustrates that the inhibiting effect of H_2O is stronger than that of O_2, since 2.2 % O_2 has almost no effect on N_2O conversion while 2.4% H_2O shifts the N_2O conversion curve to approximately 50 ºC higher temperatures with regard to the curve obtained with N_2O/He. The inhibiting effect of H_2O can be attributed to the chemisorption of H_2O and partial poisoning of catalyst sites. Details about this poisoning process have been studied by *in situ* DRIFTS-MS experiments and will be discussed in the next section.

Among the gases studied, NO is the strongest inhibitor (see Figure 9c) and, 1000 ppm of NO is enough to shift the N_2O decomposition profile to 100 ºC higher temperatures with regard to the curve on N_2O/He. The presence of O_2 and NO together with N_2O in the reactive gas mixture enhances the inhibiting effect of NO. In the presence of NO + O_2, the catalyst acelerates the oxidation of NO to NO_2 and this parallel reaction hinders N_2O decomposition. In addition NO, and to a higher extent NO_2, are chemisorbed on the catalyst surface blocking the catalytic sites. This deactivation mechanism has been also studied by in situ DRIFTS-MS and it will be discussed in the next section.

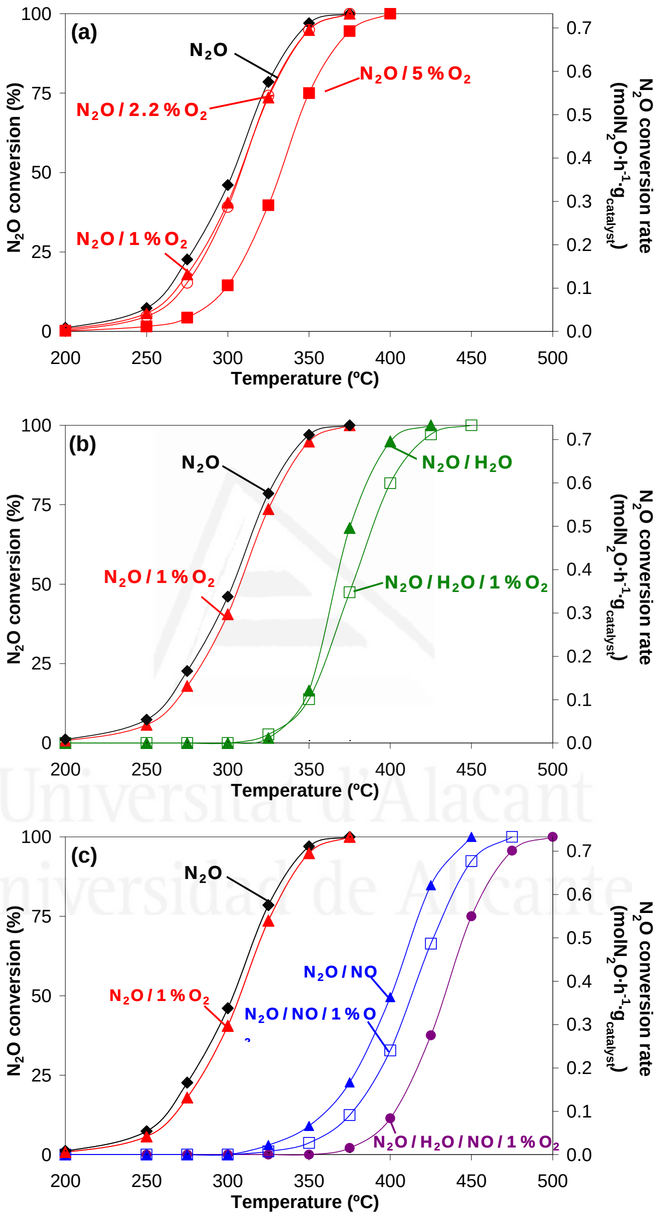

Figure 9. N_2O decomposition rates and conversion as a function of temperature in tests conducted with Rh/CeO_2(Pr)/γ-Al_2O_3. Effect of (a) 1, 2.2 or 5% O_2, (b) 2.4% H_2O and (c) 1000 ppm NO. (GHSV = 30000 h^{-1}, 1 g of catalyst, total flow: 500 ml/min).

In spite of the inhibiting effect of NO, O_2 and H_2O, the supported Rh/CeO_2(Pr)/γ-Al_2O_3 catalyst decomposes N_2O from around 350-400 ºC in the presence of all three gases, and the total conversion is reached at 500 ºC in the experimental conditions of these experiments (see Figure 9c). Therefore, in a nitric acid production plant, the catalytic decomposition of N_2O could be carried out after the expansion turbine, which is placed after the adsorption tower where the nitrogen oxides are adsorbed on water to yield nitric acid. In this position, the gas temperature reaches 400 ºC and the results obtained in this study suggest that the catalyst could be suitable for N_2O decomposition without additional energy input.

5.3.3. In situ DRIFTS-MS experiments

In order to understand the inhibiting effect of O_2, NO_x and H_2O in the catalytic decomposition of N_2O on Rh/CeO_2(Pr)/γ-Al_2O_3, *in situ* DRIFTS experiments were performed with different gas mixtures. The DRIFTS study was performed using two samples: CeO_2(Pr)/γ-Al_2O_3 and Rh/CeO_2(Pr)/γ-Al_2O_3. The Rh-free sample was used to analyse the interaction of the different gases with the modified support (CeO_2(Pr)/γ-Al_2O_3), for which no N_2O decomposition is expected to take place. The comparison of this Rh-free sample with Rh/CeO_2(Pr)/γ-Al_2O_3 gives valuable information about the effect of interactions in the N_2O decomposition process, which involve both rhodium and CeO_2 sites [12].

The MS results recorded simultaneously with the spectra during the DRIFTS-MS experiment on Rh/CeO_2(Pr)/γ-Al_2O_3 under 1000 ppm N_2O/He are shown in the Figure 10. The catalytic decomposition of N_2O in the DRIFTS cell occurs in the same range of temperatures that was observed in the fixed bed reactor (Figure 9). The only difference observed between the results obtained in the fixed bed reactor and in the DRIFTS cell is that the N_2O decomposition rate reached at a certain temperature is lower in the DRIFTS cell due to gas flow characteristics.

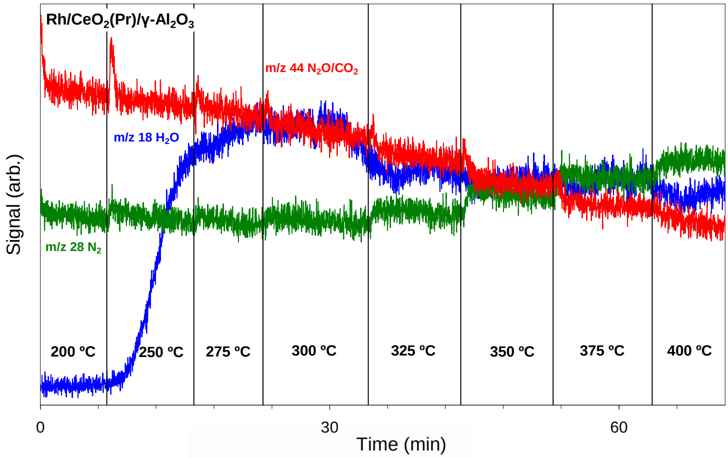

Figure 10. MS profiles measured during the DRIFTS-MS experiment performed with Rh/CeO$_2$(Pr)/γ-Al$_2$O$_3$ under 1000 ppmN$_2$O/He.

The infrared spectra obtained during these experiments are compiled in Figures 11 and 12. In general, there are three spectral regions that require special attention: i) 2400-2100 cm^{-1}, assigned to the N–N stretching frequency of adsorbed N$_2$ or N$_2$O [29-32], ii) below 1700 cm^{-1}, attributed to oxidized nitrogen species (nitrite, nitrate and/or nitro compounds) and iii) 3800-3600 cm^{-1} correspond to hydroxyl groups [33,34].

All spectra in Figures 11 and 12, regardless of the gas composition, temperature and sample, show bands in the range 2400-2100 cm^{-1}, attributed to chemisorbed N$_2$ and/or N$_2$O [29-32]. The formation of these bands in the Rh-free sample, where N$_2$O decomposition does not occur, suggests that they should be attributed to N$_2$O rather than to N$_2$. The formation of more than one band in this region can be attributed to the presence of different chemisorption sites on the catalyst surface, located on rhodium (if available), CeO$_2$(Pr) and/or γ-Al$_2$O$_3$. In addition, the CeO$_2$(Pr) surface is expected to be very heterogeneous, with several of the following species: cerium (3+ and 4+) and praseodymium cations, hydroxyl groups, oxygen vacancies, peroxide and superoxide groups, carbonates, etc. This heterogeneity could explain why there is not a single N$_2$O adsorption band in most spectra. For example, the formation of several bands in the range 2390-2100 cm^{-1} was observed in the chapter IV for pure CeO$_2$ in contact with N$_2$O while a single band at 2315 cm^{-1} for γ-Al$_2$O$_3$.

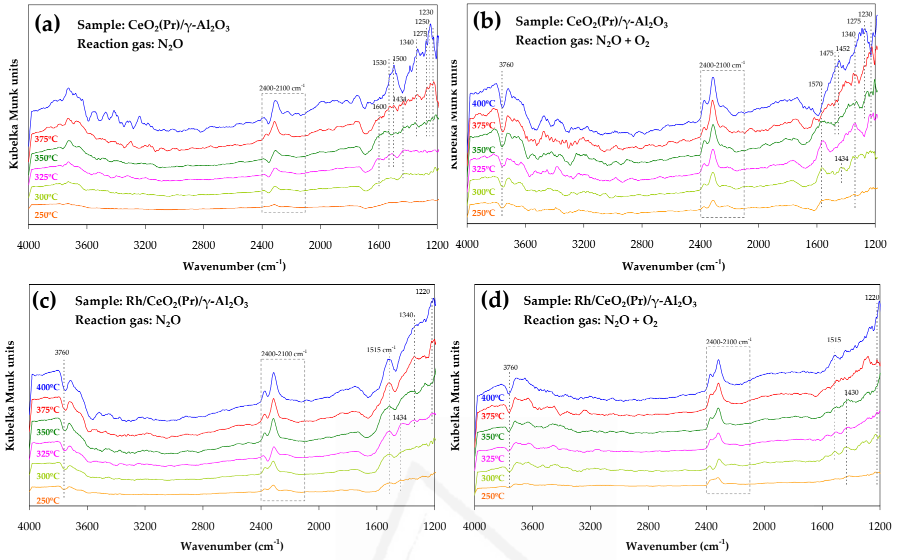

Figure 11. *In situ* DRIFT spectra of (a) $CeO_2(Pr)/\gamma$-Al_2O_3 under N_2O, (b) $CeO_2(Pr)/\gamma$-Al_2O_3 under $N_2O + O_2$, (c) $Rh/CeO_2(Pr)/\gamma$-Al_2O_3 under N_2O and (d) $Rh/CeO_2(Pr)/\gamma$-Al_2O_3 under $N_2O + O_2$.

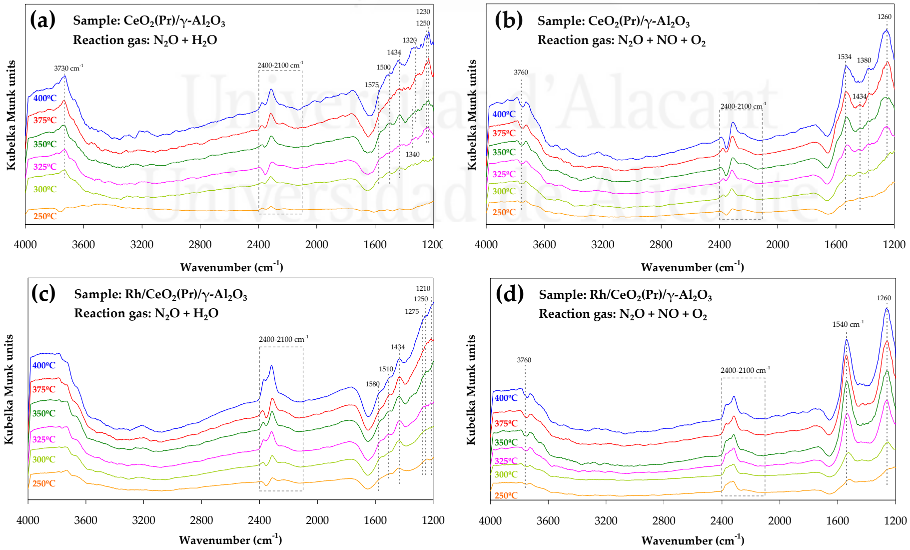

Figure 12. *In situ* DRIFT spectra of (a) $CeO_2(Pr)/\gamma$-Al_2O_3 under $N_2O + H_2O$, (b) $CeO_2(Pr)/\gamma$-Al_2O_3 under $N_2O + NO + O_2$, (c) $Rh/CeO_2(Pr)/\gamma$-Al_2O_3 under $N_2O + H_2O$ and (d) $Rh/CeO_2(Pr)/\gamma$-Al_2O_3 under $N_2O + NO + O_2$.

5.3.3.1. Experiments with N_2O and $N_2O + O_2$

The interaction of N_2O (Figure 11a) and $N_2O + O_2$ (Figure 11b) with the support CeO_2(Pr)/γ-Al_2O_3, apart from the N_2O bands, also produces bands below 1700 cm^{-1}. This confirms, in agreement with our previous study (chapter IV), that Pr-doped CeO_2 is able to oxidise the chemisorbed N_2O species to yield several oxidised surface species of nitrogen. With increasing temperature, monodentate nitrites appear first, with a typical peak at 1434 cm^{-1}, and nitrites are progressively oxidised to nitrates at higher temperatures, as indicated by the decrease in intensity of the 1434 cm^{-1} band at the expense of bands in the ranges 1530-1480 cm^{-1} and 1290-1250 cm^{-1} that progress together and correspond to monodentate nitrates [29]. The nitro band at about 1340 cm^{-1} and the formation of bidentate nitrates, with bands at around 1500 and 1275 cm^{-1}, are also observed at higher temperatures. Note that the stability of these nitrogen species increases with temperature. Nitro and nitrate compounds are more stable than nitrites, and they appear at higher temperatures. In the $N_2O + O_2$ mixture, these N_2O chemisorption and oxidation processes seem to involve hydroxyl groups, since a negative band at 3760 cm^{-1} grows with temperature due to hydroxyl group depletion.

In the chapter IV, it was concluded that the nitrite, nitro and nitrate compounds are not expected to be reaction intermediates in the N_2O decomposition mechanism, but rather are just spectator species that cover the catalyst surface. For this reason, the oxidised nitrogen species are detected during the N_2O decomposition reaction (Figures 10c and 10d, sample with rhodium) but also when there is no N_2O decomposition taking place (Figures 10a and 10b, sample without rhodium). In the absence of rhodium, the number of bands below 1700 cm^{-1} is higher than in the presence of noble metal, and the existing bands are, in general, more intense. This was also previously observed for a simple Rh/CeO_2 catalyst [12], where the oxidised nitrogen species appearing in this region were found to be spectator species. In the presence of rhodium, since N_2O decomposition is taking place, at least part of the surface sites of CeO_2(Pr) where nitrites, nitrates and/or nitro groups would be formed are not available because the surface of CeO_2 is involved in the N_2O decomposition process.

5.3.3.2. *Effect of H_2O*

Figures 12a and 12c show the DRIFT spectra recorded with $CeO_2(Pr)/\gamma\text{-}Al_2O_3$ and $Rh/CeO_2(Pr)/\gamma\text{-}Al_2O_3$, respectively, under $N_2O + H_2O$. In both spectra, the bands of N_2O chemisorbed are observed in the region 2400-2100 cm^{-1}, and differences are noticed below 1700 cm^{-1} and above 3600 cm^{-1} with regard to the H_2O-free gas streams (Figure 11).

The presence of H_2O in the gas mixture diminishes the formation of oxidised nitrogen surface species upon N_2O chemisorption, which is evidenced by the lower intensity of the bands below 1700 cm^{-1} in Figures 12a and 12c with regards to those in the counterpart spectra of Figure 11. This indicates that H_2O partially inhibits surface adsorption and oxidation sites where oxidised nitrogen species are formed. The behaviour of the hydroxyl bands in the region 3600-3800 cm^{-1} supports this hypothesis. In the absence of H_2O, hydroxyl groups are depleted during the progress of the N_2O decomposition reaction (Figure 11c), and a negative band appears at 3760 cm^{-1}. In the presence of H_2O (Figure 12a), the hydroxyl groups appear to be replenished by H_2O chemisorption on the available vacant sites and, as a result, the negative band at 3760 cm^{-1} is not observed in the spectra. The chemisorption of H_2O on the catalyst surface explains the decrease of the N_2O decomposition capacity observed in Figure 9.

5.3.3.3. *Effect of NOx*

The spectra obtained with $CeO_2(Pr)/\gamma\text{-}Al_2O_3$ and $Rh/CeO_2(Pr)/\gamma\text{-}Al_2O_3$ under $N_2O + NO + O_2$ are shown in Figures 12b and 12d, respectively. In both figures, bands in the range 2400-2100 cm^{-1}, due to the chemisorption of N_2O, a negative band at 3760 cm^{-1}, due to the depletion of hydroxyl groups and bands below 1700 cm^{-1}, attributed to oxidised nitrogen species are observed. In the absence of rhodium (Figure 12b; no N_2O decomposition) monodentate nitrites (band at 1434 cm^{-1}) appear to be formed first, and nitro (1380 cm^{-1}) and nitrate (1540 and 1260 cm^{-1}) species appear at higher temperature. As expected, the formation of oxidised nitrogen species is promoted in the presence of $NO + O_2$ in the gas stream, and the inhibiting effect of NO_x (see Figure 9c) is attributed to their chemisorption on surface sites of the catalyst.

5.3.3.4. Discussion about the inhibiting effect of O_2, H_2O and NOx

In chapter IV, a mechanistic study of the catalytic decomposition of N_2O over a Rh/CeO_2 catalyst was performed and the following mechanism was proposed:

$Rh\text{-}O + N_2O \rightarrow Rh^* + N_2 + O_2$ Step 1

$Rh^* + N_2O \rightarrow Rh^*\text{-}O + N_2$ Step 2

$2Rh^*\text{-}O \rightarrow 2Rh^* + O_2$ Step 3

$Rh^* + Ce^*\text{-}O \rightarrow Rh^*\text{-}O + Ce^*$ Step 4

$Ce^* + N_2O \rightarrow Ce^*\text{-}O + N_2$ Step 5

$2Ce^*\text{-}O \rightarrow 2Ce^* + O_2$ Step 6

$Rh^*\text{-}O + Ce^*\text{-}O \rightarrow Rh^* + Ce^* + O_2$ Step 7

where Rh*-O and Rh* are oxidised and reduced rhodium sites, respectively, and Ce*-O and Ce* are oxidised and reduced CeO_2 sites.

Taking into account this mechanism, the inhibiting effect of O_2 can be attributed to its reversible chemisorption on catalyst sites (reverse of Steps 3, 6 and 7).

In this mechanism, once a rhodium sites are reduced by N_2O (Step 1), the site can be reoxidised either by another N_2O molecule (Step 2) or by ceria oxygen (Step 4). In addition, in the presence of H_2O, the negative band appearing at 3760 cm^{-1} during N_2O decomposition suggests that the hydroxyl groups are involved in the mechanism, possibly as follows:

$2\ Ce\text{-}OH + N_2O \rightarrow 2\ Ce\text{-}^* + N_2 + H_2O + O_2$ Step 8

The depletion of hydroxyl groups will lead also to the formation of reduced cerium sites. This assumption is supported by the fact that the mass spectrometer detects water release during N_2O decomposition. The experiments performed in the presence of H_2O allow concluding that H_2O and N_2O compete for the vacant sites created on the surface of CeO_2 (Ce*), in other words, the Step 5 competes with Step 9:

$Ce\text{-}^* + Ce\text{-}O + H_2O \rightarrow 2Ce\text{-}OH$ Step 9

This step is proposed based on the fact that hydroxyl groups are created during N_2O decomposition in the presence of H_2O (Figure 12a). More specifically, it is observed that hydroxyl groups are not depleted in the presence of H_2O (Figure 12c) as is the case in the absence of H_2O (Figure 11c).

In the presence of NO_x, two mechanisms can be proposed for the inhibiting effect of these gases. The main one is the irreversible chemisorption of NO_x on the catalyst surface, which blocks catalytically active sites and hinders N_2O decomposition. Additionally, it was observed that the catalyst is able to oxidise NO to NO_2, and as a result, the active sites involved in this reaction are not available for N_2O decomposition. The Figure 13 shows the NO_2 profile during the N_2O decomposition tests in presence of NO, where it is observed that the production of NO_2 takes place in the same temperature range than N_2O decomposition.

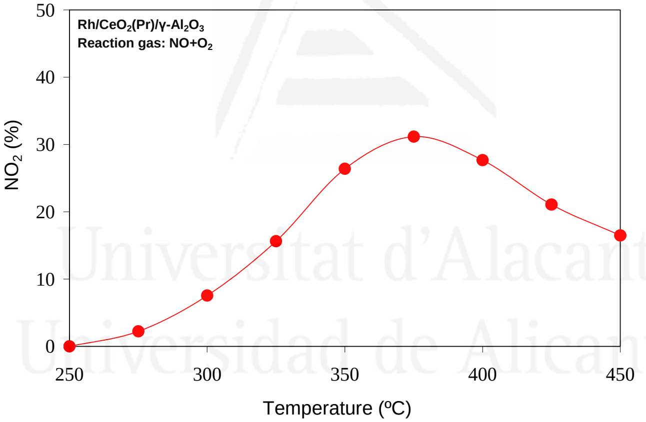

Figure 13. NO_2 profile measured by NOx chemiluminiscence analyzer during the N_2O decomposition tests in a fixed bed flow reactor performed with $Rh/CeO_2(Pr)/\gamma\text{-}Al_2O_3$ under 1000 ppmN_2O/He + 1000 ppmNO/He.

The sequence of steps 8 and 9 would explain why the inhibiting of H_2O is not as high as that of NO_x (compare Figures 9b and 9c). The competition between H_2O and N_2O for Ce* sites hinders N_2O decomposition, but the Ce-OH groups formed as a result of H_2O chemisorption are still suitable to decompose N_2O, but this is not the case of the surface species formed upon chemisorption of NO_x on the catalyst surface.

The results of the *in situ* DRIFTS experiments explain the shift in the N_2O decomposition onset temperature from about 200-250 ºC, for N_2O only streams, to 350-400 ºC in the presence of O_2, H_2O and NO_x. As was previously indicated, the catalytic N_2O decomposition over this catalyst could be used for N_2O decomposition in a nitric acid production plant after the expansion turbine, where the temperature reaches 400 ºC.

5.4. Conclusions

In this study, the active phase Rh/CeO_2(Pr) was supported on γ-Al_2O_3 particles and the supported catalyst was characterized and used for the catalytic decomposition of N_2O in the presence of O_2, H_2O and/or NO_x. The main conclusions extracted from this study are:

- The Rh/CeO_2(Pr)/γ-Al_2O_3 catalyst consist of γ-Al_2O_3 particles covered by the Rh/CeO_2(Pr) active phase, with rhodium preferentially attached to CeO_2(Pr) rather than to γ-Al_2O_3.

- The activity of the supported Rh/CeO_2(Pr)/γ-Al_2O_3 catalyst is slightly lower than that of the powdered active phase (Rh/CeO_2(Pr)). This difference is attributed to changes in the interaction between CeO_2(Pr) and γ-Al_2O_3, which in turns affects the interaction of Rh with CeO_2(Pr). Rh particles in Rh/CeO_2(Pr)/γ-Al_2O_3 are slightly larger than in Rh/CeO_2(Pr) and the formation of easily reducible, highly active Rh-Ce-Pr entities is partially impeded by alumina.

- The activity of the Rh/CeO_2(Pr)/γ-Al_2O_3 catalyst is partially inhibited in the presence of O_2, H_2O and NO_x. NO_x is the strongest inhibitor and O_2 the weakest. The inhibiting effect of O_2 is attributed to its reversible chemisorption on catalyst sites, while the effect of H_2O and NO_x is mainly related to irreversible chemisorption. The inhibiting effect of H_2O is lower than NO_x because the Ce-OH surface groups formed as a result of H_2O chemisorption are suitable for N_2O chemisorption and decomposition, while the surface nitrogen species created upon NO_x chemisorption are not.

- In spite of the inhibiting effect of NO_x, O_2 and H_2O, the $Rh/CeO_2(Pr)/\gamma\text{-}Al_2O_3$ catalyst can decompose N_2O above 350-400 ºC. Therefore, this catalysts could be used in a nitric acid production plant after the expansion turbine, where the gas stream temperatures is ~ 400 °C, avoiding an additional energy input.

References

[1] F. Kapteijn, J. Rodríguez-Mirasol, J.A. Moulijn, Appl. Catal. B 9 (1996) 25.
[2] J. Pérez-Ramírez, F. Kapteijn, K. Schöffel, J.A. Moulijn. Appl. Catal. B 44 (2003) 117.
[3] http://www.eea.europa.eu/pressroom/newsreleases/las-emisiones-de-gases-de-efecto-invernadero-se-redujeron-en-la-ue-en-2005." "acces September 2011"
[4] H.S. Gandhi, G.W. Graham, R. McCabe. J. Catal. 216 (2003) 433.
[5] G. Garrigós-Pastor, S. Parres-Escaplez, A. Bueno-López, M.J. Illán-Gómez, C. Salinas-Martínez de Lecea. Appl. Catal. A 354 (2009) 63.
[6] S.J. Lee, I.S. Ryu, B.M. Kim, S.H. Moon. Int. J. Greenhouse Gas Control 5 (2011) 167.
[7] A. Bueno-López, I. Such-Basáñez, C. Salinas-Martínez de Lecea. J. Catal. 244 (2006) 102.
[8] G. Centi, S. Perathoner, Z.S. Rak. Appl. Catal. B 41 (2003) 143.
[9] J. Oi, A. Obuchi, G. R. Bamwenda, A. Ogata, H. Yagita, S. Kushiyama, K. Mizuno. Appl. Catal. B 12 (1997) 277.
[10] S. Imamura, J. Tadani, Y. Saito, Y. Okamoto, H. Jindai, C. Kaito. Appl. Catal. A 201 (2000) 121.
[11] S. Parres-Esclapez, M.J. Illán-Gómez, C. Salinas-Martinez de Lecea, A. Bueno-López. Appl. Catal. B 96 (2010) 370.
[12] S. Parres-Esclapez, I. Such-Basañez, M.J. Illán-Gómez, C. Salinas-Martinez de Lecea, A. Bueno-López, J. Catal. 276 (2010) 390.
[13] V. Rico-Pérez, S. Parres-Esclapez, M.J. Illán-Gómez, C. Salinas-Martínez de Lecea, A. Bueno-López. Appl. Catal. B. 107 (2011) 18.
[14] D. Terribile, A. Trovarelli, J. Llorca, C. de Leitenburg, G. Dolcetti, Catal. Today 43 (1998) 79.
[15] J.R. Mcbride, K.C. Hass, B.D. Poindexter, W.H. Weber, J. Appl. Phys. 76 (1994) 2435.
[16] R. Lo Nigro, R.G. Toro, G. Malandrino et al (2003) Adv Mater 15:1071

[17] Ma L, Chen WX, Zhao J, Zheng YF (2007) J Crystal Growth 303:590

[18] Hussein GAM, Balboul BAA, Warith MAA et al (2001) Thermochim Acta 369:22

[19] C. Bueno-Ferrer, S. Parres-Esclapez, D. Lozano-Castelló, A. Bueno-López. J. Rare Earths 28 (2010) 647.

[20] J.E. Spanier, R.D. Robinson, F. Zheng, S.W. Chan, I.P. Herman, Phys. Rev. B 64 (2001) 2454071.

[21] F. Zhang, S.W. Chan, J.E. Spanier, E. Apak, Q. Jin, R.D. Robinson, I.P. Herman, Appl. Phys. Lett. 80 (2002) 127.

[22] S. Rossignol, C. Descorme, C. Kappenstein, D. Duprez, J. Mater. Chem. 11 (2001) 2587.

[23] J. Silvestre-Albero, F. Rodríguez-Reinoso, A. Sepúlveda-Escribano, J. Catal. 210 (2002) 127.

[24] M. Fernández-García, A. Martínez-Arias, A. Iglesias-Juez, C. Belver, A. B. Hungría, J.C. Conesa, J. Soria, J. Catal. 194 (2000) 385.

[25] http://www.lasurface.com/. "acces September 2011"

[26] X.D. Wu, L.H. Xu, D. Weng, Appl. Surf. Sci. 221 (2004) 375.

[27] J. Soria, A. Martínez-Arias, J.L.G. Fierro, J.C. Conesa, Vacuum 46 (1995) 1201.

[28] A. Laachir, V. Perrichon, A. Badri, J. Lamotte, E. Catherine, J.C. Lavalley, J. El Fallal, L. Hilaire, F. le Normand, E. Quéméré, G.N. Sauvion, O. Touret, J. Chem. Soc. Faraday Trans. 87 (1991) 1601.

[29] K.I. Hadjiivanov, Catal. Rev. Sci. Eng. 42 (2000) 71.

[30] N. Oktar, J. Mitome, E.M. Holmgreen, U.S. Ozkan. J. Mol. Catal. A. 259 (2006) 171.

[31] Y. Wang, Z. Lei, B. Chen, Q. Guo, N. Liu, Appl. Surf. Sci. 256 (2010) 4042.

[32] S. Haq, A. Hodgson, Surf. Sci. 463 (2000) 1.

[33] P. Djinović, J. Batista, A. Pintar, Catal. Today 147 (2009) 191.

[34] P.V. Menacherry, G.L. Haller, Catal. Letters, 44 (1997) 135.

CHAPTER VI

N_2O decomposition in a realistic nitric acid plant gas stream

A $Rh/CeO_2(Pr)/\gamma\text{-}Al_2O_3$ catalyst was tested for N_2O decomposition in a nitric acid plant. The catalyst is active enough for 100% N_2O removal at the nitric acid plant reaction conditions and maintains catalytic activity after 40 hours of operation. The characterization of the fresh and used catalysts by different techniques revealed that the main physico-chemical properties of the catalyst do not change during the N_2O decomposition experiments.

6.1. Introduction

In 2007, the European Council drafted new regulations regarding the emission of greenhouse gases within the European Union. According to the draft, the emission of greenhouse gases in Europe must be decreased by 30% with respect to 1990 levels. For the most developed countries a decrease of 80 % was proposed for 2050 [1].

The main chemical industries that emit nitrous oxide to the atmosphere are nitric acid and adipic acid manufacturing plants [2]. The current research is focussed on the abatement of nitrous oxide from nitric acid production facilities.

Two potential approaches have been proposed to diminish N_2O emissions from nitric acid plants [3]. One approach enhances NH_3 oxidation and decreases N_2O formation. Unfortunately, the modifications needed for this approach cannot be easily implemented in most of the already existing plants. The other approach focuses on removing N_2O by catalytic decomposition or reduction.

For catalytic reduction, a reductant gas such as NH_3, CO, H_2 or hydrocarbons, has to be added to the N_2O-containing gas stream. This gas stream is then converted over a selective catalyst which facilitates the N_2O reduction into N_2.

Catalytic decomposition is a generally more convenient N_2O depletion method, because it does not require the addition of reductant gases and has no impact to the overall production process.

The catalytic decomposition of N_2O could be carried out in three different locations of a nitric acid production plant (see Figure 1) [3]. The first option is just before the gas is delivered to the atmosphere. However, the gas temperature at this point is too low for the available catalysts.

The second option is to place the N_2O decomposition catalyst after the Pt-Rh gauze used for NH_3 oxidation, where the stream temperature reaches 800-900 ºC. However, this method requires a highly stable catalyst to operate under such severe conditions. Furthermore, the catalyst should have high selectivity to N_2O decomposition, without NOx decomposition, which would affect the yield of the process.

The third possible position for the N_2O decomposition catalyst is downstream from the expansion turbine located after the adsorption tower, where the nitrogen oxides react with water to yield nitric acid. The gas temperature at this position reaches 400 ºC, and N_2O must be decomposed in the presence of H_2O, NOx and O_2 in the stream. Therefore, the decomposition catalyst must be able to operate at mild temperature and in the presence of the mentioned inhibiting compounds. Most of the N_2O decomposition catalysts proposed for N_2O decomposition around 400 ºC are strongly affected by O_2 and H_2O and poisoned by NOx [2-10]. Consequently, suitable catalysts to operate in these described conditions are required.

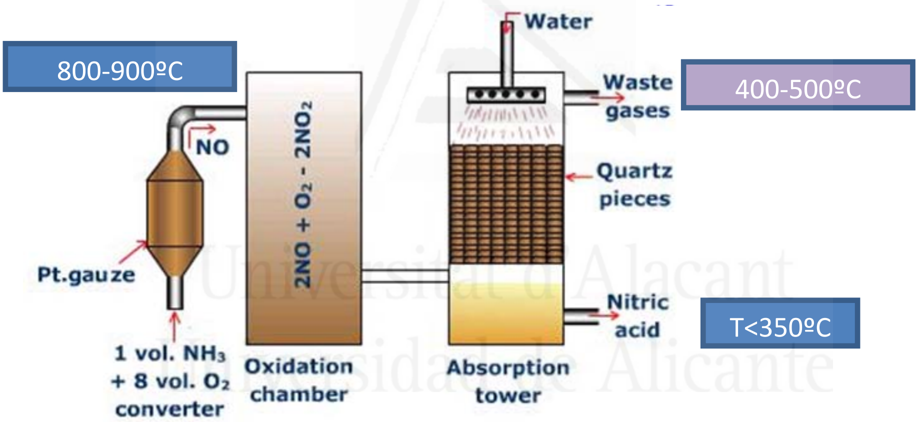

Figure 1. Scheme of a nitric acid production plant.

A high catalytic activity for N_2O decomposition at mild temperature was previously reported for Rh/cerium oxide formulations, and the promoting role of cerium oxide in the catalytic activity of rhodium was demonstrated in chapters III and IV. An improved performance was observed for cerium oxide support in comparison to an inert carrier like alumina, and among the cerium oxide supports tested, the Ce-Pr mixed oxides outperformed the behaviour of bare or La-doped ceria.

The decomposition of N_2O assisted by a $Rh/CeO_2(Pr)/\gamma\text{-}Al_2O_3$ catalyst was previously studied at the laboratory scale using H_2O, NOx and/or O_2 containing gas streams (chapter V). The promising results that were obtained suggest that this catalyst is a potential candidate for N_2O decomposition at mild temperature under realistic nitric acid plant conditions.

Thus, the goal of the study described in this chapter is to test a $Rh/CeO_2(Pr)/\gamma\text{-}Al_2O_3$ catalyst for N_2O decomposition in a nitric acid plant gas stream, after the expansion turbine. The catalyst was characterized before and after the catalytic tests in order to identify potential changes in the physico-chemical properties and how these changes affect catalyst performance.

6.2. Experimental

6.2.1. Catalyst preparation

The detailed description of the catalyst preparation was reported in chapter II.

6.2.2. N_2O decomposition tests at pilot plant scale

Two types of experiments were performed:

- TPR catalytic tests consisting of heating the catalyst from room temperature to about 450 ºC at 3 ºC/min under the reaction stream.

- Isothermal reaction, where the catalyst is kept at constant temperature for a certain time.

6.2.3. Catalyst characterization

The catalyst was characterized before and after the catalytic tests by different techniques. Additional information on the characterization techniques is reported in chapter II. It is important to mention that the same catalyst sample was used for all the catalytic tests. Consequently, the catalyst was operated under reaction conditions for about 40 (non-consecutive) hours.

During the tests, the catalyst suffered nine heating (till 450 ºC) and cooling steps and was kept at 350 ºC for different periods of time.

6.3. Results and discussion

6.3.1. TPR catalytic tests

Figure 2 includes the N_2O decomposition profiles obtained during three representative TPR experiments. The first TPR experiment was performed with fresh catalyst and using a model gas stream with 1825 ppm N_2O/N_2. All further cycles were carried out with the same catalyst sample using realistic gas stream (988 ppm N_2O + 800 ppm NOx + 0.7 % H_2O + 2.1 % O_2).

The catalytic decomposition of N_2O in the model gas flow takes place above 200 ºC (1st run, Figure 2), in close agreement with the previously observed behaviour of the Rh/CeO_2(Pr) γ-Al_2O_3 catalyst in laboratory experiments showed in the chapter V. The catalytic decomposition of N_2O is shifted to higher temperature when the experiment were performed using the realistic gas stream. Taking into account our previous study about the effect of NO_x, H_2O and O_2, this delay can be mainly attributed to the inhibiting effect of NO_x and H_2O. O_2 was observed to have a minor effect in the catalytic activity of Rh/CeO_2(Pr)/γ-Al_2O_3 for O_2 concentrations around 1-2%, and the activity decreased only slightly at higher concentration (5% O_2).

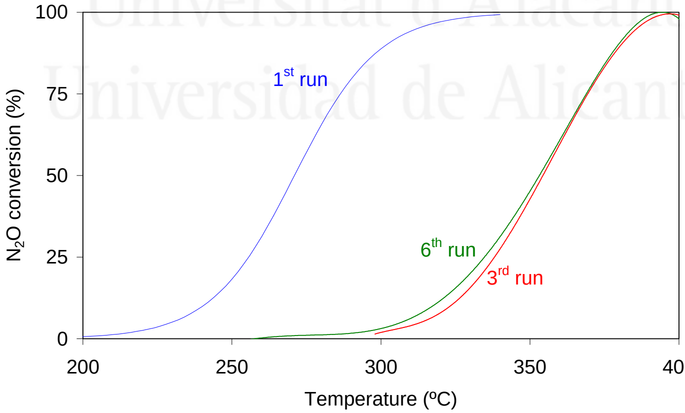

Figure 2. TPR profiles for Rh/CeO_2(Pr)/γ-Al_2O_3 catalyzed N_2O decomposition in three experiments. Fresh catalyst was used for the 1st run; GHSV = 15000 h^{-1}; gas composition 1st run = model gas with 1825 ppm N_2O in N_2; gas composition 3rd and 6th runs = realistic gas with 988 ppm N_2O + 800 ppm NOx + 0.7 % H_2O + 2.1 % O_2.

The N_2O decomposition does not change during the TPR cycles carried out using the realistic gas stream, and as an examples, the profiles obtained during the 3rd and 6th TPR experiments are shown in Figure 2. Those evidences the high stability of the Rh/CeO_2(Pr) catalyst under the reaction conditions used.

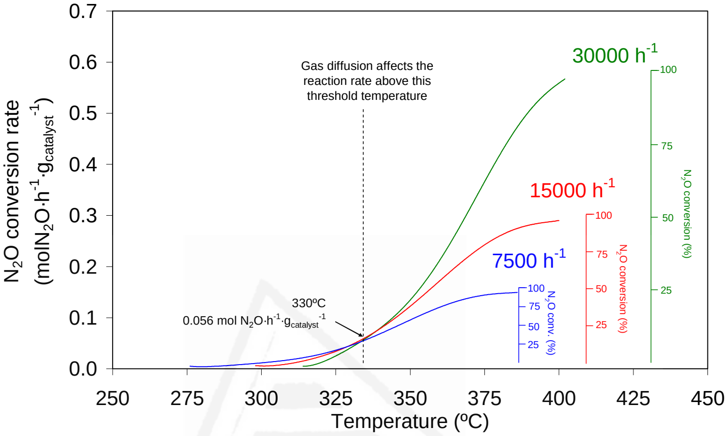

Figure 3. Effect of GHSV in the Rh/$Ce_{0.9}Pr_{0.1}O_2$/γ-Al_2O_3 catalyzed N_2O decomposition in TPR experiments (gas composition = 1007 ppm N_2O + 844 ppm NOx + 0.7 % H_2O + 2.1 % O_2).

Additionally, the effect of the GHSV on the catalytic decomposition of N_2O was analyzed using the realistic gas stream. TPR experiments using different gas flows were performed (7500, 15000 y 30000 h^{-1}). The results of these experiments are included in Figure 3. N_2O decomposition starts around 300 ºC, in accordance with the results of Figure 2. The catalytic decomposition of N_2O takes place under kinetic control of the reaction rate until 330 ºC and above this temperature, the higher the GHSV the higher the N_2O decomposition rate, indicating that the mass transfer limitation affects the reaction rate.

In spite of the contribution of gas diffusion, the Rh/CeO_2(Pr)/γ-Al_2O_3 catalyst is able to accelerate N_2O decomposition up to 100 % conversion at 400 ºC or lower temperature for all the GHSV tested. These results demonstrate that the Rh/CeO_2(Pr)/γ-Al_2O_3 catalyst is an suitable catalyst for the removal of N_2O in nitric acid plants.

6.3.2. Isothermal catalytic tests

In order to analyse the stability of the catalyst at steady state conditions, isothermal experiments were conducted at 350 ºC with realistic gas stream and using three different GHSV (3800, 7500 and 15000 h^{-1}). Two gas compositions were tested: 1000 ppm N_2O + 734 ppm NOx + 1.0 % H_2O + 2.0 %O_2 (Figure 4a) and 1000 ppm N_2O + 1200 ppm NOx + 1.3 % H_2O + 1.5 % O_2 (Figure 4b).

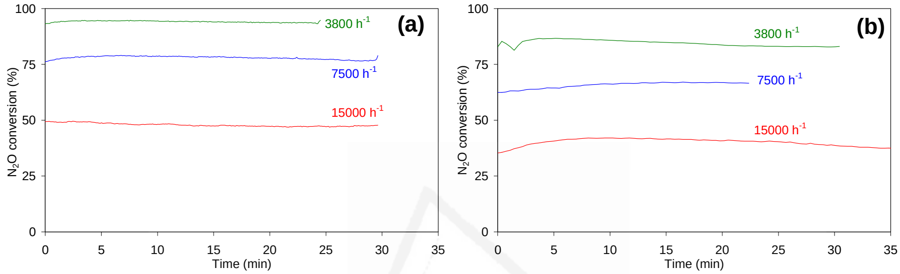

Figure 4. N_2O decomposition isothermal tests performed at 350 ºC with the Rh/CeO_2/(Pr)/γ-Al_2O_3 catalysts and using realistic gas streams of compositions: (a) 1000 ppm N_2O + 734 ppm NOx + 1.0 % H_2O + 2.0 %O_2 and (b) 1000 ppm N_2O + 1200 ppm NOx + 1.3 % H_2O + 1.5 % O_2.

The isothermal reactions were run for 30 minutes. In all cases, the N_2O decomposition level was constant during this period of time (see Figure 4), regardless the GHSV and the gas composition tested. These results confirm the stability of the Rh/CeO_2(Pr)/γ-Al_2O_3 catalyst.

As expected, N_2O conversion is higher at low GHSV. The inhibiting effect of NO_x and H_2O also affect the performance of the Rh/CeO_2(Pr)/γ-Al_2O_3 catalyst during the isothermal experiments. For a particular GHSV, the N_2O decomposition level reached in Figure 4a is higher than that reached in Figure 4b, due to the lower concentration of NO_x (734 vs 1200 ppm) and H_2O (1.0 vs 1.3 %) in the former gas stream. Note that the O_2 concentration is higher for Figure 4a experiments than for Figure 4b experiments (2.1 vs 1.5 %), confirming that the effect of O_2 in Rh/CeO_2(Pr)/γ-Al_2O_3 activity is minor in comparison with the effect of NOx and H_2O.

As a summary, the Rh/CeO_2(Pr) catalyst is active enough to ensure 100% N_2O removal in the real reaction conditions of a nitric acid plant. In addition, as it was mentioned in the experimental section, the Rh/CeO_2(Pr)/γ-Al_2O_3 catalyst was used to perform all the catalytic tests with the same parcel of catalyst, and the results of this section reveal that the catalyst does not suffer any appreciable deactivation with time.

6.3.3. Characterization of the fresh and used catalyst

The fresh and used Rh/CeO_2(Pr)/γ-Al_2O_3 catalyst was characterized by different techniques, and the obtained results are presented and discussed in this section. The characterization of the fresh catalyst was described in detail in the chapter V, and in this section, the discussion is mainly focussed on the potential changes suffered during the catalytic tests performed under real gas streams.

Figure 5 compiles the XRD patterns of the fresh and used Rh/CeO_2(Pr)/γ-Al_2O_3 catalyst. Both diffractograms show the characteristic peaks of fluorite, which is the crystalline structure of pure and many doped cerium oxides [11-13]. Peaks of rhodium species are not observed in Figure 5, due to the low concentration and high dispersion of the noble metal on the cerium oxide surface [14-16]. γ-Al_2O_3 peaks were not observed, most likely because of the low crystallinity of this aluminium oxide phase in comparison to the high crystallinity of the cerium oxide fluorite phase. Peaks of segregated praseodymium phases were also absent.

The most interesting conclusion from Figure 5 is that the diffractograms of the fresh and used catalyst are identical, that is, structural changes are not detected by XRD before and after the catalytic tests. The crystal size of the Pr-doped cerium oxide particles was estimated from the X-Ray diffractograms by using the Scherrer and Williamson-Hall equations [15], and the obtained sizes are compiled in Table 1. The similar crystal sizes determined for the fresh and used catalyst demonstrate the catalyst stability under reaction

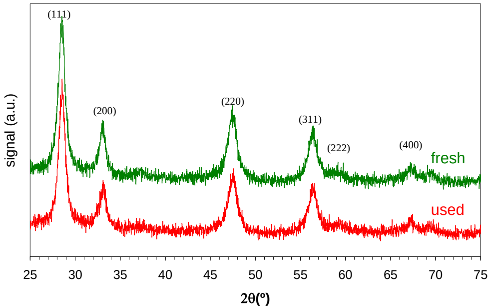

Figure 5. X-ray diffractograms of the fresh and used Rh/CeO_2/(Pr)/γAl_2O_3 catalyst.

conditions. Note that the sizes estimated with the Williamson-Hall's equation are slightly longer to those obtained with the Scherrer's equation, because the latter approach does not takes into account the contribution of the lattice defects, introduced by Pr doping, to XRD peaks broadening while the former does [17].

Table 1. Crystallytes size of $Ce_{0.9}Pr_{0.1}O_2$ and BET surface area of the fresh and used catalyst.

Rh/CeO$_2$/(Pr)/γ-Al$_2$O$_3$ Catalyst	Crystallytes size of CeO$_2$/(Pr)/γ-Al$_2$O$_3$ by Scherrer (nm)	Crystallytes size of CeO$_2$/(Pr)/γ-Al$_2$O$_3$ by Williamson-Hall (nm)	BET area of the catalyst (m^2/g)
Fresh	11	13	62
Used	11	14	57

The BET surface areas of the fresh and used catalyst have been also included in Table 1 and, also, similar surface areas have been obtained before and after the catalytic tests (62-57 m^2/g).

Raman spectra of the fresh and used Rh/CeO$_2$(Pr)/γ-Al$_2$O$_3$ catalyst were recorded (Figure 6). Both spectra are similar, with a non-constant background level due to γ-Al$_2$O$_3$ and a prominent peak at 460 cm^{-1} attributed to the oxygen breathing into the fluorite lattice of cerium oxide. Note that the typical position of the fluorite peak for a pure ceria sample is about 465 cm^{-1}, and the shift to lower values observed in Figure 6 can be attributed to Pr introduction into the ceria framework. N$_2$ adsorption and Raman characterization further illustrate the stability of the catalyst during the catalytic tests performed.

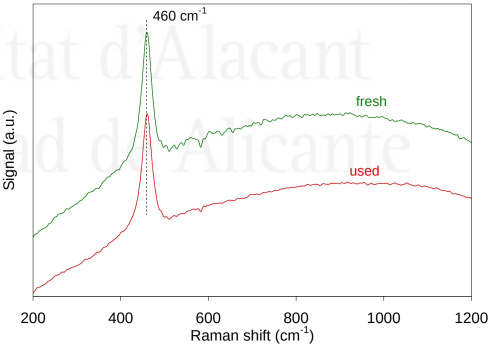

Figure 6. Raman spectra of the fresh and used Rh/CeO$_2$/(Pr)/γ-Al$_2$O$_3$ catalyst.

The structural characterization of the Rh/CeO$_2$(Pr)/γ-Al$_2$O$_3$ catalyst was completed by TEM. Figure 7 shows the bright field TEM images of the fresh and used catalyst. Dark rhodium particles are identified in both images. The average rhodium sizes are included in Table 2 together with the smallest and largest rhodium particle identified, in order to obtain information about the dispersion of sizes. Note that the number of rhodium particles measured (30-50 particles) is not high enough from a statistical point of view, therefore, it cannot be obtained a significance particle size distribution curve.

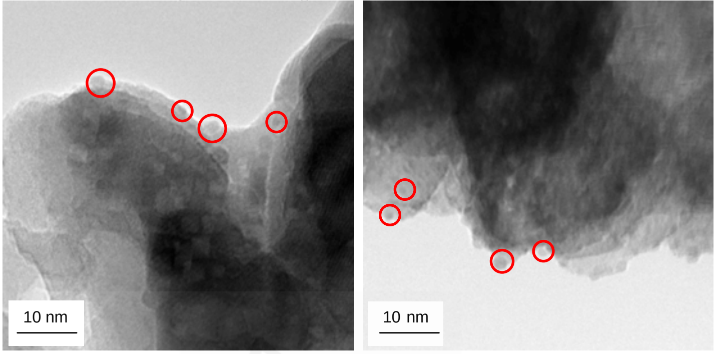

Figure 7. TEM pictures of the fresh (a) and used (b) Rh/CeO_2/(Pr)/γ-Al_2O_3 catalyst.

The mean rhodium particles size observed by TEM is approximately 2 nm, and the average dispersion is high, since the size of most particles observed is lower than 3.6 nm. The differences in rhodium particle size between the fresh and used catalysts are minor, indicating that the rhodium particles do not suffer a significant sintering during the catalytic tests.

Table 2. TEM characterization of the particle size of rhodium in the fresh and used catalyst.

Rh/CeO_2/(Pr)/γ-Al_2O_3 catalyst	Mean size (nm)	Smallest particle (nm)	Largest particle (nm)
Fresh	2.2	1.0	3.3
Used	1.8	1.0	3.6

H_2-TPR experiments were performed with the fresh and used catalyst in order to identify potential changes in the reducibility of the catalyst during the N_2O decomposition tests. The curves obtained for the fresh and used catalyst (shown in Figure 8) are similar:

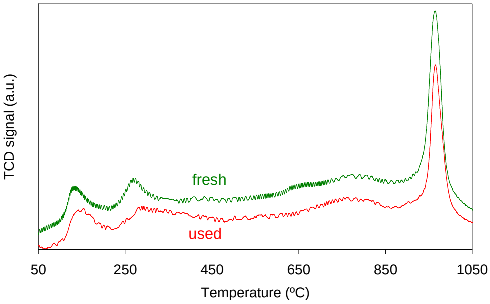

Figure 8. H_2-TPR characterisation of the fresh and used Rh/CeO_2/(Pr)/γ-Al_2O_3 catalyst.

Two peaks appear at 135 and 275 ºC, attributed to the reduction of cations at the surface of the cerium oxide particles. The reduction at 135 ºC, attributed to Rh^{3+}, Ce^{4+} and Pr^{4+}, has been proposed to occur at the rhodium-cerium oxide interface while the Ce^{4+} and Pr^{4+} reduction at 275 ºC is attributed to cations which are not in intimate contact with the noble metal [18]. The bulk reduction of the Ce-Pr mixed oxide takes place below 850 ºC, and the intense peak at 950 ºC has been assigned to the reduction of Ce-Al-O phases created by ceria and alumina reaction [19].

Finally, XPS spectra of the fresh and used catalyst were recorded, and the energy regions corresponding to the Rh 3d electronic transition is shown in Figure 9. Rh^{3+} species usually show binding energies in the range 308.3-310.5 eV for the Rh 3d5/2 electronic transition, while Rh^0 appears at 307.0-307.7 eV [19,20]. It is important to underline that, in previous studies, it was concluded that the cationic species of rhodium supported on ceria are more active for N_2O decomposition than Rh^0 supported on ceria and that such cationic rhodium species can be partially reduced to Rh^0 under N_2O decomposition conditions [14-16]. The curves included in Figure 9 show a binding energy of 308.6 eV for the Rh 3d5/2 electronic transition both for the fresh and used catalyst, suggesting that the nature of the rhodium species on the $Rh/CeO_2(Pr)/\gamma\text{-}Al_2O_3$ catalyst does not change during the N_2O decomposition tests.

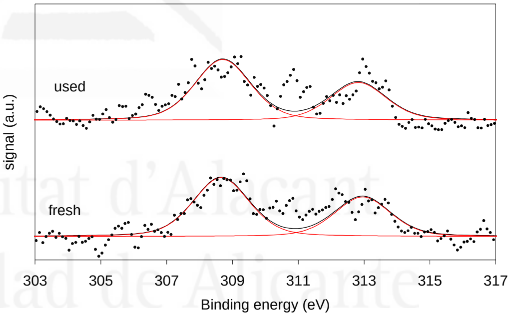

Figure 9. XPS characterization of the fresh and used $Rh/CeO_2/(Pr)/\gamma\text{-}Al_2O_3$ catalyst (Rh 3d transition).

As a summary, it can be concluded that the main physical and chemical properties of the $Rh/CeO_2(Pr)/\gamma\text{-}Al_2O_3$ catalyst do not change during the N_2O decomposition reaction in the real nitric acid plant gas streams. This observation is consistent with the high stability of this catalyst observed during the catalytic tests.

6.4. Conclusions

The main conclusions obtained from the results presented and discussed in this chapter are:

- The $Rh/CeO_2(Pr)/\gamma\text{-}Al_2O_3$ catalyst is active enough to ensure 100 % N_2O removal in the realistic reaction conditions of a nitric acid plant used in this study.

- The $Rh/CeO_2(Pr)/\gamma\text{-}Al_2O_3$ catalyst is highly stable and high N_2O decomposition rates were maintained for 40 hours of operation in real nitric acid plant streams.

- The main physicochemical features of the catalyst do not change during the N_2O decomposition experiments in the nitric acid plant: (i) XRD and Raman spectroscopy did not show any change in the fluorite structure of the Ce-Pr mixed oxide after the catalytic tests, (ii) the crystal size of the Ce-Pr mixed oxide and the BET surface area of the catalyst did not change during the catalytic tests, evidencing no sintering of ceria, (iii) H_2-TPR indicates that the reducibility of the catalyst is similar before and after the catalytic tests, revealing chemical stability, and (iv) the stability of the rhodium particles size and rhodium oxidation state was deduced from TEM and XPS, respectively.

References

[1] Proposal for a DIRECTIVE OF THE EUROPEAN PARLIAMENT AND OF THE COUNCIL amending Directive 2003/87/EC so as to improve and extend the greenhouse gas emision allowance Trading system of the Community, Brussels, 23.1.2008 COM(2008) 16 final, 2008/0013 (COD).
[2] F. Kapteijn, J. Rodríguez-Mirasol, J.A. Moulijn, Appl. Catal. B 9 (1996) 25.
[3] J. Pérez-Ramírez, F. Kapteijn, K. Schöffel, J.A. Moulijn, Appl. Catal. B 44 (2003) 117.
[4] G. Centi, S. Perathoner, F. Vanazza, M. Marella, M. Tomaselli, M. Mantegazza, Adv. Environ. Res. 4 (2000) 325.

[5] J.N. Armor, T.A. Braymer, T.S. Farris, Y. Li, F.P. Petrocelli, E.L. Weist, S. Kannan, C.S. Swamy, Appl. Catal. B 7 (1996) 397.

[6] T.W. Dann, K.H. Schulz, M. Mann, M. Collings, Appl. Catal. B 6 (1995) 1.

[7] X.F. Wang, H.C. Zheng, Appl. Catal. B 3 (1993) 55.

[8] J. Oi, A. Obuchi, G.R. Bamwenda, A. Ogata, H. Yagita, S. Kushiyama, K. Mizuno, Appl. Catal. B 12 (1997) 277.

[9] G. Centi, A. Galli, B. Montanari, S. Perathoner, A. Vaccari, Catal. Today 35 (1997) 113.

[10] J. Oi, A. Obuchi, A. Ogata, G.R. Bamwenda, K. Tanaka, T. Hibino, S. Kushiyama, Appl. Catal. B 13 (1997) 197.

[11] J. Kašpar, P. Fornasiero, M. Grazini, Catal. Today 50 (1999) 285.

[12] L.N. Ikryannikova, A.A. Aksenov, G.L.Markaryan, G.P.Murav'eva, B.G. Kostyuk, A.N. Kharlanov, E.V. Lunina, Appl. Catal. A 210 (2001) 225.

[13] A. Mineshige, T. Taji, Y. Muroi, M. Kobune, S. Fujii, N. Nishi, M. Inaba, Z. Ogumi, Solid State Ion. 135 (2000) 481.

[14] A. Bueno-López, I. Such-Basáñez, C. Salinas-Martínez de Lecea, J. Catal. 244 (2006) 102.

[15] S. Parres-Esclapez, M.J. Illán-Gómez, C. Salinas-Martínez de Lecea, A. Bueno-López, Appl. Catal. B 96 (2010) 370.

[16] S. Parres-Esclapez, I. Such-Basañez, M.J. Illán-Gómez, C. Salinas-Martínez de Lecea, A. Bueno-López, J. Catal. 276 (2010) 390.

[17] C. Bueno-Ferrer, S. Parres-Esclapez, D. Lozano-Castelló, A. Bueno-López. J. Rare Earths, 28 (2010) 647.

[18] M. Meng, Y.Q. Zha, J.Y. Luo, T.D. Hu, Y.N. Xie, T. Liu, J. Zhang, Appl. Catal. A 301 (2006) 145.

[19] M. Fernández-García, A. Martínez-Arias, A. Iglesias-Juez, C. Belver, A. B. Hungría, J.C. Conesa, J. Soria, J. Catal. 194 (2000) 385.

[20] J. Soria, A. Martinez-Arias, J.L.G. Fierro, J.C. Conesa, Vacuum 46 (1995) 1201.

CHAPTER VII

General Conclusions

In this thesis a series of Rh, Pd and Pt catalysts supported on γ-Al_2O_3, CeO_2 and CeO_2 doped with La or Pr, were prepared, characterized and tested at a laboratory scale. The N_2O decomposition mechanism over Rh/γ-Al_2O_3 and Rh/CeO_2 catalysts was studied in high detail by application of various spectroscopic techniques and isotopic labeling experiments. Furthermore, a tailored Rh/CeO_2(Pr)/γ-Al_2O_3 catalyst, which showed high potential for N_2O decomposition on the industrial scale, was studied on the laboratory and pilot plant scales. Finally, the effect of inhibitors such as H_2O, O_2 and NO_x was also determined. From the work presented in this thesis, the following general conclusions can be drawn:

- The catalytic activity for N_2O decomposition follows the trend Rh > Pd > Pt. The support has a significant influence on the activity of these noble metals. A relation was found between the reducibility of the CeO_2 support, which was catalyzed by the different noble metals, and their ability to decompose N_2O.

- The rate-limiting step of the N_2O decomposition mechanism over CeO_2-based noble metal catalyst appears to be the reduction of the catalytically active sites. For Rh catalysts, the CeO_2 support, either bare or doped, is directly involved in the N_2O decomposition process, while CeO_2 participation is not so evident for Pd and Pt catalysts.

- The Rh/γ-Al_2O_3 catalyst is less active for N_2O decomposition than Rh/CeO_2, and the apparent activation energies (146 and 121 kJ/mol, respectively) are consistent with these differences in activity. The different activity is related to the fact that the CeO_2 support is actively involved in the N_2O decomposition mechanism while γ-Al_2O_3 is not.

- The CeO_2 support strongly interacts with Rh and stabilizes very small, oxidized noble metal particles during N_2O decomposition, while rhodium on Rh/γ-Al_2O_3 is reduced to Rh^0 under the same conditions.

- N_2O decomposition over Rh/γ-Al_2O_3 mainly occurs via the Eley-Rideal mechanism, resulting in the successive oxidation and reduction of the noble metal sites by N_2O. The Langmuir-Hinshelwood mechanism, resulting in oxidation of Rh by N_2O and recombination of two oxygen atoms on Rh sites yielding molecular oxygen, has a marginal contribution.

- In Rh/CeO_2, once N_2O reduces a Rh site, this site can be reoxidized by either another N_2O molecule or by CeO_2 oxygen. In the latter case, N_2O subsequently oxidizes the vacant site created on CeO_2. As a result, the active sites for N_2O chemisorption and decomposition are not only located on Rh but also on CeO_2.

- The activity of the supported Rh/CeO_2(Pr)/γ-Al_2O_3 catalyst is slightly lower than that of the powdered active phase (Rh/CeO_2(Pr)). This difference is attributed to the changes in the interaction between CeO_2(Pr) and γ-Al_2O_3, which in turns affects the interaction of Rh with CeO_2(Pr).

- The activity of the Rh/CeO_2(Pr)/γ-Al_2O_3 catalyst is partially inhibited in the presence of O_2, H_2O and NO_x. NO_x is the strongest inhibitor and O_2 the weakest. The inhibiting effect of O_2 is attributed to its reversible chemisorption on catalyst sites, while the effect of H_2O and NO_x is mainly related to irreversible chemisorption. The inhibiting effect of H_2O is lower than NO_x because the Ce-OH surface groups formed as a result of H_2O chemisorption are suitable for N_2O chemisorption and decomposition, while the surface nitrogen species created upon NO_x chemisorption are not. In spite of the inhibiting effect of NO_x, O_2 and H_2O, the Rh/CeO_2(Pr)/γ-Al_2O_3 catalyst can decompose N_2O above 350-400 ºC.

- The Rh/CeO_2(Pr)/γ-Al_2O_3 catalyst is highly stable and high N_2O decomposition rates were maintained reaction for at least 40 hours of operation in real nitric acid plant streams. The main physicochemical features of the catalyst do not change during the N_2O decomposition experiments in the nitric acid plant.

Resumen en castellano

Catalizadores de rodio/ceria para la descomposición de N_2O

1. Introducción General

1.1. Efecto invernadero y calentamiento global

El clima se ve notablemente afectado por cambios en la concentración atmosférica de determinados gases que son capaces de retener parte de la radiación infrarroja procedente de la superficie de la Tierra. Como se esquematiza en la Figura 1, una fracción de la radiación solar que es reflejada en la superficie terrestre no atraviesa la atmósfera. Esto es debido a la presencia de gases como el vapor de agua y el dióxido de carbono que absorben dicha radiación para después devolverla hacia la superficie terrestre, originando el fenómeno conocido como efecto invernadero. El efecto invernadero es un fenómeno natural, responsable de la temperatura media de la superficie terrestre y sin el cual la superficie de la Tierra estaría a una temperatura de unos 33 ºC por debajo de la actual [1-3].

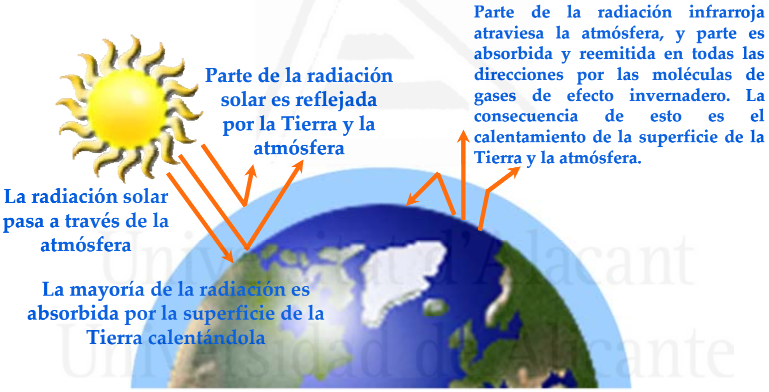

Figura 1. Esquema de la retención de radiación en la superficie terrestre responsable del efecto invernadero.

El problema actual relacionado con el calentamiento global radica en que el aumento de la concentración de gases de efecto invernadero, como consecuencia de la actividad humana, origina que una mayor fracción de radiación sea reflejada hacia la superficie terrestre. Las estrategias utilizadas para reducir el efecto invernadero se han centrado, principalmente, en la eliminación de las emisiones de CO_2, pero la importancia de otros gases como el metano, el óxido nitroso (N_2O) y los compuestos halogenados, como los CFC y los perfluorocarbonados (PFC) se ha puesto de manifiesto en los últimos años.

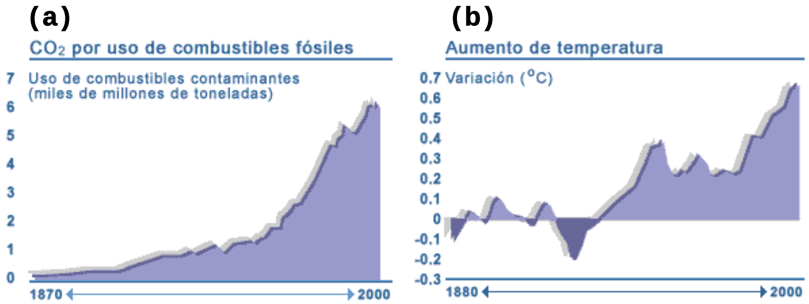

Figura 2. Aumento de las emisiones de CO_2 por uso de combustibles fósiles (a) y variación de la temperatura media del planeta durante el último siglo. (Información suministrada por BBC [4]).

En los últimos cien años la actividad humana ha generado un aumento de la concentración de gases de efecto invernadero y otros agentes contaminantes de la atmósfera. En la Figura 2a se muestra una estimación de las emisiones de CO_2 durante el último siglo. En la Figura 2b se observa que, en el mismo período, se ha registrado un aumento notable, en términos históricos, de la temperatura media del planeta. Aunque no se puede establecer con certeza en qué medida puede atribuirse este calentamiento al efecto del aumento de la concentración de gases de efecto invernadero, sí que existe la evidencia de que la actividad humana está modificando el efecto invernadero natural y, como consecuencia de ello, surge el fenómeno del calentamiento global.

En este sentido, es importante estimar hasta qué punto las consecuencias perjudiciales del cambio climático podrían reducirse mediante medidas de control de las emisiones. Además, el plazo para perfilar una política de actuación es clave, ya que existe un largo desfase entre la reducción en la emisión de gases con efecto invernadero y la estabilización de sus concentraciones atmosféricas.

1.2. Emisiones de N_2O

Este trabajo de investigación se centra en abordar el problema de las emisiones de N_2O a la atmósfera. Este compuesto se consideró inocuo durante mucho tiempo, pero se ha demostrado que contribuye a la destrucción de la capa de ozono así como al calentamiento global del planeta, siendo mucho más nocivo que el CO_2. Así, se ha estimado que cada gramo de N_2O emitido a la atmósfera contribuye al efecto invernadero de modo equivalente a unos 300 gramos de CO_2. La emisión anual de N_2O a la atmósfera debido a actividades humanas se cifra en 4,7-7 millones de toneladas [5]. Algunos científicos apuntan que habría que reducir en un 70-80 % las emisiones antropogénicas para conseguir un balance nulo entre el N_2O emitido a la atmósfera y el que el planeta es capaz de eliminar por medios naturales. De hecho, evitar las emisiones de N_2O antropogénico se estima que equivaldría, desde el punto de vista del efecto invernadero, a eliminar las emisiones de CO_2 acordadas en la cumbre de Kioto.

El N_2O se emite debido a actividades agrícolas, industriales (producción de ácidos adípico y nítrico, etc) y transportes. Las emisiones procedentes del transporte terrestre han aumentado debido al incremento del tráfico rodado. El incremento en las emisiones se debe en gran medida a la introducción de los catalizadores de tres vías en vehículos a gasolina, que reducen sustancialmente las emisiones de óxidos de nitrógeno, monóxido de carbono e hidrocarburos, pero liberan una cierta cantidad de óxido nitroso. En este tipo de sistemas catalíticos, la emisión de N_2O se ha relacionado con el envejecimiento del catalizador.

Un sector con una importante producción de N_2O son las plantas de ácido nítrico. El ácido nítrico se obtiene por oxidación catalítica de amoníaco. Durante esta reacción, el N_2O se forma como un subproducto y se libera a la atmósfera. En la actualidad, la industria del ácido nítrico utiliza controles para las emisiones de NO y NO_2 (es decir, deNOx), basados en una combinación de tecnologías NSCR y SCR. En el proceso de eliminación de NOx, los sistemas de NSCR son también muy eficaces en la destrucción de N_2O. Sin embargo, las unidades de NSCR generalmente no son aplicadas en plantas modernas debido a los altos costes energéticos.

1.3. Descomposición catalítica de N_2O

Para evitar la emisión del N_2O a la atmósfera, la solución más eficaz es utilizar catalizadores que permitan su descomposición o que faciliten su reacción con un agente reductor. En el caso de la descomposición, el N_2O se transforma en N_2 y O_2:

$$2N_2O \rightarrow 2N_2 + O_2 \quad \rightarrow \quad \Delta H^{o}(25\ ^{o}C) = -\ 163\ kJ/mol$$

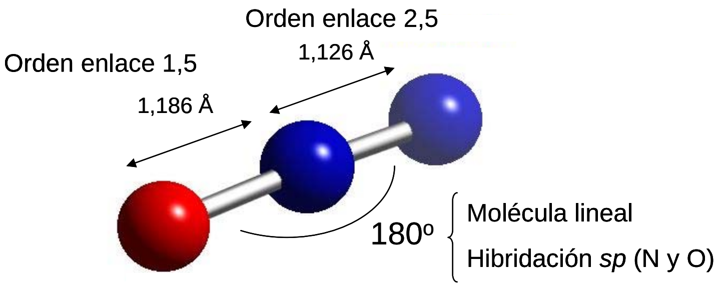

Figura 3. Esquema y algunas propiedades de los enlaces de la molécula de N_2O.

En la molécula asimétrica de N_2O (N-N-O), el orden de enlace N-N es 2,5 mientras que el de N-O es 1,5, por lo que la ruptura del enlace N-O es más fácil. La energía de activación para la disociación térmica del enlace N-O es de aproximadamente 250-270 KJ/mol, requiriéndose temperaturas superiores a 625 ºC para que la ruptura espontánea de dicho enlace comience a ser apreciable. El principal papel de un catalizador que acelera la descomposición de N_2O es transferir densidad de carga al orbital antienlazante del enlace N-O, debilitándolo y disminuyendo la energía de activación del proceso. Por otro lado, la eliminación de N_2O se ve favorecida por la presencia de especies reductoras como CO o hidrocarburos.

Se han estudiado numerosos catalizadores para descomponer N_2O, entre los que se incluyen metales no soportados y soportados, óxidos puros y mixtos y zeolitas [5,8]. Los catalizadores metálicos más estudiados son Pt, Pd, Ag, Au y Ge, con los que la descomposición de N_2O ocurre a temperaturas superiores a 375 ºC. Los óxidos puros son también activos y las actividades más altas las muestran los óxidos de Rh, Ir, Co, Fe, Ni, Cu y algunos óxidos de tierras raras. En todos ellos la temperatura de inicio de la descomposición está entre 225 y 425 ºC. Otros sólidos a los que se ha prestado especial atención son los óxidos mixtos (como óxidos dopados o disoluciones sólidas) tipo espinelas y perovskitas. En los estudios publicados, las disoluciones sólidas de CoO y MgO presentan actividad a temperaturas por encima de 225 ºC, mostrando el resto de disoluciones sólidas ensayadas actividad a temperaturas más elevadas. Por ejemplo, ciertas espinelas y perovskitas son activas a partir de 325 ºC. Los metales u óxidos metálicos soportados en sílice o alúmina tienen actividades muy variadas con temperaturas de descomposición de N_2O entre 225 y 600 ºC, siendo el Rh_2O_3 soportado en Al_2O_3 uno de los más eficaces aunque, empleando soportes zeolíticos se obtienen ventanas de actividad similares.

El análisis de la información publicada sobre el tema sugiere que catalizadores que combinen metales u óxidos metálicos activos como, por ejemplo, Rh_2O_3, con soportes del tipo CeO_2 (puros y dopados) pueden ser interesantes para la eliminación de N_2O. Además, este tipo de soportes han demostrado ser muy efectivos en otras aplicaciones como la reducción de NO_x con CO e hidrocarburos [9,10], entre otras. Por este motivo, este trabajo de investigación se ha centrado en el estudio de catalizadores para la descomposición de N_2O consistentes en metales nobles soportados en óxidos de cerio.

1.4. Legislación

Actualmente no existe una normativa que límite las emisiones de N_2O a la atmósfera. Como se ha descrito en el apartado *1.2*, estas emisiones provienen en gran parte de plantas de ácido nítrico y adípico. Existen alrededor de 80-100 plantas de ácido nítrico en la Unión Europea, y unos 10 productores de ácido adípico [11]. De las emisiones totales de N_2O que provienen de la industria del ácido nítrico en Europa se estiman en 130 Ktoneladas por año, equivalentes desde el punto de vista de el efecto invernadero a 40 Mtoneladas de CO_2. En las condiciones más favorables, se emiten 3 kg de N_2O por tonelada de HNO_3 producido, pero la media de emisiones en las plantas es de 6 kg de N_2O por tonelada de HNO_3 producido [12].

Próximamente las emisiones de N_2O generadas por la industria de fertilizantes en Europa se van a ver afectadas por una nueva legislación medioambiental establecida por la IPPC (Integrated Pollution Prevention and Control). Además, este organismo pretende instaurar en las plantas de ácido nítrico las mejores técnicas disponibles, denominadas técnicas BAT (Best Available Techniques), para la eliminación de N_2O. El principal problema de aplicar esta tecnología es el afrontar los grandes costes que implica su puesta en marcha [12]. Se requiere por lo tanto desarrollar nuevas tecnologías que permitan la eliminación de N_2O en estas instalaciones de modo más efectivo y económico.

1.5. Objetivos

El objetivo general de este estudio es desarrollar un catalizador eficaz para descomponer N_2O en corriente gaseosas. Los objetivos específicos son:

- Estudiar la descomposición de N_2O con catalizadores de Rh, Pd y Pt soportados en alúmina, ceria y ceria dopada con La o Pr, tratando de relacionar la actividad catalítica de estos materiales en experimentos a escala laboratorio con sus propiedades físico-químicas.

- Estudiar el efecto del soporte en el mecanismo de descomposición de N_2O con catalizadores Rh/CeO_2 y $Rh/\gamma\text{-}Al_2O_3$. Para ello, se han combinando experimentos de descomposición catalítica en estado estacionario a escala laboratorio, cálculos de parámetros cinéticos, caracterización mediante XPS *in situ* en condiciones de reacción, experimentos DRIFTS y Raman *in situ* y experimentos en condiciones transitorias mediante la técnica de pulsos con gases isotópicos.

- Síntesis de la fase activa con mejores propiedades catalíticas según los estudios previos, utilizando como soporte partículas de alúmina. Para ello se requiere estudiar el efecto de las propiedades físico-químicas del catalizador, así como la interacción Ce-Al y analizar la influencia de los diferentes inhibidores (O_2, H_2O y NOx) en el transcurso de la reacción mediante espectroscopía DRIFTS.

- Estudiar la actividad y estabilidad de un catalizador $Rh/CeO_2(Pr)/\gamma\text{-}Al_2O_3$ para la eliminación de N_2O en una planta de producción de ácido nítrico, así como analizar las propiedades físico-químicas del catalizador antes y después de las pruebas catalíticas, con el objetivo de identificar posibles cambios.

2. Descomposición de N_2O con catalizadores de Rh, Pd y Pt soportados en alúmina y ceria

2.1. Experimental

Los catalizadores que se han utilizado en este apartado son: Rh/CeO_2, Rh/CeO_2(Pr), Rh/CeO_2(La), Pd/CeO_2, Pd/CeO_2(Pr), Pd/CeO_2(La), Pt/CeO_2, Pt/CeO_2(Pr), Pt/CeO_2(La), Rh/γ-Al_2O_3, Pd/γ-Al_2O_3 y Pt/γ-Al_2O_3, donde CeO_2(Pr) = $Ce_{0,9}Pr_{0,1}O_2$ y CeO_2(La) = $Ce_{0,9}La_{0,1}O_2$. Los soportes de CeO_2 fueron preparados empleando $Ln(NO_3)_3{\cdot}6H_2O$ (Ln = Ce, La, Pr) como precursores. Las cantidades requeridas de cada precursor se mezclaron en un mortero y se calcinaron en aire a 600 ºC durante 90 minutos (rampa de calentamiento 10 ºC/min). Los soportes fueron impregnados con $Pt(NH_3)_4(NO_3)_2$, $Rh(NO_3)_3$ o $(Pd(C_2H_3O_2)_2)_3$ disueltos en el mínimo volumen de agua para conseguir una cantidad de metal noble del 0,5% en peso y, después, se secaron a 200 ºC y se calcinaron a 500 ºC en aire durante dos horas.

La superficie específica BET de los soportes ha sido determinada mediante adsorción de N_2 a -196 ºC y sus características estructurales se han estudiado por difracción de rayos X y espectroscopía Raman. Además, se ha determinado la reducibilidad de los soportes y de los catalizadores mediante experimentos de reducción a temperatura programada con H_2 (RTP-H_2). Finalmente, el tamaño de las partículas de los metales nobles se ha obtenido por microscopía TEM.

Para determinar la actividad catalítica, se han realizado ensayos de descomposición de N_2O a escala de laboratorio. En primer lugar se ha analizado el comportamiento de todos los catalizadores, utilizando una corriente de gas compuesta por N_2O y He. A partir de los resultados de estos experimentos, se seleccionaron los catalizadores Rh/CeO_2(Pr), Pd/CeO_2(Pr) y Pt/CeO_2(Pr) para realizar ensayos en presencia de especies gaseosas oxidantes (O_2) y reductoras (CO).

2.2. Resultados y discusión

De los resultados de caracterización obtenidos mediante espectroscopía Raman y difracción de rayos X, se puede deducir que los soportes presentan estructura tipo fluorita. El La y Pr se encuentran en la red cristalina de CeO_2 formando un óxido mixto. La presencia de La y Pr en la red cristalina deforma la estructura disminuyendo considerablemente la intensidad de la banda F_{2g} (a 459 cm^{-1}), y en el caso del La, desplazando la posición de los picos de difracción.

El área BET de los soportes CeO_2 y γ-Al_2O_3 es similar (76 y 78 m^2/g respectivamente) y la introducción de dopantes en la estructura del CeO_2 disminuye el área, respecto a la del CeO_2 puro. Esta disminución en concordancia con el aumento del tamaño de medio cristal desde 13 nm para el CeO_2 puro hasta 17-20 nm para los soportes dopados, según predice el modelo de Williamson Hall. De estos resultados se deduce que la incorporación de La o Pr al soporte de CeO_2 provoca la sinterización parcial del material. Este efecto de los dopantes se produce cuando este tipo de óxidos mixtos se calcinan a temperaturas moderadas, como es el caso de este estudio (600 ºC).

La reducibilidad de las diferentes muestras se ha analizado con experimentos de Reducción a Temperatura Programada con H_2 (RTP-H_2). La introducción de dopantes favorece la reducción de Ce^{4+} a Ce^{3+} y aumenta la movilidad del oxígeno en la red cristalina del soporte mejorando sus propiedades redox. Independientemente del soporte, las menores temperaturas de reducción se consiguen empleando Rh, y sigue la tendencia Rh>Pd>Pt. Como se demostrará más adelante, la reducibilidad del soporte a baja temperatura tiene un papel importante en la descomposición catalítica de N_2O.

En la Figura 4 se observan los perfiles de conversión de N_2O obtenidos en los ensayos catalíticos realizados con 1000 ppm N_2O/He empleando las diferentes muestras con Rh y sin metal noble (Figura 4a), con Pd (Figura 4b) y con Pt (Figura 4c).

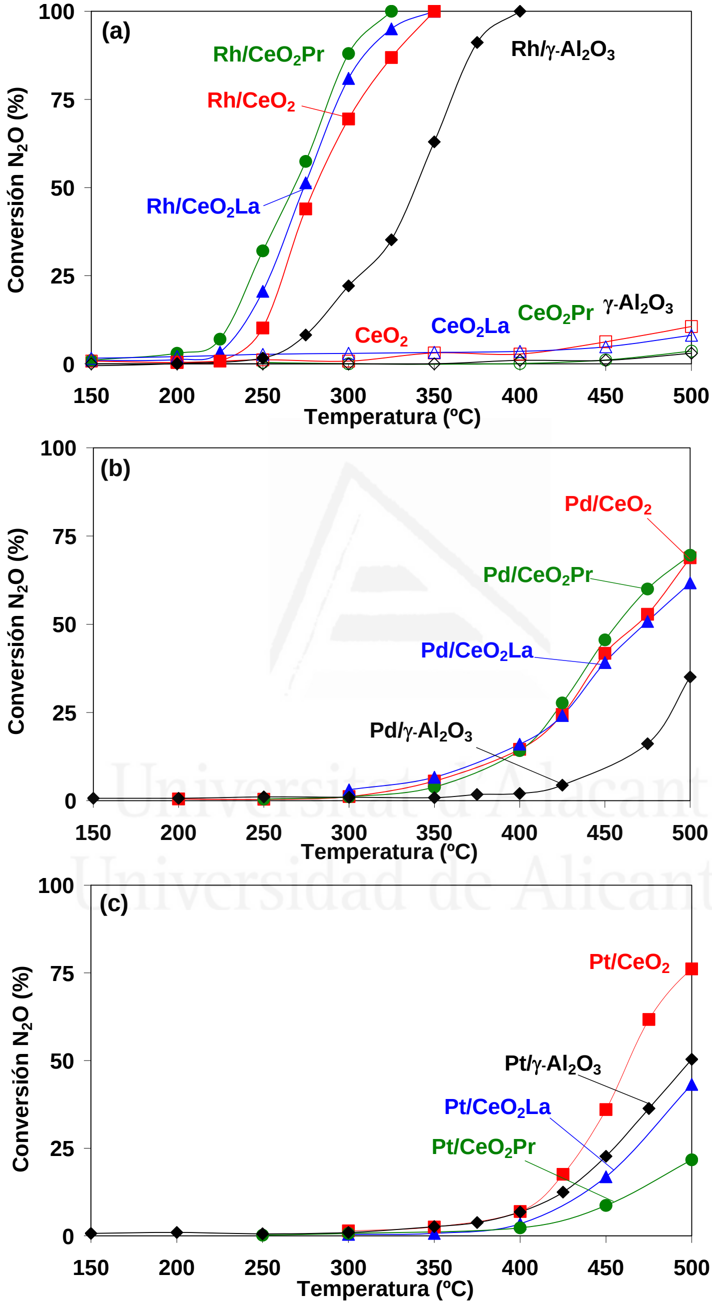

Figura 4. Conversión de N_2O con los catalizadores de (a) Rh, (b) Pd y (c) Pt.

Los soportes presentan una actividad baja en el intervalo de temperaturas estudiado alcanzando, en el mejor de los casos que es el de CeO_2 puro, ~10% de conversión a 500 ºC. Al introducir un metal noble aumenta la actividad catalítica y, como tendencia general, se observa que los catalizadores de Rh son más activos que los que contienen Pd o Pt. Como ya se ha comentado, los soportes en los catalizadores de Rh se reducen a menor temperatura y parece que la reducibilidad del soporte es una característica que afecta a la actividad catalítica para la descomposición de N_2O.

Los catalizadores de Rh son activos para la descomposición de N_2O a partir de 200-250 ºC, alcanzando la conversión completa en el intervalo 300-400 ºC, dependiendo del soporte empleado. La actividad de los catalizadores de Rh sigue la tendencia:

$$Rh/CeO_2(Pr) > Rh/CeO_2(La) > Rh/CeO_2 > Rh/\gamma\text{-}Al_2O_3$$

Así, se concluye que los soportes de CeO_2, tanto puro como dopado, aumentan la actividad catalítica del Rh respecto al soporte de Al_2O_3 y, en concordancia con los resultados previos a este estudio [13], la mayor actividad se consigue con el soporte de CeO_2 dopado con Pr.

Los catalizadores de Pd (Figura 4b) y Pt (Figura 4c) son mucho menos efectivos para descomponer N_2O que los de Rh y, en ningún caso se alcanza el 100% de conversión en el intervalo de temperaturas estudiado. Entre los catalizadores de Pd, los soportados en CeO_2 puro y dopado muestran similar actividad, siendo esta superior a la del catalizador $Pd/\gamma\text{-}Al_2O_3$. Esto indica que también en este caso es beneficioso emplear un soporte de CeO_2 respecto a la Al_2O_3, pero, en cambio, resulta indiferente modificar las propiedades del CeO_2 introduciendo dopantes.

En el caso del Pt (Figura 4c), el efecto del soporte es más complicado de interpretar pues tanto el tamaño de las partículas de metal noble como las propiedades redox del soporte parecen afectar a la actividad de este metal noble, que es también menos efectivo que el rodio. Según estos resultados, el empleo de soportes de CeO_2 puro o dopados respecto al empleo de alúmina tiene un doble efecto sobre el Pt: por un lado, aumentan el tamaño de partícula de Pt, lo que incrementa la actividad catalítica pero, por otro, mejora la movilidad del oxígeno del soporte, lo que disminuye la actividad catalítica.

Para concluir la discusión sobre los ensayos catalíticos, se han intentado analizar con más detalle los parámetros que condicionan la descomposición de N_2O con catalizadores de Rh, Pd y Pt soportados en CeO_2 puro y dopado. Como se ha indicado previamente, parece que existe una relación entre la reducibilidad de los soportes de CeO_2 y la actividad de los catalizadores para la descomposición de N_2O. Para obtener datos que muestren esta relación, se han determinado, por un lado, las temperaturas a las que comienza la descomposición de N_2O en los ensayos catalíticos (Figura 4) tomándose como criterio que la descomposición alcance un valor del 10% y, por otro lado, a partir de los RTP-H_2 se ha determinado la temperatura del máximo de reducción superficial para cada uno de los catalizadores con soporte de CeO_2 puro y dopado. En la Figura 5 se representa la temperatura de descomposición frente a la de reducción, observándose que existe una relación entre la reducibilidad de los soportes, catalizada por los distintos metales nobles, y su actividad para la descomposición de N_2O. Así, cuanto menor es la temperatura de reducción, menor es la temperatura de inicio de descomposición de N_2O. Para los catalizadores de Pt, la tendencia es la opuesta, lo que pone de manifiesto, de nuevo, que al Pt le afecta negativamente que los soportes presenten buenas propiedades redox. Como tendencia general se confirma que, tanto la actividad como la reducibilidad de los tres metales nobles estudiados, siguen la secuencia Rh>Pd>Pt. Además, estos resultados sugieren que la etapa limitante de la velocidad de descomposición de N_2O es la reducción de los sitios activos del catalizador y que los soportes de CeO_2 participan en el mecanismo de descomposición de N_2O.

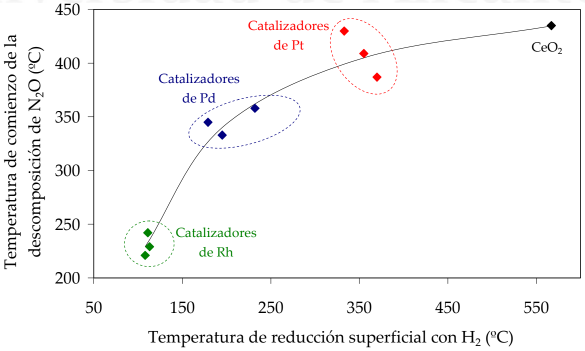

Figura 5. Relación entre la reducibilidad de los soportes de CeO_2 pura y dopada catalizada por los distintos metales nobles y la capacidad de descomponer N_2O.

Con el fin de profundizar en el efecto que tienen los procesos redox en la descomposición de N_2O se han llevado a cabo ensayos catalíticos empleando mezclas gaseosas que, además de N_2O, contienen un gas oxidante (O_2) o reductor (CO) y para estos ensayos se han utilizado, únicamente, los catalizadores de Rh, Pd y Pt soportados en CeO_2(Pr).

El oxígeno tiene un efecto inhibidor sobre la reacción de descomposición de N_2O, disminuyendo la actividad catalítica. Como se ha indicado, la actividad de los catalizadores estudiados para la descomposición de N_2O está relaciona con la reducibilidad superficial del soporte, por lo que la incorporación de un gas oxidante, como el oxígeno, disminuye la actividad catalítica. Como describen Kapteijn y col. en una revisión bibliográfica dedicada a la descomposición catalítica de N_2O [14], el efecto inhibidor del O_2 se ha observado en muchos de los catalizadores propuestos para su descomposición.

Por otro lado, en una atmósfera reductora, como la de CO, se favorece notablemente la conversión de N_2O. Este aumento resulta moderado en el caso del Rh pero es muy significativo para los catalizadores de Pd y Pt. Estos resultados sugieren, de nuevo, que la etapa limitante de la velocidad de descomposición de N_2O es la reducción de los sitios activos del catalizador. Esto explica, por un lado, que cuanto más fácilmente se reduzca el sistema metal noble-soporte mayor sea su actividad y, por otro lado, que al acelerar la etapa de reducción incorporando CO a la corriente, aumente considerablemente la conversión de N_2O.

2.3. Conclusiones

El estudio de la descomposición de N_2O con catalizadores de Rh, Pd y Pt soportados en alúmina, CeO_2 y CeO_2 dopado con La o Pr permite llegar a las siguientes conclusiones:

- Los tres metales nobles estudiados (Rh, Pd y Pt) catalizan la descomposición de N_2O, siendo el Rh el catalizador más activo.

- Las propiedades redox de los soportes afectan a la actividad catalítica de los catalizadores de Rh. Los soportes basados en ceria presentan mayor actividad que los soportes de alúmina.

- La actividad para la descomposición de N_2O de los catalizadores basados en ceria está relacionada con su reducibilidad en presencia de H_2, y cuanto más fácil es la reducción, mayor es la actividad catalítica.

- La etapa limitante de la velocidad en el mecanismo de descomposición de N_2O en catalizadores basados en ceria parece ser la reducción de los sitios activos del catalizador. En los catalizadores de Rh, los soportes de ceria parecen estar involucrados en la descomposición de N_2O, mientras que para los catalizadores de Pd y Pt la participación de la ceria no es tan evidente.

3. Estudio del mecanismo de descomposición de N_2O con catalizadores de Rh/CeO_2 y $Rh/\gamma\text{-}Al_2O_3$

3.1. Experimental

Los catalizadores empleados en este apartado, para estudiar el efecto del soporte sobre la actividad del rodio, fueron Rh/CeO_2 y $Rh/\gamma\text{-}Al_2O_3$..

Los soportes y los catalizadores se han caracterizado utilizando espectroscopía Raman, DRX, isotermas de adsorción de N_2 a -196 ºC, RTP-H_2 y TEM. Cabe mencionar que ambos soportes presentan similar área BET (76 m^2/g CeO_2 y 78 m^2/g $\gamma\text{-}Al_2O_3$) y similar tamaño de partícula de rodio (tamaño medio de partículas de rodio 2.2 nm en Rh/CeO_2 y 2.3 nm en $Rh/\gamma\text{-}Al_2O_3$, observado por TEM).

Se han realizado diferentes tipos de ensayos para determinar la actividad catalítica y obtener información sobre los mecanismos por los cuales actúan estos catalizadores:

- Ensayos catalíticos a escala laboratorio de descomposición de N_2O con diferentes concentraciones de N_2O (100, 300, 650, 1000 y 1400 ppm).

- Experimentos de intercambio isotópico en los que, antes del inicio del experimento, los catalizadores fueron pretratados con un flujo de oxígeno (30 ml/min) a 400 ºC durante 30 min. A continuación, se trataron los catalizadores térmicamente a diferentes temperaturas (50, 200, 250, 300, 350 y 400 ºC) en gas inerte (He, 10 ml/min) y, una vez alcanzada la temperatura, se introdujeron pulsos de $^{15}N_2{}^{18}O$ en la muestra (3 pulsos a cada temperatura).

- Por otra parte, se realizaron mediciones mediante las técnicas espectroscópicas DRIFTS y Raman, en condiciones de reacción con una composición de 1000 ppm de N_2O, y mediante XPS tras pretratamientos in situ en esa misma atmósfera.

3.2. Resultados y discusión

3.2.1. Efecto de la presión parcial de N_2O

Se ha estudiado el efecto de la presión parcial de N_2O en la actividad de los catalizadores empleando para ello presiones parciales de entrada de 100, 300, 650, 1000 y 1400 ppm. Los datos obtenidos se muestran en la Figura 6. El catalizador Rh/CeO_2 es más activo que el catalizador $Rh/\gamma\text{-}Al_2O_3$. Con los datos obtenidos se realizaron ajustes cinéticos para determinar el orden de reacción respecto al N_2O, en cada catalizador, y la energía de activación del proceso. El aumento en la presión parcial de entrada de N_2O produce una disminución en el % de descomposición de N_2O. Esto es consistente con ordenes de reacción menores de 1. Ambos catalizadores presentan un orden de reacción similar. La energía de activación obtenida con Rh/CeO_2 es menor que la de $Rh/\gamma\text{-}Al_2O_3$.

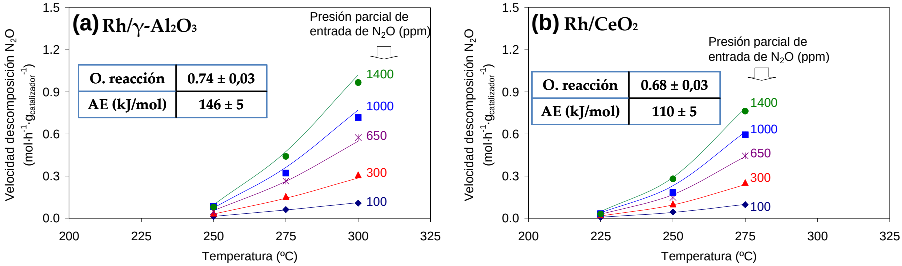

Figura 6. Velocidad de descomposición de N_2O en función de la temperatura a diferentes presiones parciales. (símbolos: datos experimentales, líneas: ajuste cinético).

3.2.2. Experimentos de intercambio isotópico

Se han realizado experimentos de pulsos con $^{15}N_2{}^{18}O$ y se ha analizado. La proporción de las diferentes especies de oxígeno molecular formadas. Estas proporciones, normalizadas respecto a la cantidad total de oxígeno molecular generada a cada temperatura, se muestran en la Figura 7.

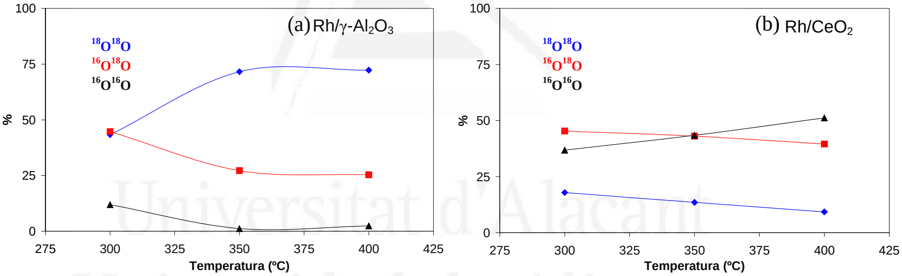

Figura 7. Naturaleza de las especies de oxígeno formadas como producto de la descomposición de $^{15}N_2{}^{18}O$.

El principal O_2 emitido para el catalizador Rh/γ-Al_2O_3 es $^{18}O_2$, indicando que la mayor parte del oxígeno emitido como producto procede del gas pulsado ($^{15}N_2{}^{18}O$). La emisión de $^{16}O_2$ y $^{16}O^{18}O$ es consistente con la reducción de Rh_2O_3 a Rh^0 en condiciones de reacción. El catalizador de Rh/CeO_2 genera principalmente $^{16}O_2$ y $^{16}O^{18}O$, que contienen átomos de oxígeno procedentes del catalizador, revelando la participación de la ceria en el mecanismo de reacción.

3.2.3. Experimentos DRIFTS in situ

La Figura 8 muestra los espectros DRIFT realizados con $\gamma\text{-}Al_2O_3$, $Rh/\gamma\text{-}Al_2O_3$, CeO_2 y Rh/CeO_2 en atmósfera de N_2O. En general, hay dos regiones del espectro que requieren especial atención: i) 2400-2100 cm^{-1}, asignado a la vibración del enlace de N_2 adsorbido o N_2O [15-18] y ii) por debajo de 1700 cm^{-1}, que se atribuye a las especies de nitrógeno oxidado (nitritos, nitratos y / o grupos nitro) [19,20].

Los espectros obtenidos con $\gamma\text{-}Al_2O_3$ y $Rh/\gamma\text{-}Al_2O_3$ son muy similares, lo que sugiere que muchas de las especies nitrogenadas observadas se forma sobre la alúmina y no están involucradas en el mecanismo de descomposición de N_2O. La naturaleza de las especies de nitrógeno creadas en la superficie de la ceria es mucho más heterogénea que las observadas en la alúmina. Algunas de las especies nitrogenadas creadas en la ceria no son estables durante la descomposición de N_2O, indicando que la ceria está involucrada en el proceso de descomposición de N_2O.

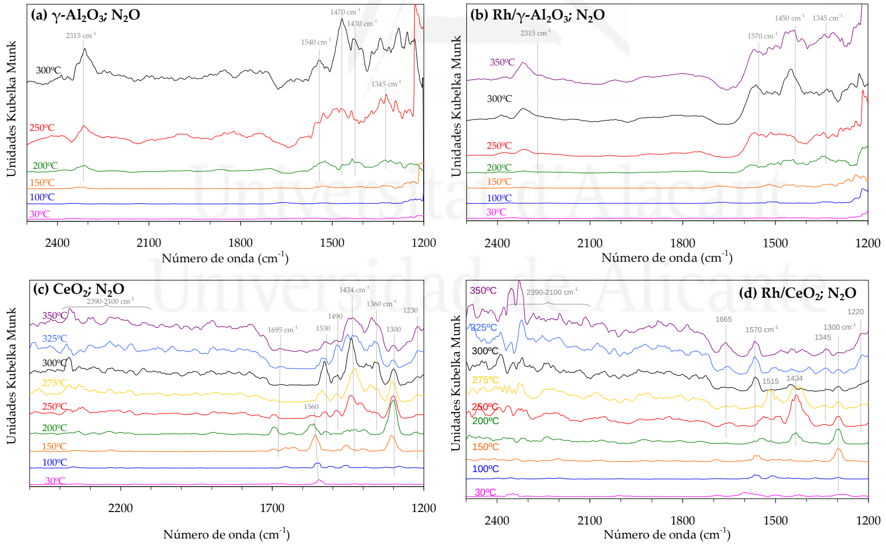

Figura 8. Espectros DRIFT *in situ* obtenidos a distintas temperaturas em 1000 ppm N_2O/He.

3.2.4. Experimentos de XPS in situ

Para obtener información sobre el efecto del soporte en la naturaleza de las especies de rodio presentes en cada catalizador así como sobre los cambios que sufren dichas especies durante los experimentos catalíticos se obtuvieron espectros de XPS de los catalizadores frescos y después de un tratamiento con N_2O a diferentes temperaturas. En Figura 9 se muestran los espectros correspondientes a las transiciones electrónicas Rh $3d_{3/2}$ y Rh $3d_{5/2}$, que aparecen con energías de ligadura centradas a 312-315 eV y 306-310 eV, respectivamente.

Al realizar los sucesivos tratamientos con N_2O a distintas temperaturas se observan cambios en el estado de oxidación del rodio, produciéndose la conversión parcial o total de Rh^{3+} a Rh^0 al aumentar la temperatura. Este proceso de reducción del metal noble durante la descomposición de N_2O afecta de modo diferente a cada catalizador, poniendo en evidencia un claro efecto del soporte en dicha reducción. El catalizador Rh/CeO_2 mantiene el Rh parcialmente oxidado en condiciones de reacción mientras que el Rh en γ-Al_2O_3 se reduce.

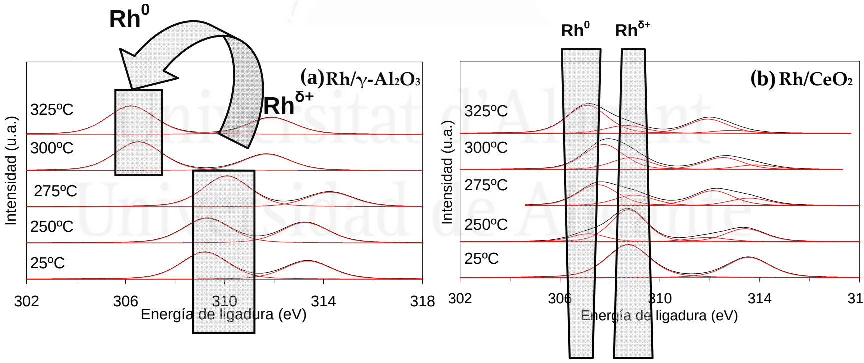

Figura 9. Espectros XPS correspondientes al Rh 3d de los catalizadores frescos y después de un tratamiento in situ a diferentes temperaturas con N_2O.

3.2.5. Discusión

Las diferentes técnicas usadas en este estudio aportan información complementaria sobre el mecanismo de descomposición de N_2O para los catalizadores Rh/γ-Al_2O_3 y Rh/CeO_2. De los experimentos realizados con pulsos de $^{15}N_2{}^{18}O$, se deduce que tienen lugar varios procesos redox en los catalizadores durante la descomposición de N_2O. Como principal conclusión, se ha demostrado que el CeO_2, en presencia de Rh, se involucra activamente en el mecanismo de descomposición de N_2O, mientras que la γ-Al_2O_3 no participa en dicho mecanismo. Con la información deducida de los diferentes experimentos realizados, se ha llegado a la conclusión de que la descomposición de N_2O para los catalizadores Rh/γ-Al_2O_3 y Rh/CeO_2 se puede describir según las siguientes etapas de reacción:

Mecanismo de descomposición para el catalizador Rh/γ-Al_2O_3:

$Rh^*\text{-}{}^{16}O + {}^{15}N_2{}^{18}O \rightarrow Rh^* + {}^{15}N_2 + {}^{18}O^{16}O$ Etapa 1
$Rh^* + {}^{15}N_2{}^{18}O \rightarrow Rh^*\text{-}{}^{18}O + {}^{15}N_2$ Etapa 2
$Rh^*\text{-}{}^{18}O + {}^{15}N_2{}^{18}O \rightarrow Rh^* + {}^{15}N_2 + {}^{18}O_2$ Etapa 1'
$Rh^*\text{-}{}^{16}O + Rh^*\text{-}{}^{16}O \rightarrow 2Rh^* + {}^{16}O_2$ Etapa 3

En el catalizador Rh/CeO_2, además de las etapas 1 a 3, también se producen los siguientes procesos:

$Rh^* + Ce^*\text{-}{}^{16}O \rightarrow Rh^*\text{-}{}^{16}O + Ce^*$ Etapa 4
$Ce^* + {}^{15}N_2{}^{18}O \rightarrow Ce^*\text{-}{}^{18}O + {}^{15}N_2$ Etapa 5
$2Ce^*\text{-}{}^{16}O \rightarrow 2Ce^* + {}^{16}O^{16}O$ Etapa 6
$Rh^*\text{-}{}^{16}O + Ce^*\text{-}{}^{16}O \rightarrow Rh^* + Ce^* + {}^{16}O^{16}O$ Etapa 7

Los etapas de reacción que tienen lugar con Rh/CeO_2 son más eficaces que los que se basan exclusivamente en los pasos 1, 1 bis y 2 (observadas para Rh/γ-Al_2O_3), ya que los sitios activos de quimisorción de N_2O y de descomposición no sólo se encuentran en el rodio, sino también en la ceria.

3.3. Conclusiones

- El catalizador Rh/γ-Al_2O_3 es menos activo para la descomposición de N_2O que el catalizador Rh/CeO_2. La diferencia de actividad es consecuencia de la participación de la ceria en el mecanismo de descomposición de N_2O.

- El soporte de ceria interacciona fuertemente con el rodio y estabiliza especies oxidadas del metal noble, mientras que en Rh/γ-Al_2O_3 el metal se reduce a Rh^0 en condiciones de reacción.

- En Rh/CeO_2, los sitios activos para la quimisorción y descomposición de N_2O no están localizados exclusivamente en el rodio, sino también en el soporte de ceria.

4. Catalizador Rh/Ce_2O(Pr)/γ-Al_2O_3 para la descomposición de N_2O en presencia de O_2, H_2O y NO

4.1. Experimental

Las muestras usadas en este apartado han sido CeO_2(Pr)/γ-Al_2O_3, Rh/CeO_2(Pr) y Rh/CeO_2(Pr)/γ-Al_2O_3 y han sido caracterizadas mediante SEM, TEM, DRX, espectroscopia Raman, adsorción de N_2 a -196 ºC, RTP-H_2 y XPS.

Los ensayos catalíticos se han realizado usando una mezcla gaseosa consistente en 1000 ppm N_2O/He a GHSV = 10000 h^{-1} con el catalizador en polvo (Rh/CeO_2(Pr)) y con el catalizador soportado en partículas de alúmina (Rh/CeO_2(Pr)/γ-Al_2O_3). Además se realizaron ensayos catalíticos con el catalizador soportado utilizando una velocidad espacial de 30000 h^{-1} con una mezcla gaseosa con uno o más de los siguientes componentes: 1000 ppm N_2O; 1000 ppm NO; 1, 2.2 o 5% O_2; 2.4 % H_2O; y He como gas portador.

Se realizaron mediciones mediante la técnica espectroscópica DRIFTS en condiciones de reacción con las siguientes composiciones: 1000 ppm N_2O/He, 1000 ppm N_2O/5%O_2/He, 1000 ppm N_2O/2.6%H_2O o 1000 ppm N_2O/1000 ppm NO/ 5%O_2.

4.2. Resultados y discusión

4.2.1. Caracterización

De los resultados de caracterización se puede concluir que el catalizador Rh/CeO_2(Pr)/γ-Al_2O_3 consiste en partículas de γ-Al_2O_3 cubiertas de fase activa Rh/CeO_2(Pr), con el rodio anclado preferentemente al CeO_2(Pr). La interacción entre CeO_2(Pr) y γ-Al_2O_3 afecta a la interacción del Rh con CeO_2(Pr). Las partículas de rodio en Rh/CeO_2(Pr)/γ-Al_2O_3 son ligeramente mayores que en el catalizador homólogo en polvo Rh/CeO_2(Pr). La formación de especies Rh-Ce-Pr fácilmente reducibles de alta actividad catalítica, está parcialmente impedida por la γ-Al_2O_3.

4.2.2. Ensayos catalíticos

Se ha comparado la descomposición de N_2O de los catalizadores /CeO_2(Pr) y Rh/CeO_2(Pr)/γ-Al_2O_3 usando una corriente gaseosa de 1000 ppm N_2O/He. Los perfiles de conversión de N_2O y las velocidades de descomposición obtenidas se pueden observar en la Figura 10.

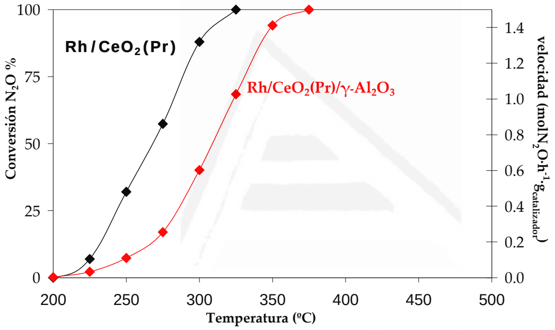

Figura 10. Velocidad de descomposición y conversión de N_2O en función de la temperatura en los ensayos realizados con Rh/CeO_2(Pr) y Rh/CeO_2(Pr)/γ-Al_2O_3 en N_2O/He 1000 ppm.

La temperatura a la que se inicia la descomposición de N_2O es 225 ºC para ambos catalizadores. A temperaturas más elevadas, la actividad del catalizador soportado Rh/CeO_2(Pr)/γ-Al_2O_3 es menor que la del homólogo en polvo Rh/CeO_2(Pr), con un retraso de 25-30 ºC en la posición de la curva de descomposición. Esta diferencia puede atribuirse a la interacción entre CeO_2(Pr) y γ-Al_2O_3, que a su vez afecta a la interacción del rodio con CeO_2(Pr) y disminuye la actividad catalítica.

La descomposición de N_2O para el catalizador soportado Rh/CeO_2(Pr)/γ-Al_2O_3 se ha estudiado también en presencia de O_2, H_2O y/o NO_x. La Figura 11 muestra los resultados de actividad catalítica obtenidos para las diferentes mezclas estudiadas.

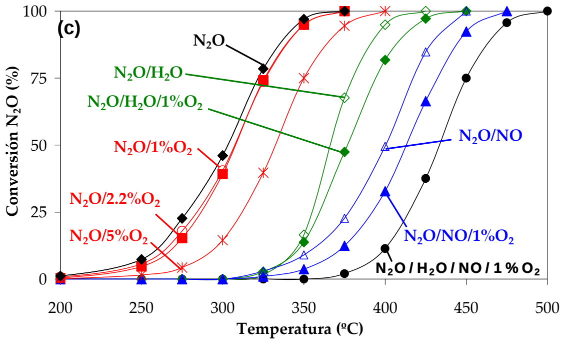

Figura 11. Efecto de la composición del gas en la descomposición de N_2O a diferentes temperaturas.

El O_2 sólo presenta un ligero efecto inhibidor en concentraciones del 5%, siendo nulo para concentraciones inferiores. El H_2O inhibe considerablemente la reacción, desplazando la curva de descomposición 50 ºC respecto a N_2O/He y el NO resulta ser el inhibidor más potente ya que retrasa el inicio de la conversión de N_2O unos 100 ºC.

Las diferencias entre las curvas N_2O/H_2O y $N_2O/1\%$ O_2/H_2O son mínimas, es decir, la introducción conjunta de O_2 y H_2O no genera efecto sinérgico y la inhibición es principalmente debida al H_2O. Contrariamente, al utilizar la mezcla que contiene $N_2O/1\%$ O_2/NO, se observa un desplazamiento en la curva de 25 ºC hacia temperaturas superiores con respecto a N_2O/NO, es decir, la presencia de O_2 aumenta el efecto inhibidor del NO. Este efecto es consecuencia de la formación de NO_2 por oxidación de NO, que también está catalizada por el mismo catalizador. Esta reacción secundaria puede competir con la descomposición de N_2O o bien el propio producto (NO_2) puede desactivar el catalizador al quimisorberse en los sitios activos.

Al introducir todos los gases de reacción presentes en una planta de ácido nítrico de forma conjunta (mezcla $N_2O/NO/1\%O_2/H_2O$), se obtienen resultados muy prometedores ya que la descomposición de N_2O se inicia a 350 ºC y se alcanza el 100 % de conversión de N_2O a 500 ºC.

4.2.2. *Experimentos DRIFTS in situ*

Para entender el efecto inhibidor del O_2, NO_x y H_2O en la descomposición catalítica de N_2O en Rh/CeO_2(Pr)/γ-Al_2O_3, se han realizado experimentos DRIFTS *in situ* con diferentes mezclas de gases. Los espectros infrarrojos obtenidos en estos experimentos se recogen en la Figura 12.

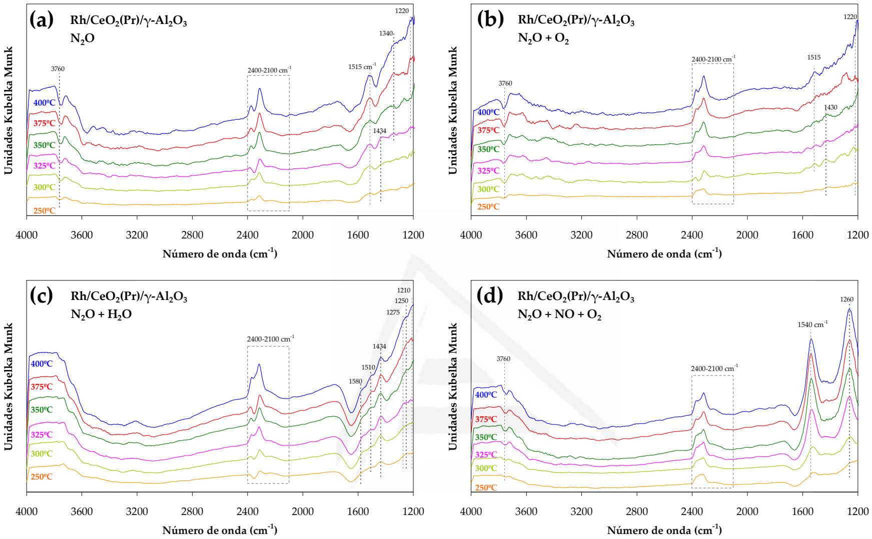

Figura 12. Espectros DRIFT *in situ*.

La interacción de N_2O y N_2O + O_2 con el catalizador Rh/CeO_2(Pr)/γ-Al_2O_3, genera bandas por debajo de los 1700 cm^{-1} (además de las bandas de N_2O). Esto confirma que el CeO_2 es capaz de oxidar el N_2O para producir diferentes especies oxidadas de nitrógeno en la superficie del catalizador.

Efecto del H_2O: La presencia de H_2O en la mezcla de gases disminuye la formación de especies oxidadas de nitrógeno en la superficie. Esto indica que el H_2O inhibe parcialmente los sitios donde las especies oxidadas de nitrógeno se forman. La evolución de la señal correspondiente a los grupos hidroxilo en la región de 3600-3800 cm^{-1} apoya esta hipótesis. En ausencia de H_2O, los grupos hidroxilo se consumen durante la descomposición de N_2O y aparece una banda negativa en 3760 cm^{-1}. En cambio, en presencia de H_2O, los grupos hidroxilo parecen formarse por quimisorción de H_2O en los sitios vacantes disponibles y, como resultado, no se observa la banda negativa a

3760 cm^{-1}. La quimisorción de H_2O en la superficie del catalizador explica la disminución de la capacidad de descomposición de N_2O.

Efecto de NOx: Se observan bandas en el rango 2400-2100 cm^{-1}, debido a la quimisorción de N_2O, una banda negativa a 3760 cm^{-1}, debido al consumo de los grupos hidroxilo y bandas por debajo de 1700 cm^{-1}, que se atribuyen a especies de nitrógeno oxidados. Como era de esperar, la formación de especies de nitrógeno se ve favorecida en presencia de $NO + O_2$ en la corriente de gas, y el efecto inhibidor de NOx se atribuye a su absorción química en sitios de la superficie del catalizador.

En el apartado *"3. Estudio del mecanismo de descomposición de N_2O con catalizadores de Rh/CeO_2 y $Rh/\gamma\text{-}Al_2O_3$"* se llego a la conclusión de que el mecanismo de descomposición de N_2O para el catalizador Rh/CeO_2 seguía las siguientes etapas:

$Rh\text{-}O + N_2O \rightarrow Rh^* + N_2 + O_2$ Etapa 1
$Rh^* + N_2O \rightarrow Rh^*\text{-}O + N_2$ Etapa 2
$2Rh^*\text{-}O \rightarrow 2Rh^* + O_2$ Etapa 3
$Rh^* + Ce^*\text{-}O \rightarrow Rh^*\text{-}O + Ce^*$ Etapa 4
$Ce^* + N_2O \rightarrow Ce^*\text{-}O + N_2$ Etapa 5
$2Ce^*\text{-}O \rightarrow 2Ce^* + O_2$ Etapa 6
$Rh^*\text{-}O + Ce^*\text{-}O \rightarrow Rh^* + Ce^* + O_2$ Etapa 7

donde $Rh^*\text{-}O$ y Rh^* son sitios oxidados y reducidos de catalizador de Rh, respectivamente, y $Ce^*\text{-}O$ y Ce^* son sitios oxidados y reducidos de la CeO_2.

Considerando este mecanismo, el efecto inhibidor del O_2 se puede atribuir a su absorción química reversible en los sitios de catalizador (reacciones inversas de las etapas 3, 6 y 7).

Respecto al efecto de H_2O, una vez que los sitios de rodio se reducen debido al N_2O (etapa 1), el sitio puede ser reoxidado ya sea por otra molécula de N_2O (etapa 2) o por el oxígeno del CeO_2 (etapa 4). Además, la banda negativa que aparece en 3760 cm^{-1} durante la descomposición de N_2O

sugiere que los grupos hidroxilo también están implicados en el mecanismo, posiblemente mediante la reacción:

$$2\ \text{Ce-OH} + N_2O \rightarrow 2\ \text{Ce-}^{*} + N_2 + H_2O + O_2 \qquad \text{Etapa 8}$$

El consumo de los grupos hidroxilo dará lugar a la formación de sitios de cerio reducido. Los experimentos realizados en presencia de H_2O permiten concluir que el H_2O y el N_2O compiten por los sitios vacantes creados en la superficie del CeO_2 (Ce*), en otras palabras, la etapa 5 compite con la etapa 9:

$$\text{Ce-}^{*} + \text{Ce-O} + H_2O \rightarrow 2\text{Ce-OH} \qquad \text{Etapa 9}$$

4.3. Conclusiones

- El catalizador Rh/CeO_2(Pr)/γ-Al_2O_3 está formado por partículas de γ-Al_2O_3 cubiertas por la fase activa Rh/CeO_2(Pr), en la que el Rh está anclado preferentemente en el CeO_2(Pr) y no en la γ-Al_2O_3.

- La actividad del catalizador soportado Rh/CeO_2(Pr)/γ-Al_2O_3 es ligeramente inferior a la de la fase activa en polvo (Rh/CeO_2(Pr)). Esta diferencia se atribuye a la interacción entre CeO_2(Pr) y γ-Al_2O_3, que a su vez afecta a la interacción de Rh con CeO_2(Pr). Las partículas de Rh en Rh/CeO_2(Pr)/γ-Al_2O_3 son ligeramente más grandes que en Rh/CeO_2(Pr) y la formación de especies fácilmente reducibles Rh-Ce-Pr está parcialmente obstaculizada por la alúmina.

- La actividad del catalizador Rh/CeO_2(Pr)/γ-Al_2O_3 es parcialmente inhibida en presencia de O_2, H_2O y NOx. El NOx es el inhibidor más fuerte y el O_2 es el más débil. El efecto inhibidor del O_2 se atribuye a su absorción química reversible en sitios de catalizador, mientras que el efecto de H_2O y NOx se debe, principalmente, a una quimisorción irreversible.

5. Eliminación de N_2O en una planta de producción de ácido nítrico

5.1. Experimental

Para desarrollar este estudio se ha utilizado el catalizador $Rh/CeO_2(Pr)/\gamma\text{-}Al_2O_3$. Este catalizador ha sido analizado antes y después de ser usado en la reacción de descomposición de N_2O utilizando diferentes técnicas de caracterización. La superficie específica BET ha sido determinada mediante adsorción de N_2 a -196 ºC y las características estructurales se han estudiado por difracción de rayos X y espectroscopía Raman. La naturaleza de las especies se ha analizado mediante XPS y se ha determinado la reducibilidad del soporte y del catalizador mediante experimentos de reducción a temperatura programada con H_2 (RTP-H_2). Finalmente, el tamaño de las partículas de metal noble se determinó por microscopía TEM.

Los ensayos catalíticos se llevaron a cabo en la planta de producción de ácido nítrico que tiene la Compañía de Producción de Fertilizantes Nitrogenados de Pulawy (Polonia). Estos ensayos se realizaron usando un reactor tubular de lecho fijo con 2 g de catalizador ubicado en un reactor para el control de la temperatura. La alimentación de gases empleada fue extraída directamente de la corriente de gases de la planta producción de ácido nítrico tras la turbina de expansión, empleándose caudales entre 100 y 800 ml/min.

Se realizaron dos tipos de ensayos:

- Ensayos de descomposición de N_2O a temperatura programada, consistentes en estabilizar la temperatura del catalizador a 200 ºC en una corriente de N_2 y, a continuación, introducir la corriente de gas extraída de la planta y aumentar la temperatura a razón de 2 ºC/min hasta 450 ºC. En estos ensayos se emplearon diferentes velocidades espaciales (7500, 15000 y 30000 h^{-1}).

- Ensayos de descomposición de N_2O en régimen isotermo a 350 ºC, utilizando diferentes velocidades espaciales (3800, 7500 y 15000 h^{-1}).

Para interpretar correctamente los resultados de caracterización del catalizador usado hay que mencionar que en todos los ensayos catalíticos se ha utilizado la misma muestra de catalizador. Tras la realización de todos los ensayos catalíticos, esta muestra de catalizador ha estado unas 40 horas no consecutivas en presencia de la corriente de gas de la planta de producción de ácido nítrico. Durante este tiempo, el catalizador ha sido sometido a nueve ciclos de calentamiento-enfriamiento y periodos de distinta duración en condiciones isotermas a 350 ºC.

5.2. Resultados y discusión

5.2.1. Ensayos catalíticos

En la Figura 13 se recogen los perfiles de conversión de N_2O en función de la temperatura correspondientes a los diferentes experimentos a temperatura programada realizados en la planta de producción de ácido nítrico a 7500, 15000 y 30000 h^{-1}.

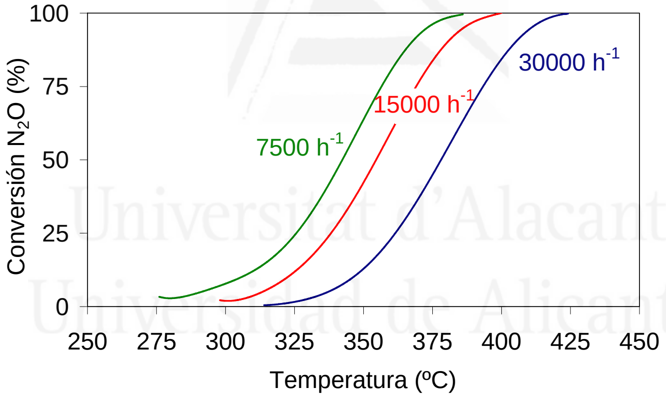

Figura 13. Ensayos de descomposición de N_2O a temperatura programada en una corriente real de una planta de producción de ácido nítrico (composición del gas: 1000 ppm N_2O + 750 ppm NO_x + 1%H_2O + 2%O_2) utilizando el catalizador Rh/CeO_2(Pr)/γ-Al_2O_3.

La conversión de N_2O comienza entre 275 y 325 ºC, dependiendo de la velocidad espacial empleada, alcanzándose la descomposición completa entre 380 y 425 ºC. Como es esperable, la conversión de N_2O aumenta al disminuir la velocidad espacial. Con el catalizador en polvo Rh/CeO_2(Pr) se alcanzó a 350 ºC el 100% de conversión de N_2O en el ensayo de laboratorio realizado con una corriente de 100ppm N_2O + 5%O_2 y una velocidad espacial de 10000 h^{-1}. Considerando el efecto de los inhibidores (H_2O y NOx) presentes en los gases procedentes de la planta de ácido nítrico, se puede concluir que se ha conseguido escalar con éxito el catalizador en polvo a un catalizador soportado que permite trabajar con corrientes de gas reales.

Por otra parte, se realizó un estudio sobre la estabilidad del catalizador. En la Figura 14 se presentan los resultados de experimentos isotermos realizados a 350 ºC. Como se observa en la Figura 14, en todas las condiciones de trabajo empleadas el catalizador mantiene su actividad constante durante un intervalo de tiempo de 30 minutos aproximadamente, lo que demuestra que el catalizador, además de tener una buena actividad catalítica, es estable en las condiciones requeridas para trabajar en una planta de ácido nítrico. Esta estabilidad es consistente con las similares propiedades físico-químicas mostradas por el catalizador fresco y usado.

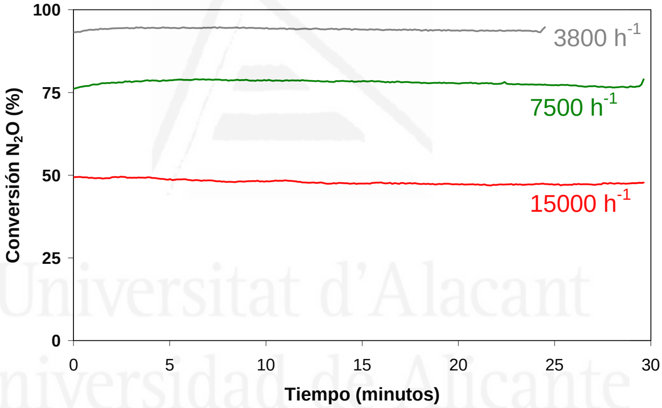

Figura 14. Ensayos de descomposición de N_2O en condiciones isotermas a 350 ºC en una corriente real de una planta de producción de ácido nítrico (composición del gas: 1000 ppm N_2O + 750 ppm NOx + 1%H_2O + 2%O_2) utilizando el catalizador Rh/CeO_2(Pr)/γ-Al_2O_3.

5.2.2. Caracterización

De la caracterización del catalizador antes y después de ser utilizado en la planta de producción de ácido nítrico se deduce que el catalizador no presenta modificaciones en sus propiedades físico-químicas: (i) mediante difracción de rayos X y espectroscopía Raman no se mostró ningún cambio en la estructura fluorita del óxido mixto de Ce-Pr después de los ensayos catalíticos, (ii) el tamaño de los cristales de las partículas de óxido mixto de

Ce-Pr y el área superficial BET de los catalizadores no cambia durante los ensayos catalíticos, lo que indica que no se ha producido la sinterización del óxido de cerio, (iii) la técnica de RTP-H_2 indica que la reducibilidad del catalizador es similar antes y después de las pruebas catalíticas, mostrando buena estabilidad química, y (iv) estabilidad de los tamaños de partículas de rodio y del estado de oxidación, deducido a partir de TEM y XPS, respectivamente.

5.3. Conclusiones

- El catalizador soportado es activo para la descomposición de N_2O en corrientes de gases complejas tales como las de las plantas de producción de ácido nítrico. A pesar del efecto inhibidor del O_2, H_2O y NOx se logra la descomposición completa del N_2O entre 380 y 425 ºC, dependiendo de la velocidad espacial empleada.

- El catalizador soportado es estable, y no muestra disminución de la actividad catalítica con el tiempo de operación ni modificación de las propiedades físico-químicas durante los ensayos catalíticos.

Bibliografia

[1] C. Baird. Química Ambiental. Reverté (2001).
[2] T.G. Spiro, W.M. Stigliani. Química Medioambiental. Pearson Prentice Hall (2005).
[3] http://www.ghgonline.org/index.htm
[4] http://www.bbc.co.uk/spanish/especiales/clima/index.shtml
[5] F. Kapteijn, J. Rodriguez Mirasol, J.A. Moulijn. Appl. Catal. B, 9 (1996) 25.
[6]H.S. Gandhi, G.W. Graham, R. McCabe. J. Catal. 216 (2003) 433.
[7]S.J. Lee, I.S. Ryu, B.M. Kim, S.H. Moon. Int. J. Greenhouse Gas Control 5 (2011) 167.
[8]A. Bueno-López, I. Such-Basáñez, C. Salinas-Martínez de Lecea. J. Catal. 244 (2006) 102.
[9] J. Kăspar, P. Fornasiero, M. Graziani. Catal. Today 50 (1999) 285.
[10] S. Bernal, G. Blanco, J.J. Calvino, J.M. Gatica, J.A. Perez-Omil, J.M. Pintado. Topics Catal. 28 (2004) 31.

[11] European Climate Change Programme: http://ec.europa.eu/environment/climat/eccp_review.htm
[12] J. Pérez-Ramírez. Appl. Catal. B 70 (2007) 31.
[13] A. Bueno-López, I. Such-Basáñez, C. Salinas-Martínez de Lecea. J. Catal. 244 (2006) 102.
[14] F. Kapteijn, J. Rodriguez-Mirasol, J.A. Moulijn. Applied Catalysis B 9 (1996) 25.
[15] K.I. Hadjiivanov, Catal. Rev. Sci. Eng. 42 (2000) 71.
[16] N. Oktar, J. Mitome, E.M. Holmgreen, U.S. Ozkan. J. Mol. Catal. A. 259 (2006) 171.
[17] Y. Wang, Z. Lei, B. Chen, Q. Guo, N. Liu, Appl. Surf. Sci. 256 (2010) 4042.
[18] S. Haq, A. Hodgson, Surf. Sci. 463 (2000) 1.
[19] P. Djinović, J. Batista, A. Pintar, Catal. Today 147 (2009) 191.
[20] P.V. Menacherry, G.L. Haller, Catal. Letters, 44 (1997) 135.

Curriculum Vitae

CURRICULUM VITAE

Sonia Parres Esclapez was born on the 25th of November 1982 in Elche, Spain. She obtained her pre-university education from the Institute Tirant lo Blanc (Elche) in 2000 and earned a university degree in chemistry from the University of Alicante in 2006. In that year, she started her Ph.D. studies in environmental catalysis in the Carbon Materials and Environment Research Group at the University of Alicante. In 2008 she obtained a pre-doctoral fellowship funded by the University of Alicante-CAM-Union Fenosa. In July 2009, she wrote her DEA (Advance Studies Certificate) with the title "Rhodium catalysts supported on CeO_2 to N_2O decomposition" under the supervision of Prof. Agustín Bueno López and Prof. María José Illán Gómez. This work was awarded the San Alberto Magno XVII Award for the best master's thesis by the Royal Spanish Society of Chemistry. This Ph.D. thesis describes the most important findings of the research she performed in N_2O decomposition from 2006 to 2011.

LIST OF PUBLICATIONS

- V. Rico-Pérez, S. Parres-Esclapez, M. J. Illán-Gómez, C. Salinas-Martínez de Lecea, A. Bueno-López. "Preparation, characterisation and N_2O decomposition activity of honeycomb monolith-supported $Rh/Ce_{0.9}Pr_{0.1}O_2$ catalysts". Applied Catalysis B: Environmental 107 (2011) 18.

- Q. He, S. Mukerjee, S. Parres-Esclapez, A. Bueno-López." Effect of praseodymium oxide and cerium-praseodymium mixed oxide in the Pt electrocatalyst performance for the oxygen reduction reaction in PAFCs" Journal of Applied Electrochemistry 41 (2011) 891.

- S. Parres-Esclapez, I. Such-Basañez, M.J. Illán-Gómez, C. Salinas-Martínez de Lecea, A. Bueno-López. "Study by isotopic gases and in situ spectroscopies (DRIFTS, XPS and Raman) of the N_2O decomposition mechanism on Rh/CeO_2 and $Rh/\gamma\text{-}Al_2O_3$ catalysts" Journal of Catalysis 276 (2010) 390.

- C. Bueno-Ferrer, S. Parres-Esclapez, D. Lozano-Castelló, A. Bueno-López. "Relationship between surface area and crystal size of pure and doped cerium oxides" Journal of Rare Earths 28 (2010) 647.

- Q. He, S. Mukerjee, R. Zeis, S. Parres-Esclapez, M.J. Illán-Gómez, A. Bueno-López. "Enhanced Pt stability in MO_2 (M = Ce, Zr or $Ce_{0.9}Zr_{0.1}$)-promoted Pt/C electrocatalysts for oxygen reduction reaction in PAFCs" Applied Catalysis A: General 381 (2010) 54.

- S. Parres-Esclapez, M.J. Illán-Gómez, C. Salinas-Martínez de Lecea, A. Bueno-López. "On the importance of the catalyst redox properties in the N_2O decomposition over alumina and ceria supported Rh, Pd and Pt" Applied Catalysis B: Environmental 96 (2010) 370.

- I. Miguel-García, S. Parres-Esclapez, D. Lozano-Castelló, A. Bueno-López. "H_2 assisted decomposition of cerium nitrate to ceria with enhanced catalytic properties" Catalysis Communications 11 (2010) 848.

- S. Parres-Esclapez, F.E. López-Suárez, A. Bueno-López, M.J. Illán-Gómez, B. Ura, J. Trawczynski. "Rh-Sr/Al_2O_3 catalyst for N_2O decomposition in the presence of O_2" Topics in Catalysis 52 (2009) 1832.

- F.E. López-Suárez, S. Parres-Esclapez, A. Bueno-López, M.J. Illán-Gómez, B. Ura, J. Trawczynski. "Role of surface and lattice copper species in copper-containing (Mg/Sr)TiO_3 perovskite catalysts for soot combustion" Applied Catalysis B: Environmental 93 (2009) 82.

- Q. He, S. Mukerjee, B. Shyam, D. Ramaker, S. Parres-Esclapez, M.J. Illán-Gómez, A. Bueno-López. "Promoting effect of CeO_2 in the electrocatalytic activity of rhodium for ethanol electro-oxidation" Journal of Power Source 193 (2009) 408.

- G. Garrigós-Pastor, S. Parres-Esclapez, A. Bueno-López, M.J. Illán-Gómez, C. Salinas-Martínez de Lecea. "Power-bench demonstration of the Pt-catalysed C_3H_6-SCR of NOx in a diesel exhaust" Applied Catalysis A: General 354 (2009) 63.

- S. Parres-Esclapez, F.E. López-Suárez, A. Bueno-López, M.J. Illán-Gómez, B. Ura, J. Trawczynski. "Enhanced N_2O Decomposition over Sr-promoted Rh/Al_2O_3 Catalysts" Polish Journal of Environmental Studies 18 (2009) 176.

- J. Alcañiz-Monge, G. Trautwein, S. Parres-Esclapez, J.A. Maciá-Agulló. "Influence of microporosity of activated carbons as a support of polyoxometalates" Microporous and Mesoporous Materials 115 (2008) 440.

- G. Garrigós-Pastor, I. Such-Basáñez, S. Parres-Esclapez, A. Bueno-López, M.J. Illán-Gómez, C. Salinas-Martínez de Lecea. "Eliminación catalítica de contaminantes en motores Diésel" Anales de la Real Sociedad Española de Química 104 (2008) 31.

PATENTS

- A. Bueno-López, M.J. Illán-Gómez, S. Parres-Esclapez, C. Salinas-Martínez de Lecea. "Sistemas catalíticos de rodio y óxido de cerio modificado para la descomposición de N_2O en N_2 y O_2" P200901897.

LIST OF CONTRIBUTIONS TO INTERNATIONAL CONFERENCES

- S. Parres-Esclapez, I. Such-Basañez, M.J. Illán-Gómez, C. Salinas-Martínez de Lecea, A. Bueno-López. "The N_2O decomposition mechanism on Rh catalysts studied by isotopic gases and in situ spectroscopies (DRIFTS, XPS and RAMAN)" 10th European Congress on Catalysis (EuropaCat X), Glasgow, United Kingdom, September 2011 (poster).

- I. Miguel-García, S. Parres-Esclapez, D. Lozano-Castelló, A. Bueno-López. "H_2 assisted decomposition of cerium nitrate to ceria with enhanced catalytic properties" 10th European Congress on Catalysis (EuropaCat X), Glasgow, United Kingdom, September 2011 (poster).

- V. Rico-Pérez, S. Parres-Esclapez, M. J. Illán-Gómez, C. Salinas-Martínez de Lecea, A. Bueno-López. "Preparation, characterization and catalytic performance for N_2O decomposition of $Rh/Ce_{0.9}Pr_{0.1}O_2$/monolith" 10th European Congress on Catalysis (EuropaCat X), Glasgow, United Kingdom, September 2011 (poster).

- S. Parres-Esclapez, A. Bueno-López, M. J. Illán-Gómez, C. Salinas-Martínez de Lecea. "Dual-bed catalytic systems for NOx-N_2O removal from diesel engine exhaust" APAC 2010, 2nd International Symposium on Air Pollution Abatement Catalysis, Krakow, Poland, September 2010 (poster).

- S. Parres-Esclapez, A. Bueno-López, M. J. Illán-Gómez, C. Salinas-Martínez de Lecea. "$Rh/CeO_2(Pr)/Al_2O_3$ catalyst for mild temperature N_2O decomposition in the presence of O_2, H_2O and NO. 9th European Congress on Catalysis (EuropaCat IX), Salamanca, Spain, September 2010 (poster).

- V. Rico-Pérez, S. Parres-Esclapez, M. J. Illán-Gómez, C. Salinas-Martínez de Lecea, A. Bueno-López. "Preparation, characterization and catalytic performance for N_2O decomposition of $Rh/Ce_{0,9}Pr_{0,1}O_2$/monolith" APAC 2010, 2nd International Symposium on Air Pollution Abatement Catalysis, Krakow, Poland, September 2010 (poster).

- S. Parres-Esclapez, F.E. López-Suárez, A. Bueno-López, M.J. Illán-Gómez, B. Ura, J. Trawczynski. "N_2O decomposition over Sr-promoted Rh/Al_2O_3 catalysts" 8th International Congress on Catalysis and Automotive Pollution Control (CAPOC), Brussels, Belgium, April 2009 (poster).

- S. Parres-Esclapez, F.E. López-Suárez, A. Bueno-López, M.J. Illán-Gómez B. Ura, J. Trawczynski. “Enhanced N_2O decomposition over Sr-promoted Rh/Al_2O_3 catalysts” Catalysis and Adsorption in Fuels Processing and Environmental Protection 2008 (CAFUEL), Szklarska Porêba, Poland, September 2008 (poster).

- S. Parres-Esclapez, F.E. López-Suárez, A. Bueno-López, M.J. Illán-Gómez, B. Ura, J. Trawczynski. “Effect of Sr and Mg in the activity of Rh/Al_2O_3 catalysts for N_2O decomposition” 2nd International Annual Meeting, Catalysis for Environment: Depollution, Renewable Energy and Clean Fuels, Zakopane, Poland, September 2008 (oral).

- S. Parres-Esclapez, A. Bueno-López, M. J. Illán-Gómez, C. Salinas-Martínez de Lecea. “N_2O decomposition mechanism on Rh catalyst studied by isotopic gases” 5th International Conference on Environmental Catalysis (ICEC), Belfast, United Kingdom, September 2008 (poster).

- J. Mora, B. Mancheño, N. Grané, L. Gras, V. Climent, M.J. Illán, F. Alonso, A. Beltrán, S. Parres, J. Mira, L. Pedro, A. López. “The assesment in the spanish university and its suitability to the EHEA. Conclusions obtained in a teaching-learning network” International Technology, Education and Development Conference, Valencia, Spain, March 2008 (poster).

- S. Parres-Esclapez, A. Bueno-López, M. J. Illán-Gómez, C. Salinas-Martínez de Lecea. “N_2O decomposition and reduction by CO on Ce/Pr mixed oxide-supported NM (NM = Pd, Rh or Pt) in the presence of O_2” 8th European Congress on Catalysis (EuropaCat VIII), Turku, Finland, August 2007 (poster).

LIST OF CONTRIBUTIONS TO NATIONAL CONFERENCES

- V. Rico-Pérez, S. Parres-Esclapez, M. J. Illán-Gómez, C. Salinas-Martínez de Lecea, A. Bueno-López. “Catalizadores $Rh/Ce_{0,9}Pr_{0,1}O_2$ soportados en monolitos de cordierita. Preparación, caracterización y ensayos catalíticos de descomposición de N_2O", SECAT 2011, Zaragoza, Spain, June 2011 (oral).

- I. Miguel-García, S. Parres-Esclapez, D. Lozano-Castelló, A. Bueno-López. "Descomposición de nitrato de cerio en atmósfera de hidrógeno para la obtención ceria con propiedades catalíticas mejoradas" SECAT 2011, Zaragoza, Spain, June 2011 (oral).

- S. Parres-Esclapez, I. Such-Basañez, M.J. Illán-Gómez, C. Salinas-Martínez de Lecea, A. Bueno-López. "Estudio mediante marcaje isotópico y espectroscopias in situ (DRIFT, XPS y Raman) del mecanismo de descomposición de N_2O en catalizadores de Rh" SECAT 2011, Zaragoza, Spain, June 2011 (poster).

- V. Rico-Pérez, S. Parres-Esclapez, M. J. Illán-Gómez, C. Salinas-Martínez de Lecea, A. Bueno-López. "Catalizadores $Rh/Ce_{0,9}Pr_{0,1}O_2$ soportados en monolitos de cordierita" XIV Reunión Científica Plenaria de Química Inorgánica y VIII Reunión Científica Plenaria de Química de Estado Sólido, Cartagena, Spain, September 2010 (oral).

- M. Martín-Martínez, M.A. Alvarez-Montero, L.M. Gomez-Sainero, S. Parres-Esclapez, A. Linares-Solano, J.J. Rodriguez. "Hidrodecloración de diclorometano en fase gas con catalizadores pt/ca. Efecto de las condiciones de preparación" X Reunión del Grupo Español del Carbón (GEC), Girona, Spain, May 2010 (poster).

- S. Parres-Esclapez, A. Bueno-López, M. J. Illán-Gómez, C. Salinas-Martínez de Lecea. "$Rh/CeO_2(Pr)/Al_2O_3$ para descomposición de N_2O en presencia de NO, O_2 y H_2O" SECAT 2009, Ciudad Real, Spain, June 2009 (oral).

- J. Mora, B. Mancheño, N. Grané, L. Gras, V. Climent, M.J. Illán, F. Alonso, A. Beltrán, S. Parres, J. Mira, L. Pedro, A. López. "La evaluación en la Universidad española y su adecuación al EEES. Conclusiones obtenidas en una red docente-discente" VI Jornadas de redes de investigación en docencia universitaria, Alicante, Spain, June 2008 (oral).

- J. Mora, B. Mancheño, N. Grané, L. Gras, V. Climent, M.J. Illán, F. Alonso, A. Beltrán, S. Parres, J. Mira, L. Pedro, A. López. “La evaluación en la universidad española actual y su adecuación al EEES. Conclusiones obtenidas en una red docente–discente” II Jornadas Nacionales de Metodologías ECTS, Badajoz, Spain, September 2007 (poster).

- S. Parres-Esclapez, A. Bueno-López, M. J. Illán-Gómez, C. Salinas-Martínez de Lecea. “Efecto del soporte en la descomposición de N_2O con catalizadores Rh, Pd, Pt/CeO_2(La, Pr)” SECAT 2007, Bilbao, Spain, June 2007 (poster).

- J. Mora, B. Mancheño, N. Grané, L. Gras, V. Climent, M.J. Illán, F. Alonso, A. Beltrán, S. Parres, J. Mira, L. Pedro, A. López. “El proceso de evaluación dentro de los planes piloto en Química de diferentes universidades españolas. Conclusiones obtenidas en una red docente-discente” II REUNIÓN INDOQUIM, Vigo, Spain, June 2007 (oral).

This thesis presents the results of the study of Rh catalysts supported on CeO_2 for the reaction of N_2O decomposition. The emission of this gas to the atmosphere cause environmental problems that are described along with the main anthropogenic sources and the current European legislation for this greenhouse gas control. In this work a series of catalysts Rh, Pd and Pt supported on γ-Al_2O_3, CeO_2 and CeO_2 doped with La or Pr, have been prepared, characterized and tested at a laboratory scale. The results show that the activity of the three noble metals studied follows the sequence Rh> Pd> Pt and the support plays a considerable effect on the catalysts activity. N_2O decomposition mechanisms have been studied by using spectroscopic techniques and isotopic labeling tests for Rh/γ-Al_2O_3 and Rh/CeO_2 catalysts. In this study the results of experiments conducting at laboratory scale and at pilot plant (stream of gases from a nitric acid plant) obtained with the most promising catalyst (Rh/CeO_2(Pr)) has been included. Finally, studying the effect of inhibitors such as H_2O, O_2 and NOx was also analyzed.

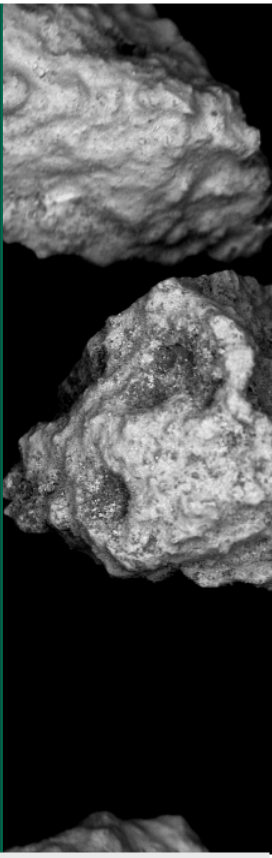

Sonia Parres Esclapez

Carbon Materials and Environment Research Group
Inorganic Chemistry Department
University of Alicante, Aptdo. 99 San Vicente del Raspeig, E-03080 Alicante, Spain

E-mail: sonia.parres@ua.es

MCMA Carbon Materials and Environment Research Group